Physics of erupting solar flux ropes: Coronal mass ejections (CMEs)—Recent advances in theory and observation

Cite as: Phys. Plasmas **24**, 090501 (2017); https://doi.org/10.1063/1.4993929
Submitted: 19 November 2013 . Accepted: 06 March 2017 . Published Online: 22 August 2017

James Chen

Physics of erupting solar flux ropes: Coronal mass ejections (CMEs)—Recent advances in theory and observation

James Chen
Plasma Physics Division, Naval Research Laboratory, Washington, DC 20375, USA

(Received 19 November 2013; accepted 6 March 2017; published online 22 August 2017)

Solar eruptions, observed as flares and coronal mass ejections (CMEs), are the most energetic visible plasma phenomena in the solar system. CMEs are the central component of solar eruptions and are detected as coherent magnetized plasma structures expanding in the solar wind (SW). If they reach the Earth, their magnetic fields can drive strong disturbances in the ionosphere, causing deleterious effects on terrestrial technological systems. The scientific and practical importance of CMEs has led to numerous satellite missions observing the Sun and SW. This has culminated in the ability to continuously observe CMEs expanding from the Sun to 1 AU, where the magnetic fields and plasma parameters of the evolved structures ("ejecta") can be measured *in situ*. Until recently, the physical mechanisms responsible for eruptions were major unanswered questions in solar and by extension stellar physics. New observations of CME dynamics and associated eruptive phenomena are now providing more stringent constraints on models, and quantitative theory-data comparisons are helping to establish the correct mechanism of solar eruptions, particularly the driving force of CMEs and the evolution of their magnetic fields in three dimensions. Recent work has demonstrated that theoretical results can simultaneously replicate the observed CME position-time data, temporal profiles of associated solar flare soft X-ray emissions, and the magnetic field and plasma parameters of CME ejecta measured at 1 AU. Thus, a new theoretical framework with testable predictions is emerging to model eruptions and the coupling of CME ejecta to geomagnetic disturbances. The key physics in CME dynamics is the Lorentz hoop force acting on toroidal "flux ropes," scalable from tokamaks and similar laboratory plasma structures. The present paper reviews the latest advances in observational and theoretical understanding of CMEs with the emphasis on quantitative comparisons of theory and observation. *Published by AIP Publishing.*
[http://dx.doi.org/10.1063/1.4993929]

I. INTRODUCTION

The Sun is the most dominant object in the solar system. Its mass, $M_\odot = 1.99 \times 10^{33}$ g, constitutes approximately 99.8% of the total mass of the system. Most of this mass is in the form of plasma. To the casual observer, the Sun is constant and placid. To the keen observer, however, it is neither constant nor placid, sporadically exhibiting "eruptions" that are observed as *coronal mass ejections* (CMEs), *eruptive prominences* (EPs), or *solar flares* depending on the method of observation. CMEs and EPs appear as large plasma structures of the order of the solar radius, $1R_\odot = 6.96 \times 10^5$ km, accelerating and expanding away from the Sun. Their speeds can reach several hundred to a few thousand kilometers per second in tens of minutes. Solar flares, detectable in electromagnetic radiation ranging from radiowaves to γ-rays, appear as localized quasi-stationary brightening in the low corona. Figure 1 shows the morphology of a solar flare (solid arrow) observed in X-rays. Exceptionally powerful flares are visible in white light against the bright solar disk, but such events are rare. Most flares are much less energetic and are observed in limited wavelength bands such as X-rays, extreme ultraviolet (EUV), and hydrogen alpha (Hα, $\lambda = 6562.8$ Å) where the background is relatively dark (e.g., Fig. 1). These phenomena are the most energetic plasma processes observed in the solar system: each occurrence expels an estimated 10^{14}–10^{16} g of mass and 10^{30}–10^{33} ergs of energy as kinetic energy of bulk plasma motion (CMEs and EPs) and photon energy (flares). These processes occur over tens of minutes to several hours. Still, the mass and energy losses in eruptions are miniscule compared to the solar mass $M_\odot = 2 \times 10^{33}$ g, steady mass loss of $\sim 10^{12}$ g s^{-1} due to the *solar wind* (SW), and luminosity $\mathcal{L}_\odot = 3.8 \times 10^{33}$ erg s^{-1}. The energy source—presumed to be magnetic—and physical mechanisms of eruption have been long-standing questions in physics.

Historically, different manifestations of eruptions were discovered as new observations became available. The first solar eruption to be recorded as such was a rare white-light flare serendipitously discovered in 1859 by two astronomers during independent sunspot observations.[1,2] It appeared as intensely bright patches against the solar disk, lasting for about 5 min.[2] Both observers were surprised, describing the occurrence as "singular appearance" and "curious appearance." Some of the bright patches were reported to "move" $\sim$35 000 mile (5.6×10^4 km) during the event.[1] This translates to an apparent speed of $\sim$200 km s^{-1}, much faster than the speeds associated with discernible changes in sunspot features ($<$1 km s^{-1}). With the advent of spectroheliographs that could image the Sun at specific wavelengths,[3,4] flares were found to be common at lower brightness levels in

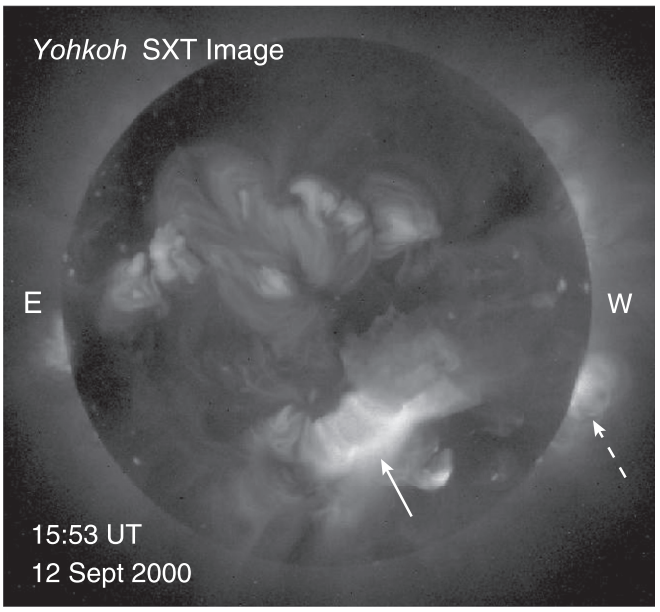

FIG. 1. *Yohkoh* soft x-ray telescope (SXT) image of a solar flare (solid arrow) at 15:53 UT on 12 September 2000, showing an "arcade" of bright loops (solid arrow) against the X-ray dark photosphere, some 3 h after the peak. The flare erupted in NOAA active region (AR) 9163. The hot X-ray loops are coronal structures rising well above the solar surface. An earlier flare occurred on the west limb (right in the image, NOAA AR 9154), providing a view of an arcade from the side (dashed arrow). By convention, the west (east) limb is on the right (left) based on the observer in the northern hemisphere of the Earth.

various wavelength regimes. Flares are often accompanied by radiowave emissions whose sources move away from flare sites at upwards of 1000 km s^{-1} (moving type IV bursts).[5–7]

Prominences, which radiate in Hα and would be visible to the naked eye but for the bright solar disk, had been observed during solar eclipses as reddish arched structures suspended above the solar limb. Figure 2 shows in near-natural color a few prominences (pinkish) and the corona (diffuse white) during a total solar eclipse.[8] The motion of a prominence would be difficult to see during the limited duration of an eclipse, but by early 1900s, it had been determined from Doppler data and spectroheliographic images that they sporadically erupted at several hundred kilometers per second.[9–11]

The first CME was observed relatively recently,[12] in 1971 by the space-borne coronagraph on the Orbiting Solar Observatory 7 (OSO-7): it appeared as a coronal density structure (a band of bright pixels) moving outward at an apparent speed in excess of 1000 km s^{-1}. A coronagraph, invented by Lyot in the 1930s,[13,14] is a telescope that uses an occulter to block the bright solar disk, in effect creating a perpetual artificial eclipse, so that the faint corona can be observed. Meanwhile, the existence of the SW, a steady outflow of plasma from the Sun, was confirmed by satellite observations.[15–17]

The 1859 flare was followed by a major *geomagnetic storm* at the Earth; such storms are characterized by large-amplitude fluctuations in the ground magnetic field and bright aurorae around the globe.[18] It was suspected to have been caused by the flare, but this was met with skepticism ("One swallow does not make a summer"[1]) although apparent links between sunspots and aurorae had been noted.[19,20] For

FIG. 2. Total solar eclipse on 11 August 1999 viewed in France. The corona (whitish and diffuse) and prominences (reddish) are visible in near-natural color. The corona is visible because of Thomson scattering of photospheric light by free electrons. The thin reddish layer along the disk gives a glimpse of the chromosphere radiating in Hα (6562.8 Å). The white spots in the prominences are saturated Hα pixels. Credit: Original full-disk image by Luc Viatour/www.Lucnix.be.

example, the "prolonged sunspot minimum" (1645–1715)[21,22]—the so-called Maunder Minimum[23]—was correlated with a marked dearth of aurorae,[19,20] but "it is not obvious that anyone in solar physics listened" to the message of Sun-Earth connection and solar influence on the Earth.[23]

The nature of the suspected solar-terrestrial connection remained mysterious until the age of satellite observation. With *in situ* measurements of the SW plasmas, it became clear that long durations (several hours) of strong southward ($z<0$) interplanetary magnetic field (IMF) emanating from the Sun, say, $B_z < -10$ nT (nanotesla), were correlated with geomagnetic storms.[24–26] Burlaga *et al.*[27] reported observation of a large magnetized plasma "loop," dubbed an interplanetary (IP) "magnetic cloud" (MC), detected at 1 AU and 2 AU by multiple spacecraft. At the Helios 2 spacecraft near 1 AU, it was inferred to be ∼0.5 AU in radial extent along the Sun-Earth line, and the measured magnetic field in the loop reached $B_{max} \sim 20$ nT, with the field vector **B** smoothly rotating from the southward to the northward orientation over 36 h. This observation led the way in clarifying the three-dimensional (3-D) spatial structure of such *geoeffective* (storm-causing) unipolar IMF periods, which are distinguishable from the rapidly fluctuating background IMF of ∼5 nT. These properties are characteristic of MCs at 1 AU.[28] If they impinge on the Earth, MCs can impose long durations (say, 10–20 h) of strong southward IMF on the magnetosphere, producing major geomagnetic storms.

Subsequent work established a statistical association between MCs at 1 AU and CMEs and EPs at the Sun.[29–31] The association was statistical because coronagraphs had limited fields of view (FOVs) and could not observe CMEs propagating toward the space-borne magnetometers and particle detectors placed at the L1 Lagrange point on the Sun-Earth line, approximately 10^{-2} AU from the Earth toward the Sun. With the launch of the Solar Terrestrial Relations

Observatory (STEREO) mission[32] in 2006, consisting of two identical spacecraft (A and B) placed in the ecliptic but off the Sun-Earth line, it became possible for the first time to directly observe CME ejecta from the Sun to 1 AU, where under favorable circumstances, the ejecta magnetic fields could be measured *in situ*. In some fortuitous cases, the CME-MC connection has been confirmed.[33]

Each STEREO spacecraft carries an identical suite of telescopes and *in situ* detectors—Sun Earth Connection Coronal and Heliospheric Investigation (SECCHI)[34]—consisting of inner Sun-centered coronagraphs COR1 and COR2 ($1.3–15\,R_\odot$), outer side-viewing heliospheric imagers HI1 and HI2 ($12–215\,R_\odot$), Extreme Ultraviolet Imager (EUVI), a magnetometer (IMPACT), and a plasma detector (PLASTIC). Coronagraph data yield line-of-sight (LOS) integrated density distributions projected onto the two dimensional (2-D) plane of the sky and do not show the 3-D *magnetic* geometry of CMEs or the magnetic connection between CMEs and the Sun. Nevertheless, there is observational[35] and theoretical[36,37] evidence that CMEs maintain their magnetic connection to the Sun. Thus, the magnetic fields of CMEs impinging on the Earth provide the key physical connection between solar eruptions and strong disturbances in geoplasma space.

Advances in solar physics have been achieved largely by improvements in remote-sensing observations. Observations using different parts of the electromagnetic spectrum reveal different "faces" of the Sun.[38] The historical emphasis has been on understanding spectral data and images. Images—2-D projections of 3-D density structures—have led to numerous schematic concepts and mechanical analogs of dynamical scenarios ("cartoons") that are used to help interpet observations, numerical simulations, and theoretical models.[39] Image-based concepts, however, do not necessarily lend themselves to quantitative or testable understanding of data and physical mechanisms. Yet, the legacy of such concepts and biases influences the interpretation of new observations. A challenge in solar physics research is to revise the old pictures and construct new "faces" in quantitative agreement with new data and physical laws. The present paper will emphasize the macroscopic physics underlying eruptive processes, particularly the magnetohydrodynamic (MHD) forces responsible for observed CME dynamics and the evolution of CME magnetic fields.

Currently, a constellation of satellites observe the Sun and heliosphere from multiple vantage points. The two identitical STEREO spacecraft have, for the first time, directly observed CME dynamics from the Sun to 1 AU and in a number of events, measured CME ejecta magnetic fields and plasma parameters *in situ*. The Solar Dynamics Observatory (SDO; 2010-present)[40] provides high-resolution images of the Sun from Earth's vantage in multiple wavelengths. Flare X-ray emissions are monitored by the Geostationary Operational Environmental Satellites (GOES) system, and the SW properties, including the ejecta of CMEs, are measured by the Advanced Composition Explorer (ACE) placed at the L1 Lagrange point, $\sim 10^{-2}$ AU from the Earth toward the Sun. These datasets can now quantitatively constrain CME-EP-flare-MC models over the entire 1-AU region. As a result, new testable answers to long-standing questions are emerging: (1) what magnetic structures underlie CMEs, (2) what forces drive CMEs and determine their trajectories, (3) what physical processes connect the acceleration of CMEs and energy release in flares, (4) how CME magnetic field evolves through interplanetary (IP) space, and (5) how CMEs and MCs are related. The dynamics and structure of solar magnetic flux ropes play a key role in answering these questions.

There exists an enormous literature on the models of solar eruptions based on the so-called "standard model" (Sec. III A), which posits that the energy of eruption resides in the coronal magnetic fields and evolves into eruptive state by the slow photospneric boundary motion of the magnetic footpoints. The challenge is to determine what coronal structures and photospheric conditions can reproduce observed CME acceleration and propagation to 1 AU. There are several well-established models, which have been extensively reviewed[41] and are a textbook matter.[42] The present paper is *not* a compendium of such well-reviewed models nor is it a general review of solar eruptions, a subject matter too vast to consider in depth in a reasonably finite amount of space: rather, it presents an emerging new theoretical framework and examines how it answers outstanding questions, together with recent solar observations and the contrasting traditional interpretation of observed phenomena. The new theory focuses on the physical mechanism of CME eruption—the expansion of magnetic flux ropes, the driving forces, and the evolution of the ejecta magnetic fields—and produces new testable predictions for CMEs, flares, and MCs. The objective is to present a physics- and data-based "big picture" with sufficient depth and breadth to enable the reader to delve into the existing literature and critically examine physical issues. Of necessity, plasma physics will be key in the subject matter. The discussion will emphasize comparison of theoretical predictions and observed data. In this big picture, arguably the most important physical difference is that the standard paradigm places the energy of eruption in the corona while the new erupting flux rope (EFR) paradigm *allow* injection of magnetic flux from the convection zone. In terms of citations, primary/original references are emphasized, complemented by those that provide more recent observational findings.

In Secs. I A and I B, a brief history of the understanding of solar eruptions is given. Section II A summarizes the known properties of the solar atmosphsere, and Sec. II B provides specifics of observed eruptions. The reader who is familiar with the phenomenology of eruption may skip Sec. II and proceed to Sec. III, where the physics of CMEs is introduced and theory-data comparisons are discussed. The new theory is compared with the prevailing "standard model." Section IV examines in depth some important open questions in models of solar eruption, which will provide stimulating challenges to plasma physics. The canonical parameters of the solar atmosphere are given in Table I.

A. Solar eruptions: Overview

Solar flares are perhaps the most widely known manifestation of eruptions. They have been observed in various electromagnetic regimes for over a century and a half, and their spectroscopic properties are well-documented.[42–47] The X-ray flare in Fig. 1 was captured during the decay phase by the Soft X-ray Telescope (SXT)[48] on the *Yohkoh* satellite

TABLE I. Solar plasma parameters.[a] n = particle density; $\zeta \equiv n_e/n_H$ = degree of ionization, n_e = electron density, n_H = neutral hydrogen density; T = temperature (Kelvin); B = strong magnetic field; $V_A = B/(4\pi\rho)^{1/2}$ = Alfvén speed; β = plasma beta; λ_{mfp} = ion mean free path; ρ_L = characteristic ion Larmor radius; c/ω_{pi} = ion inertial length; and $\omega_{pi} = (4\pi ne^2/m_i)^{1/2}$.

	n[b] (cm^{-3})	ζ[b]	T (K)	B[c] (G)	V_A[c] (km s^{-1})	β[c]	λ_{mfp} (cm)	ρ_L (cm)	c/ω_{pi} (cm)
Corona[d]	5×10^8	$\sim\infty$	2×10^6	10–100	1000	0.01	6×10^7	100	700
Chromosphere	4×10^{10}	0.7	10^4	10^2–10^3	100	0.1	10	10	70
Photosphere	8×10^{16}	2×10^{-4}	5800	1k–3k	10	1	10^{-1}	1	10^{-1}
Convection zone[e]	1×10^{23}	$\sim\infty$	2×10^6	n/a	2.2×10^2	n/a	3×10^{-7}	n/a	7×10^{-3}

[a]Canonical values derived from remote observations. All quantities encompass a range of values.
[b]Ionization, $\zeta \equiv n_e/n_H$: Photospheric and chromospheric values based on Table 10 of Vernazza *et al.*[150] The optical depth at 500 nm (nanometer)—τ_{500}—decreases from $\tau_{500} = 1$ to $\tau_{500} = 0.1$ in about 150 km above the photosphere. Photospheric values are the approximate averages in this thin layer. Chromospheric values are given where $T \sim 10^4$ K ($\sim$2000 km above the photosphere).
[c]Values in regions with strong fields. Photospheric values are for sunspots (the LOS component). For the convection zone where no magnetic field is available, the sound speed C_S (model S) is given.[152]
[d]Estimated value at the base of the corona.
[e]At the base of the convection zone, approximately 2×10^5 km below the photosphere. The values are from the model of Christensen-Dalsgaard *et al.*,[152] the so-called model S. Specifically, the values are from $\mathcal{R}/R_\odot = 0.7143$ measured from Sun center. No model magnetic field information is available; in place of V_A, the sound speed is given: $C_S = (\gamma p/\rho)^{1/2}$, where the thermodynamic adiabatic index is $\gamma = 1.664$ at this depth.

(mission: 1991–2005).[49] In this image, the flare appears as an arcade of diffuse "loops," known as a "post-flare arcade" or a "post-eruption arcade" (solid arrow). (These historical terms are misnomers in that the arcade is part of the eruption.) An arcade on the west limb (dashed arrow) from an earlier eruption provides a view of such loops from the side. Figure 3 shows the disk-integrated soft X-ray (SXR) intensity $\mathcal{I}_{SXR}(t)$ measured by the GOES 8 spacecraft in the two wavelength bands, 1–8 Å and 0.5–4 Å. Note that $\mathcal{I}_{SXR}(t)$ contains no spatial information, but the Hα and EUV images during this period show no other eruptions. Thus, the peak in $\mathcal{I}_{SXR}$ is attributable to this flare. The maximum SXR intensity, occurring at ~12:20 UT, is one order of magnitude brighter than is seen in Fig. 1. Also seen in Fig. 1 are several relatively bright patches. They mark *active regions* (AR), which are regions of the order of 10^5 km characterized by strong (a few kilogauss) magnetic fields in the photosphere.

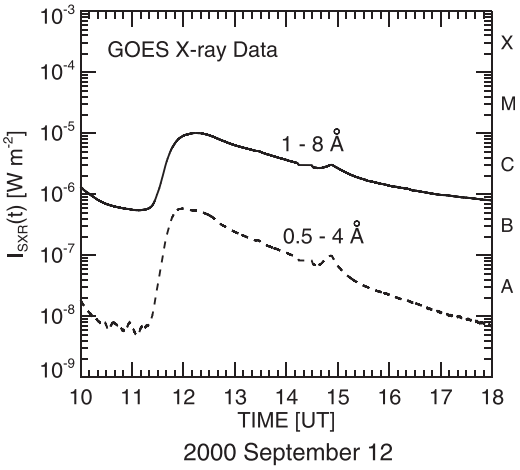

FIG. 3. Soft X-ray (SXR) intensity $I_{SXR}(t)$ detected by GOES-8, in units of W m^{-2} and averaged over 3 s. $I_{SXR}(t)$, integrated over the solar disk, peaked at about 12:20 UT with the FWHM duration is 105 min. After the peak, $I_{SXR}(t)$ decayed to the pre-eruption level in about 8 h. The flare classification (A, B, C, M, and X) is defined by the peak intensity in the 1–8 Å band and is given on the right axis. This is a small M-class flare.

The coronal emissions from such regions fluctuate and make up the bulk of the quasi-steady X-ray background.

The National Oceanic and Atmospheric Administration (NOAA) maintains a catalog of active regions. This flare occurred in the region designated as AR 9163 in this catalog. Flares are classified as *A*, *B*, *C*, *M*, and *X* according to the peak power in the 1–8 Å channel. The right vertical axis shows the decade of power for each class. With maximum $\mathcal{I}_{SXR} = 1.02 \times 10^{-5}$ W m^{-2}, this is an M-class flare.

Closely associated with flares, EPs had also attracted much attention,[50] and their observed morphology and dynamics are now well known.[43,51] Figure 4 is a snapshot from a sequence of Hα images of the eruption of a prominence, the so-called Grand Daddy prominence. The occulted solar disk provides the spatial scale. The large-scale "braided" features suggest nonlocal magnetic organization. The plasma parameters in quiescent prominences have been inferred using photon spectra and polarization. Temperatures are 5×10^3–1×10^4 K with non-thermal ("turbulent") broadening of spectral lines corresponding to 5–8 km s^{-1}.[52] Electron density of $n_e \sim 10^{10}$–10^{11} cm^{-3} has been obtained

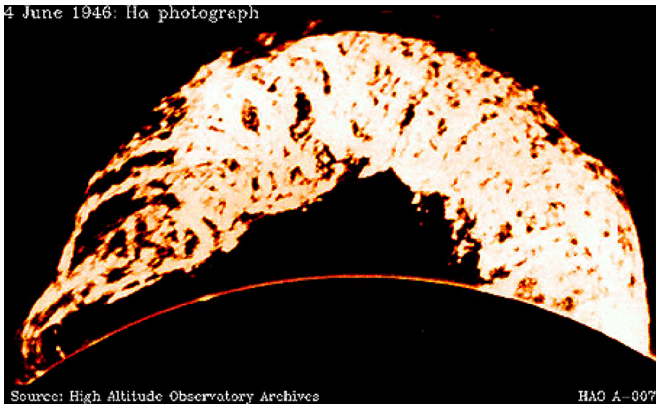

FIG. 4. The "Grand Daddy" eruptive prominence photographed on 4 June 1946. The solar disk is occulted. The image is interpreted as a 2D projection of a twisted or helical plasma structure organized by magnetic field. The Hα filtergram, one in a sequence capturing the eruption, was obtained by Roberts at Harvard College Observatory in Climax, CO.

from the measured Stark effect in hydrogen Balmer lines.[52,53] The estimated ionization is $0.05 < \zeta < 1$,[51]

$$\zeta \equiv n_e/n_H, \tag{1}$$

where n_H refers to the neutral hydrogen density. Various spectroscopic methods have yielded similar values of n_e in prominences.[54] The total plasma density is $n_e + n_H \sim 10^{12}$ cm^{-3}. The magnetic field in quiescent prominences is $|B| \sim 10$ G, reaching upwards of 20–30 G.[55–57]

While the corona was known to vary from eclipse to eclipse and rocket-borne observations separated by ~24 h had shown changes in the large-scale morphology,[58] such observations did not show motion. The rapid expansion of a large coronal structure at speeds greater than 1000 km s^{-1} evidenced by the OSO-7 data had not been expected.[59] The OSO-7 discovery of CMEs was followed by extensive observations from space-borne Skylab (1973, 1974),[60] the Solwind coronagraph on board the P78–1 satellite (1979–1981),[61] and Solar Maximum Mission (SMM; 1980–1982, 1984–1989),[62] and by land-based Mauna Loa Solar Observatory (MLSO) Mark III K-coronameter (MK3; 1980–2013).[63] In the early literature, the term "coronal transient" was used because it was not certain whether the observed changes were mass motion or transient waves, but it is now well-established that CMEs represent ejection of coronal mass.[64–69] The statistical properties of CMEs observed by the different instruments over several solar cycles are well documented.[64–67,70]

Figure 5 shows a sequence of images of a CME[71] observed by the SMM coronagraph whose FOV is a quadrant of the inner corona extending to 6 $R_\odot$. The dark disk is the occulter, and the white arc indicates the Sun. A short arrow located at the center of the Sun (⊙) points to the solar north. The quantity observed by a coronagraph is white light from the Sun that is Thomson-scattered by the free electrons in the optically thin corona.[72] Thus, bright features in these images show enhanced plasma density integrated along the LOS relative to the darker regions. Coronagraph data contain no information on the spatial distribution of electrons along the LOS: at each pixel, the observed quantity is $\int D_T n_e(s) ds$, where D_T is the Thomson scattering function, and $n_e(s)$ is the free-electron density along the LOS. There is no temperature information in D_T or n_e. These images were obtained using a broadband filter centered at 5175 Å (green) with a bandpass of 350 Å.

In an influential study, Illing and Hundhausen[71] described this event and identified several morphological features of CMEs. Figure 5(a) (10:04 UT) shows the pre-eruption "helmet streamer" (arrow) that had been slowly expanding for approximately one day. Streamers refer to bright radial structures along which coronal material is thought to be streaming from the Sun; "helmet" refers to the bulge at the base of the streamer. At 11:54 UT (panel b), the helmet was expanding more rapidly, manifesting three parts consisting of the bright rim or CME loop (arrow) encircling a relatively dark "cavity" and a bright "core." As the CME expanded, it maintained the three-part morphology (panel c). By 13:10 UT, the bright loop had moved out of the FOV, and the expanding core had revealed its internal structure. The "knotty" and braided

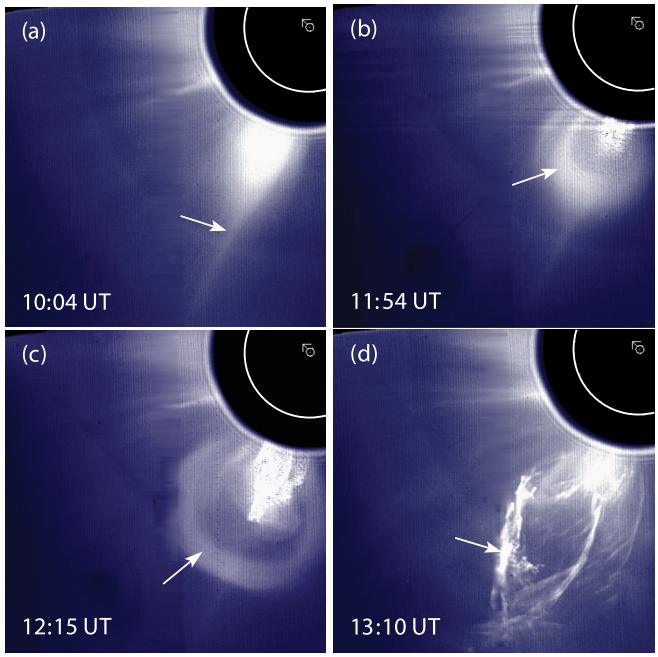

FIG. 5. SMM coronagraph images of an erupting CME on 18 August 1980.[71] The images were taken using an unpolarized $\Delta\lambda = 350$ Å bandpass filter centered at $\lambda = 5175$ Å(green). The SMM observed one quadrant at a time, with Sun center denoted by ⊙ and a short arrow pointing to the solar north. The white circular arc is the solar disk. The brightness measures the LOS-integrated columnar content of free electrons. The occulter (black circle) has a radius of 1.63 $R_\odot$. Certain artifacts have been removed. Courtesy of the High Altitude Observatory. (a) Shortly before the main eruption phase. The arrow points to the "helmet stream." (b) The expanding bright rim of the CME (arrow) enclosing a relatively dark "cavity" and a relatively bright "core." The core can be traced to an erupting prominence. (c) The rim-cavity-core structure maintains the relative spatial relationships. (d) The leading edge (LE) of the CME has expanded out of the field of view (FOV), and the core has unwound itself to reveal the intricate braided density features.

features (arrow) are similar in appearance to those in an Hα observation of this event[71,73] and are reminiscent of the features in Fig. 4. The mass of the CME loop was estimated to be comparable to the mass previously in the helmet. This was interpreted as evidence that the CME loop was formed by the coronal material expelled by the expanding cavity. Here, CME/EP mass is estimated from the Thomson-scattered intensity, assuming that the mass is concentrated near the plane of the sky where the scattering function is peaked.[72] The bright core in a CME-EP structure is interpreted as the coronal counterpart of the prominence observed in Hα.[74] At this point, the prominence plasma was estimated to be about 95% ionized. This type of CME, an eruption preceded by slow expansion of a helmet streamer and disappearance thereof, came to be known as "streamer blowout"[67] and "streamer disruption"[71] events.

The three-part morphology was interpreted as a 2-D projection of a 3-D density shell with approximate rotational symmetry in which the relatively long LOS paths through the dense shell [Fig. 6(a)] lead to the bright loop: the interior of the shell is the cavity, with the prominence material (not shown for simplicity) located inside the dome. The importance of this concept is that it structurally tied the CME, cavity, and associated EP together, pointing toward a more

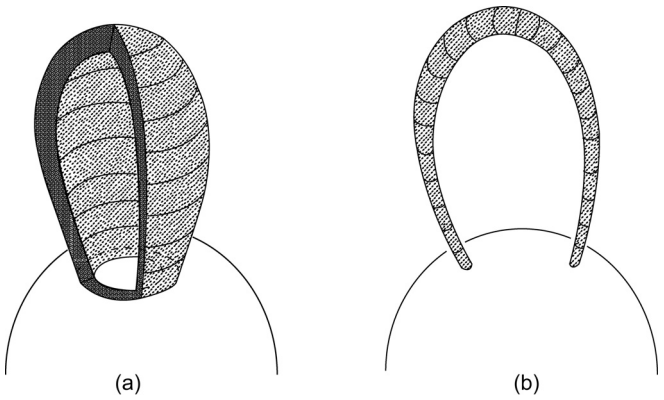

FIG. 6. Schematic of possible CME geometries in three dimensions. (a) Shell or bubble of dense plasma, the consensus view of the SMM era (1980s and 1990s). (b) Loop of dense plasma, a concept based on Skylab observations. Loops are characterized by minor radius a and major radius R. The thickness of the CME loop would be $2a$. Drawings based on Fig. 5.15 of Ref. 69.

unified understanding of CMEs and EPs. In an earlier concept, the bright CME loop [arrow, Fig. 5(c)] was thought of as a thin current loop,[75–77] schematically shown in Fig. 6(b). This configuration was modeled using a simple metallic current loop (minus tensile strength)[76] but did not include the cavity and prominence as integral elements.

Perhaps the strongest evidence supporting the hollow-dome structure came from the observation of a so-called "halo" CME[78] appearing as a relatively bright, nearly circular halo around the Sun. This was interpreted as the 2-D projection of an Earth-directed dome. Statistically, the angular widths of CME cavities showed no significant dependence on how the underlying filaments were oriented.[79,80] Assuming zero density in the cavity and estimating the contrast between the bright loop and the dark cavity, the size of the cavity in the direction of the LOS was estimated to be comparable to the transverse width of the cavity.[81,82] It was noted[71] that the thickness of the observed CME loops did not increase as described by the thin loop models,[75,76] i.e., as $a(t) \propto R(t)$, where $a(R)$ is the minor (major) radius of a loop. These studies helped establish the consensus view of the SMM era that the bright CME loop is an expanding shell,[69] not a thin planar loop.

The above interpretations were based on 2-D images of 3-D density structures and are inherently non-unique. Indeed, neither the three-part dome[69,71] [Fig. 6(a)] nor the thin planar loop[75,76] [Fig. 6(b)] proved to be the correct interpretation. An important new constraint emerged in the form of CME dynamics observed by the newly launched Large Angle and Spectrometric Coronagraph (LASCO).[83] LASCO is a set of three coronagraphs (C1, C2, and C3) on board the Solar and Heliospheric Observatory satellite (SOHO; 1996–present),[84] and has a then-unprecedently large FOV of radius 32 $R_\odot$ (Sun-centered). The large FOV and high sensitivity enabled detailed observations of CME acceleration and subsequent propagation through the inner heliosphere. Given this development, theoretical calculations of toroidal *magnetic flux rope* dynamics[85,86] were carried out and compared with observed CME dynamics, yielding good agreement throughout the LASCO FOV.[87] This pointed to a particular 3-D flux rope configuration—distinct from the earlier thin planar loops [Fig. 6(b)]—and a specific force as the physics underlying the CME phenomenon. This has led to much new research on flux-rope CMEs, and it is now generally accepted that CMEs are expanding flux ropes.[88–93]

In their simplest form, flux ropes are self-organized plasma pinches (Sec. III D), and the appellation refers to the braided (twisted) "ropes" of helical magnetic field "lines" characteristic of such structures. The magnetic fields of CMEs, however, still cannot be observed. This gap may be indirectly filled by observed dynamics because the expansion of CMEs, if they are flux ropes, must be consistent with calculated flux-rope dynamics.[87,94–96] Thus, the observed CME dynamics—in conjunction with physical models—serve as an added constraint on the interpretation of data. Coronagraph data also cannot determine if a flux rope exists prior to the eruption. Recent studies show evidence of pre-eruption cavities[97,98] and flux ropes,[99] supporting the flux-rope hypothesis in the earliest stages of eruption. This also suggests that CME cavities and bright rims are not necessarily caused by expelling the coronal material as previously thought.[71]

Occasionally, CMEs observed by multiple instruments show no identifiable flares (in X-rays) or EPs (in EUV, Hα) associated with them.[100] Such ("stealth") CMEs are nearly always slow. Transition Region and Coronal Explorer (TRACE) also detected a prominence rising up to a maximum height in the low corona and draining back down (seen in Hα) with no CME counterpart in the corona.[101] Such events, referred to as "failed eruptions," appear to be common.[102,103] In some events, seemingly only part of a filament is seen to disappear ("partial eruption"), which has been modeled as a 3-D flux rope separating into two parts via reconnection.[104] These new observations have significantly refined the knowledge of the range of the CME phenomenon.

B. Solar eruptions and space weather: Sun-Earth plasma connection

Approximately 17 h after the 1859 flare,[105] large disturbances in ground-level magnetic fields and bright aurorae were observed worldwide even at low latitudes,[1,106–108] but the possible flare-aurora causal connection—even its existence—remained a matter of speculation for over a century. The early proposals hypothesized corpuscular agents. On the basis of the recurrent auroral activities correlated with sunspots rotating into Earth-directed positions, Maunder thought that "electric particles" could be expelled from sunspots, reaching the Earth and causing aurorae.[109] Chapman and Ferraro[110] proposed that neutral streams of charged particles accelerated in solar flares were responsible for aurorae. The existence of particles streaming from the Sun (not necessarily from flares) was inferred by Biermann from comet tails that are directed away from the Sun regardless of the direction of the comet motion.[111,112] Chapman constructed a model of a static and unmagnetized corona extending past the Earth based on the high thermal conductivity of a fully ionized plasma,[113] suggesting an explanation for the high

temperature of the upper ionosphere. Parker, who coined the term "solar wind," showed that there is no static equilibrium solution with vanishing asymptotic pressure and constructed a model solar atmosphere with steady-state outflows sustained by an assumed heating function.[114] The model includes the solar magnetic field carried by the expanding plasma, leading to the configuration with spiral IMF "lines."[115,116]

Shortly afterwards, the Soviet satellite Luna 1 detected a stream of charged particles from the Sun in IP space,[15] confirming the existence of the SW. Detailed measurements were made of the IMF and SW plasma parameters by Pioneer V[16] and Mariner 2.[17] The large-scale structure of the IP medium at various heliocentric distances is now well documented,[117,118] including a view of the SW out of the ecliptic plane.[119] The typical SW speed is $\sim$400 km s^{-1} at low latitudes, which is the "slow" component, and is $\sim$600 km s^{-1} at the high latitudes, which is the "fast" component. Near solar minimum, the fast wind can extend down to the ecliptic plane at 1 AU. Although the mechanisms for the heating function—a key question in SW physics—have yet to be identified, the current understanding of the SW is substantially based on Parker's model. Instead of local heating, nonlocal thermal conduction from the hot corona through the nearly collisionless SW medium may play a significant role.

As mentioned earlier, CME ejecta (i.e., MCs) are now known to be the primary SW structures responsible for large geomagnetic storms. Figure 7 (top) shows a 2.5-day period of IMP-8 satellite SW data at L1, illustrating a prototypical MC at 1 AU and its relationship to such a storm. Panels (a) and (b) show, respectively, the B_y (east-west) and B_z (north-south) components of the IMF, and panel (c) shows the rotation angle $\vartheta(t)$ of the magnetic field vector in the y–z plane, defined by

$$\vartheta(t) \equiv \sin^{-1}(B_z/B_{yz}), \tag{2}$$

where $B_{yz}(t) \equiv (B_y^2 + B_z^2)^{1/2}$, and $+x$ points sunward from the Earth. Here, $|\vartheta| = 0$ corresponds to $B_z = 0$ ($B_y \neq 0$) and $|\vartheta| = \pi/2$ to $B_y = 0$ ($B_z \neq 0$). These plots show that the IMF fluctuated with the typical amplitude of $\sim$5 nT prior to 00:00 UT, 14 January 1988, when the IMF increased and turned northward ($B_z > 0$, $\vartheta > 0$) for about 16 h. It then turned and remained southward ($B_z < 0$, $\vartheta < 0$) for the next 18 h, reaching -20 nT. The maximum of $|\mathbf{B}_{yz}|$ coincided with maximum $|B_y|$ and $B_z = 0$. The observed magnetic field is consistent with that of a simple magnetic flux rope with its axis ($B_z = 0$) in the ecliptic as illustrated in Fig. 7 (bottom), a pinch having both an axial (B_y) and azimuthal (B_z) magnetic field components. (Also see Fig. 8 of Ref. 27.) The period between the maximum and minimum ϑ (vertical lines) is the MC as defined by Burlaga *et al.*, which is the current channel of the flux rope.[86] At the leading edge (LE) of the structure, the measured SW plasma speed (panel c) increased to about 700 km s^{-1}, then decreasing to about 500 km s^{-1} and roughly the earlier background conditions ($\sim$10:00 UT, 15 January 1988). This is consistent with the minor radius of the magnetic flux rope expanding at $\sim$100 km s^{-1} about its axis ($B_z = 0$). The proton density n_p in the MC is shown in panel

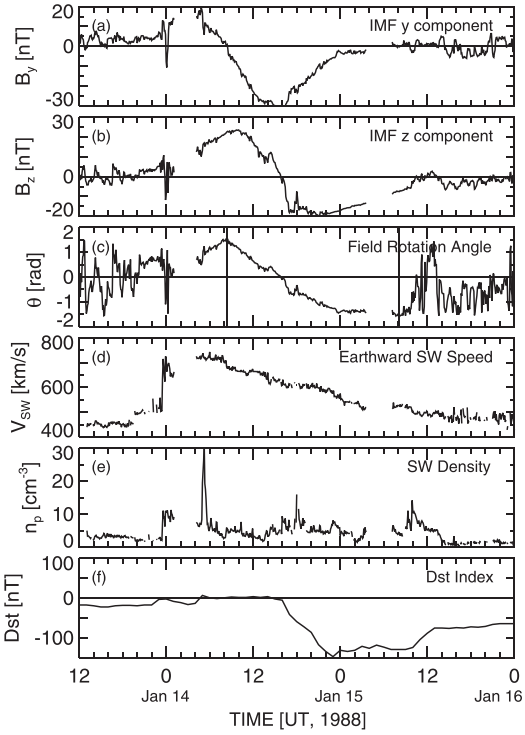

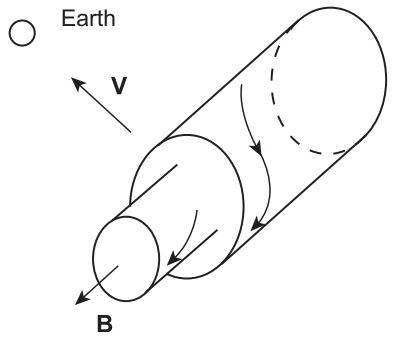

FIG. 7. Solar wind (SW) data measured by the IMP-8 satellite at 1 AU on 13–16 January 1988 (left). An organized magnetic structure—a magnetic cloud (MC)—is inferred (schematic, right). (a) B_y (east-west) component, in the Geocentric Solar Ecliptic (GSE) coordinates ($+z$ is north in the ecliptic and $+x$ points from Earth to the Sun). Data gaps are left blank. (b) B_z (north-south) component. (c) The IMF "clock angle" defined by Eq. (2), showing a smooth field rotation of $\delta\vartheta \simeq \pi$ in 36 h. The vertical line segments demarcate the MC proper,[27] corresponding to the current channel of the larger flux rope. (d) The SW speed V_{SW} toward the Earth. The nearly linear decrease in V_{SW} indicates that the structure was expanding. The duration of 36 h (00:00 UT, January 14–12:00 UT, January 15) and average $V_{SW} \simeq 600$ km s^{-1} imply a spatial size of $\sim$1/2 AU. (e) Proton density, n_p. Proton temperature (not shown) in the MC: $T_p \sim 5 \times 10^4 - 1 \times 10^5$ K. (f) Associated *Dst* index value. The maximum excursion of $Dst = -150$ nT indicates a moderate geomagnetic storm. $Dst(t) < 0$ is most directly correlated with $B_z(t) < 0$. The increases in V_{SW} and n_p were not directly associated with significant changes in *Dst*.

(e). The proton temperature was $T_p \sim 5 \times 10^4 - 1 \times 10^5$ K (not shown). Overall, the data show a large plasma structure that was well organized by a magnetic field much stronger than the background IMF. At an average speed of 600 km s^{-1} and observed duration of 36 h, the structure had a perceived size of $\sim$1/2 AU. MCs are often so well organized that it is possible to infer the magnetic field profile of one given only 10%–15% of the data near the LE.[120–122]

Figure 7(f) shows the *Dst* ("Disturbance storm time") index[123] for this time period. This is the standard measure of geomagnetic storm strength: the more negative *Dst* is, the stronger the storm. *Dst* is an hourly average of the ground magnetic field relative to the quiet state ($Dst = 0$), computed monthly using the data from several magnetometer stations around the globe. It is clear that $Dst(t)$ is most closely correlated with the southward $B_z(t)$. It reached the peak disturbance level of $Dst \simeq -150$ nT, a moderately strong storm. The substantial increase in the SW ram pressure ($\rho_{SW} V_{SW}^2$) did not cause *Dst* to deviate from the quiet-time values ($Dst \approx 0$). A storm typically decays in several hours to a few days after the passage of southward IMF structures.

The above relationship between the IMF and *Dst* is consistent with the hypothesis that the southward IMF ($B_z < 0$) reconnects with the Earth's magnetic field, resulting in large-scale disturbances in the magnetospheric fields and energetic particles producing aurorae.[124] The weaker but recurrent form of storms is correlated with high-speed SW streams (not associated with flares or CMEs) whose source regions rotate with the Sun.[125,126] While it had been known in magnetospheric physics that major geomagnetic storms are caused by strong southward IMF,[24–26] the adage that flare-generated particles and SW disturbances (e.g., shocks[127]) cause aurorae and geomagnetic storms persisted in the solar physics literature. Only recently did CME ejecta and their magnetic fields come to be recognized as the primary solar drivers of large storms.[128,129] Solar energetic particles (SEPs)—electrons and protons accelerated to more than tens of MeV—can impinge on the Earth for days, much longer than flare durations; a major contribution to SEPs comes from particles accelerated by shocks generated by expanding CMEs.[130] *Aurora borealis* (northern lights) and aurora australis (southern lights) result from particles accelerated in the nightside magnetotail.[131,132]

The interplanetary MCs are usually modeled as force-free ($\mathbf{J} \times \mathbf{B} = 0$) flux ropes.[31,133–136] The specific form used is the Lundquist solution given by $\mathbf{J} = \lambda \mathbf{B}$ with $\lambda = const.$[137] To the lowest order, the Bessel function profiles can approximate many observed MC profiles, but the Lundquist solution has a fixed ratio of $B_t(r = 0)/|B_p|_{max} \approx 1.7$. The observed MCs exhibit a wide range of values for this ratio. The force-free simplification is usually given the physical rationale that the plasma β of MCs is small. A small $\beta \ll 1$, however, is not equivalent to $\mathbf{J} \times \mathbf{B} = \nabla p = 0$. Accordingly, non-force-free MC flux ropes have been constructed (no ambient pressure treated).[139] Non-force-free flux ropes in equilibrium in an ambient medium of finite pressure (p_a) subject to the "minimum complexity" constraint have been obtained.[138] Non-force-free and force-free Lundquist profiles need not be remarkably different,[138] but flux ropes generally do not evolve in a force-free manner (Sec. III F 2).

Geomagnetic storms with large-amplitude disturbances in magnetic fields and ionospheric plasma density can adversely affect micro-electronics and globally integrated technological infrastructure; outages of communications and navigation systems, air traffic control system, and electric power grids are but a few examples.[140–143] SEPs do not cause storms but are a significant hazard to spacecraft, astronauts, and airline crew. Thus, understanding the physical mechanisms of CME eruption, subsequent propagation and evolution of the magnetized ejecta, and the physical processes by which magnetospheric dynamics are driven by CME ejecta has become a grand-challenge scientific objective of societal importance, providing a focal point of solar-terrestrial plasma physics, sometimes referred to as "space weather."

Although it is now generally accepted that MCs are the CME ejecta in the heliosphere, i.e., the structures resulting from CME eruptions, it should be remembered that this connection was mostly statistical, not direct, until the STEREO mission because the propagation of a CME from the Sun to a point of observation could not be fully observed. In early research, counterstreaming SW electrons (identified by pitch-angle distributions) were used as a proxy for the interplanetary manifestation of the CME ejecta largely based on statistical evidence.[144] Such SW signatures were often referred to "CME," "solar wind CME," or "interplanetary CME (ICME)." Other interplanetary particle signatures of CMEs have been studied, but the association of such plasma particle features with CME structures is ambiguous (e.g., see Ref. 145). In the present paper, the term "CME" will be used to denote the structure observed by coronagraphs, while "CME ejecta" will denote the heliospheric counterpart of the evolved CME; CME ejecta and magnetic clouds will be used interchangeably depending on the context. The focus will be on the magnetic field structure. The term "ICME" is often used in the literature to denote disturbed SW features that are presumed to result from solar eruptions but do not have flux-rope like magnetic fields.

II. OBSERVATION OF THE SUN: DIFFERENT FACES OF THE SUN

Solar observations are remote-sensing measurements. In interpreting such data, it is important to understand the underlying assumptions used to relate the detected photons to the physical quantities of interest. Here, solar observations relevant to eruptions are summarized with a brief historical account of the observational advances.

A. Solar atmosphere

1. Photosphere

In ancient times, the solar disk was regarded as an "unblemished" circle. The solar surface, however, is not unblemished. Dark "spots" on the disk are occasionally observed. They were recorded by Chinese astronomers in official imperial documents dating back to 28 before the current era (BCE). Written descriptions of spots exist from the fifth century BCE.[146] These dark spots are now understood to have been large *sunspots* or sunspot groups, which are visible to the unaided eye under certain conditions, e.g., through haze, thin cloud, or dust that acts as a neutral density filter. Telescopic observations of sunspots started around 1610,[147] yielding detailed drawings of sunspots. Three centuries later, George E. Hale discovered the Zeeman splitting in the photon spectra from sunspots,[148] demonstrating the existence of

solar magnetism, arguably the most important discovery in modern solar physics.

The solar disk is the projection of the hemispherical *photosphere* ("light sphere"), the visible solar "surface." Below the photosphere is the *convection zone* in which the energy generated by nuclear fusion in the core drives convective plasma flows that carry the energy to the surface, where the upwelling plasma radiatively cools and begins to flow down; the photosphere is where the atmosphere makes the transition from an optically thick (optical depth $\tau = 1$) to an optically thin state. It is, therefore, the inner most layer of the solar atmosphere that can be directly observed. Its effective (black-body radiation) temperature is $T_s \simeq 5800$ K ($kT_s = 0.5$ eV). Here, subscript s refers to the photospheric "surface," which is a highly nonuniform and dynamic layer with an estimated thickness of ∼150 km (i.e., one gravitational scale height). This is also approximately the photon mean-free-path in the photosphere.[149] The canonical particle and mass densities are $n_s \sim 10^{16}$–10^{17} cm^{-3} and $\rho_s \sim 2 \times 10^{-8} - 10^{-7}$ g cm^{-3}, respectively. The temperature decreases to $T_{min} \simeq 4000$ K at ∼500 km, where $n \sim 2 \times 10^{15}$ cm^{-3}.[150]

The photosphere is not a fixed surface, and its position and observed properties are determined by the last interaction of the detected photons with the optically thick plasmas. The photosphere is weakly ionized with ionization of $\zeta \sim 10^{-4}$.[150,152] Below the surface, both n and T increase with depth: at the base of the convection zone, the estimated values are $n_{cz} \sim 10^{23}$ cm^{-3}, $\rho_{cz} \sim 10^{-1}$ g cm^{-3}, and $T_{cz} \sim 2 \times 10^6$ K (2 MK), corresponding to $kT_{cz} = 172$ eV, so that $p_{cz} \sim 6 \times 10^{13}$ dyn cm^{-2}.[152] For comparison, the Earth's neutral atmosphere at 1 atm has particle density ∼2.5 $\times 10^{19}$ cm^{-3} and mass density ∼1.2×10^{-3} g cm^{-3}. The weakly ionized ionosphere has daytime maximum electron density $n_e \sim 10^6$ cm^{-3} and temperature 0.2 eV at 250–300 km (F layer). This region is inside the hot but tenuous magnetosphere ($T \sim 1$ keV, $n \sim 1$–10 cm^{-3}).

The most prominent features in the photosphere are sunspots, which appear dark due to the relatively low temperature, $T_s \sim 4500$ K (viz., the Stefan-Boltzmann law, $I_s \propto T_s^4$). Figure 8 shows one half of a sunspot, observed by the Swedish 1-m Solar Telescope (SST) on La Palma in the Canary Islands.[153] The dark central region is the *umbra*, which is surrounded by filamentary features making up the *penumbra* of the spot. The axes are marked in units of 1000 km, indicating that spatial features of ∼100 km are resolved. This is the current limit of resolution.[154] The image also shows the presence of relatively bright small features ("dots") containing dark cores well inside the umbra. They are interpreted as the footpoints of penumbral filaments aligned in the LOS direction. These filaments, many of which also contain dark cores, are assumed to be thin magnetic flux ropes fanning out as they rise into the low pressure corona, but there is no established interpretation for the dark cores. Given the small scales in photospheric plasmas (Table I), these filamentary structures support the expectation that fundamental physical processes in the photosphere occur on scales smaller than 100 km.[153] The cellular features beyond the penumbra are *granules* that are the tops of convection cells. The darker edges of granules correspond to colder plasmas flowing downwards. Granules are typically ∼1000 km across and last several minutes. The granular size is determined by the upflow and radiative cooling of the convection cells.

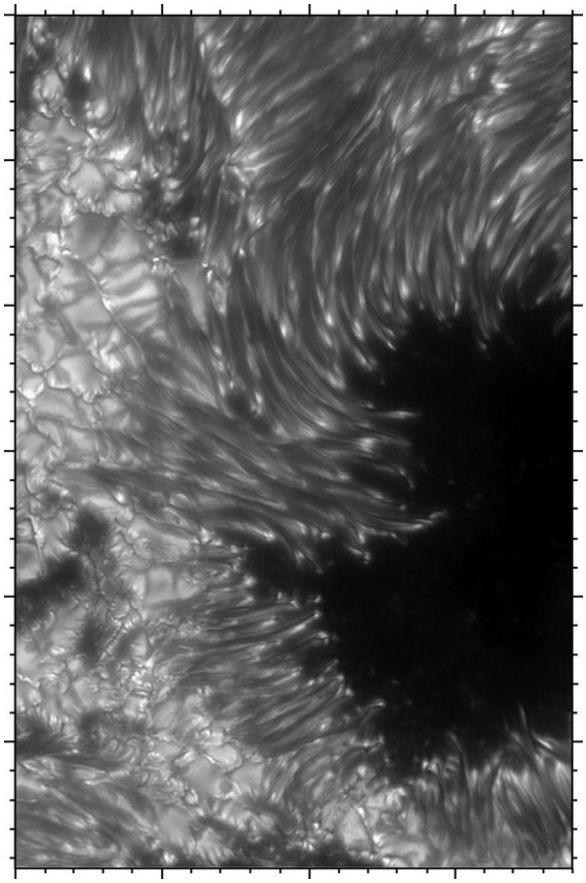

FIG. 8. Image of a half of a sunspot in Active Region 10 030 observed by the Swedish 1-m solar telescope (SST). This image, obtained using adaptive optics and a filter centered at 4305 Å, resolves features down to slightly less than 100 km. The tick marks are placed in units of 1000 km. The spot consists of the dark *umbra* ($T_s \approx 4500$ K) and the *penumbra*, characterized by filamentary rays emanating from the umbra. The penumbral filaments are presumed to be organized by magnetic fields. Most of these filaments—width of 150–180 km resolved by 5–6 pixels—contain dark cores. This image suggests that the sunspot consists of highly localized and filamentary elements. Beyond the penumbra, cellular features of ∼1000 km across are evident. They are referred to as *granules*, corresponding to the top of convection cells. Reproduced with permission from Scharmer *et al.*, Nature **420**, 151 (2002). Copyright 2002 Springer Nature.[151]

The convection zone cannot be directly observed because photons are collisional at all wavelengths. This is unfortunate because the ultimate source of magnetic energy—the solar dynamo—is thought to reside deep in the convection zone (e.g., Ref. 155). Nevertheless, the large-scale structure of the convection zone such as its depth—approximately 2×10^5 km—has been inferred using *helioseismic* techniques based on observations of oscillations in the photosphere.[152,156–159] Recent work is beginning to yield quantitative insights into magnetic structures in the convection zone below active regions.[160]

Most of the radiative energy from the Sun ($\mathcal{L}_\odot \simeq 3.8 \times 10^{33}$ erg s^{-1}) is in "white light" at ∼5800 K. Figure 9(a) shows a white-light image of the Sun obtained by the Kanzelhöhe Solar Observatory (KSO) in Austria. The

observed intensity exhibits a pronounced decrease toward the limb due to the so-called "limb darkening" effect:[161] the disk center is relatively brighter because photons from deeper and hotter layers of the photosphere reach the observer, and near the limb, photons have longer paths through an opaque medium. Thus, observed photons from different parts of the disk correspond to slightly different heights in the atmosphere. The white square marks a compact group of large sunspots. The light and dark mottled appearance is caused by temperature—thus intensity—variations on the granular scale of ~1000 km (convolved with noise).

Figure 9(b) is a photospheric magnetogram obtained by the Michelson Doppler Imager (MDI)[162] on SOHO. This image, captured shortly after Fig. 9(a), is a map of the LOS, or *longitudinal*, component of the magnetic "field" inferred from the longitudinal Zeeman effect (Stokes I and V). Here, white is positive (toward the observer) and black is negative (away from the observer). The magnitude is shown on a grey scale. The image shows that strong LOS field (both black and white) occurs as small unipolar features clustered into large bipolar regions. In one such region, marked *A*, a thick white curve is drawn to indicate the *polarity inversion line (PIL)* or *neutral line* across which the LOS polarity is reversed. Both terms are used in the literature, but in deference to the prevalent use of the term "neutral line" to refer to field-reversed current structures, we will use the term "polarity inversion line" (PIL). The LOS magnetograms do not detect unresolved magnetic flux of opposite polarity and do not contain information on the component perpendicular to the LOS. This transverse component requires linear polarizations from the transverse Zeeman effect (Stokes Q and U).[163] At disk center, the transverse component is horizontal in the surface. At the limb, it is the LOS component that is horizontal. Thus, a magnetogram gives different views of a given structure in different parts of the disk.[164] The transverse component given in a vector magnetogram has a 180° ambiguity and greater uncertainties than the LOS component. The former requires additional assumptions to disambiguate.

2. Photospheric magnetic field data

It is important to keep in mind that what is actually shown in a LOS magnetogram such as Fig. 9(b) is the *net* magnetic flux through each pixel because the circular polarization (Stokes V) from the unresolved positive and negative field elements cancels. Here, Stokes V is the intensity difference between the right- and left-handed circular polarization when observing along **B**. Thus, the "magnetic field" data are the pixel-averaged *net* flux per unit area, and "zero" field [grey in Fig. 9(b)] may result from cancellation of oppositely directed strong fields.[149] In addition, the inversion algorithms used to infer the strength of magnetic field from the measured Stokes data require a parameter, referred to as the *filling factor*, which is the fraction of the area occupied by unresolved magnetic fields within a pixel. If the filling factor, which is usually denoted by α, is assumed to be unity (as in calculations of LOS fields), the inferred field strength and flux are the lower limits. The thin penumbral filaments in Fig. 8 and the small plasma length scales (Table I) suggest that the filling factors in sunspots are much less than unity. The full-disk MDI image in Fig. 9 has angular resolution of 4″ (arcsec), where 1″ is 727 km on the solar surface, so that a pixel is approximately 3×10^3 km.

Furthermore, the longitudinal and transverse components are defined relative to the LOS. A given **B** vector will exhibit different longitudinal and transverse components if viewed from different angles. If a contribution to the vector **B** varies in time while the others do not, the measured flux will be the sum of the contributions from the time-varying and static components along the LOS. Thus, the relative magnitude of detectable changes will depend on the viewing angle with respect to the component that varies.

Photospheric magnetic fields are observed in small concentrations (unipolar patches), which disperse or disappear in time. The higher the spatial resolution, the greater the amount of magnetic flux (energy) and magnitude of field that can be detected. A detailed analysis of flux concentrations in quiet regions (high-resolution MDI data, resolved to 0.6″) showed that the smaller the patch size, the faster the dispersal process.[165] The average (quiet-region) concentrations, $\sim 2.5 \times 10^{18}$ Mx, were found to last 20 min, with larger ones lasting up to approximately 10 hrs (4×10^4 s). Estimates based on data and numerical simulations suggest that flux concentrations occur on scales at least one order of magnitude smaller than can be resolved at this time (100–200 km), possibly smaller than 20 km.[167,168] There is evidence that

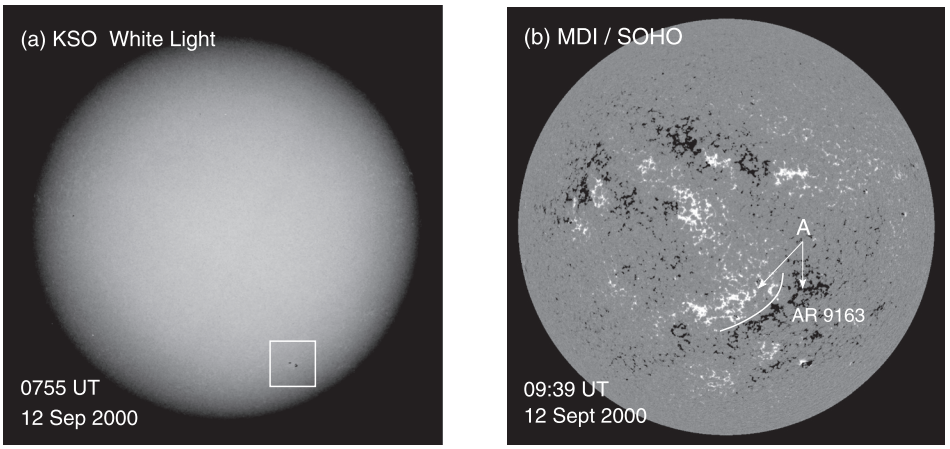

FIG. 9. Different faces of the Sun: the photosphere. (a) White light (KSO). White square encloses a group of large sunspots. North is up. (b) Magnetic field component along the LOS (MDI SOHO). White/black indicates the field polarity out of/into the solar surface, respectively. Region *A* is NOAA Active Region 9163. The polarity inversion line (PIL) is indicated for one active region. Angular resolution is 4″, where 1″ (arcsec) corresponds to 727 km on the solar surface.

photospheric magnetic fields follow a scale-free power law (frequency versus flux) on all currently observed scales over five decades.[169] This implies that the photospheric magnetic flux budget may be significantly underestimated.[167] Much of the small-scale magnetic features and their dynamics is understood on the scale of 100–200 km, obtained by, for example, the Solar Optical Telescope (SOT)[170] on board *Hinode*[166] and the SST (e.g., Fig. 8). In addition to the SST, ground observatories using adaptive optics are now routinely producing high-resolution images of the solar surface. The newly operational New Solar Telescope (NST) of the Big Bear Solar Observatory (BBSO) with adaptive optics has a 0.083″ spatial resolution (60 km), and the next-generation Daniel K. Inoue Solar Telescope (DKIST) (under construction) of the National Solar Observatory (NSO) with adaptive optics is expected to have a better resolution. High resolution observations, however, are limited by the small FOVs. For example, the NST spectropolarimeter—Near-Infrared Imaging Spectropolarimeter (NIRIS)—has an FOV of 85″ across ($\sim 6 \times 10^4$ km). The slit-based Vector Spectromagnetograph (VSM) of the NSO can image the solar disk in 20 min at 1″ resolution (2048 pixels across).[163]

3. Corona

From the photosphere to the base of the corona, the atmospheric properties change by many orders of magnitude. There is a thin boundary region consisting of the *chromosphere* ("color sphere"), an irregular layer of average thickness ~2500 km, and the *transition region*, which is an even thinner sheath region between the chromosphere and the corona. Identified by the characteristic Hα radiation, the chromosphere has the canonical temperature $T \sim 10^4$ K and density $n \sim 10^{11}$ cm^{-3}.[150] It is partially ionized with ionization $\zeta \sim 10^{-3}$ in the lower chromosphere and $\zeta \sim 1$ at the top (Table I). The transition region is nearly fully ionized ($\zeta \gg 1$) and is identified by EUV emissions at $\sim 10^5$ K. The plasma density rapidly decreases to $n_c \simeq 10^9$ cm^{-3} at the base of the corona where the temperature is $T_c \simeq 1$ MK–2 MK ($kT_c = 86$–172 eV). In active regions, it is significantly hotter, reaching as high as ~6 MK (0.5 keV).[42] High coronal temperatures ($T > 10^6$ K) have also been inferred from the presence of the Fe XIV and Fe X lines and from the gravitational density scale height of $H_g = 2kT/m_i g \sim 1R_\odot$ observed during eclipses.

Figure 10(a) is an Hα image of the Sun, showing the chromospheric layer of the atmosphere above the photosphere shortly after the magnetogram in Fig. 9(b) was obtained. Bright patches are called *plage* (French for "beach") and are a characteristic chromospheric signature of active regions with strong magnetic fields. Plage map to *faculae* in the photosphere below, which refer to much smaller bright patches. There are numerous dark filamentary features, referred to as *filaments*. They are dense and cool plasma structures in the low corona and absorb Hα radiation from below, giving them the dark appearance.[171,172] A large filament (P) lies above the PIL in region A [Fig. 9(b)]. When filaments are on the limb viewed from the side against the Hα-dark (fully ionized) corona, they appear as bright prominences radiating in Hα (e.g., Figs. 2 and 4). Filaments and prominences refer to the same structures viewed from different vantage points, and the two terms are interchangeable. Filaments can remain quasi-stationary for weeks and abruptly erupt.

Figure 10(b) is an image obtained by the Extreme Ultraviolet Imaging Telescope (EIT)[173] on SOHO shortly before Fig. 10(a). It is a map of EUV at $\lambda = 195$ Å, arising from Fe XII in the hot corona at $T \sim 1.5 \times 10^6$ K. The brightness is proportional to the LOS integration, $I_{EUV} \propto \int D_{EUV} n^2(s) ds$, where $n(s)$ is the EUV emitter density and D_{EUV} depends on the source plasma temperature and instrument sensitivity. Filaments are absorption features with similar appearances in both Hα and EUV [Figs. 10(a) and 10(b)].

Figure 1, obtained several hours after Fig. 9(b), shows that the axis of the X-ray arcade is aligned with the pre-eruption PIL. Other bipolar active regions are similarly associated with enhanced emissions in X-rays, EUV, and Hα (plage). When observed on or near the limb, bright EUV loops (thin flux ropes) are seen to extend into the corona [Fig. 10(b)]. This indicates that hotter, denser material can be confined by magnetic field into loops. Figure 11 shows a better resolved image of an arcade of thin loops in an active region after an eruption. This image was obtained by the Transition Region and Coronal Explorer (TRACE) satellite[174] (1999–2010) at $\lambda = 171$ Å, which is primarily at $T \sim (1-2) \times 10^6$ K but may contain contributions from 10^7 K plasmas.[175] Such bright loop structures are typically

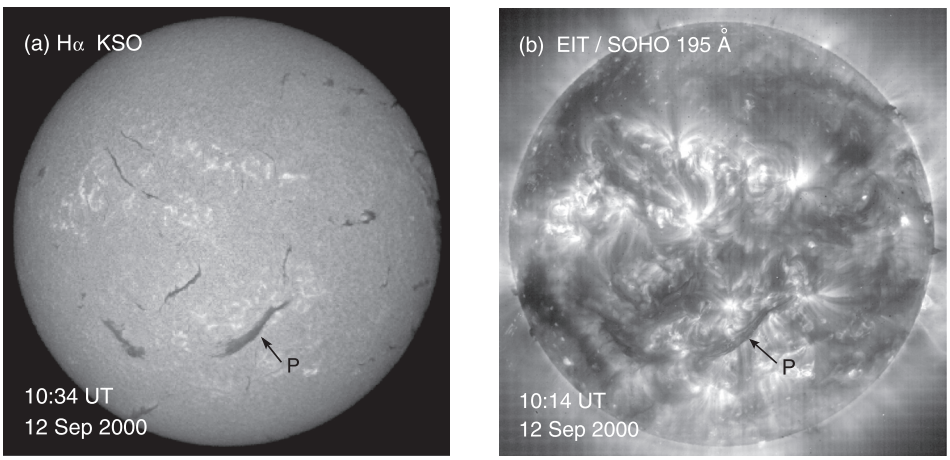

FIG. 10. Different faces of the Sun: the chromosphere and corona corresponding to the surface shown in Fig. 9. (a) Hα image (KSO). A large filament (P) in AR9163 is visible. (b) EUV image $\lambda = 195$ Å (EIT/SOHO. The filament in AR 9163 is visible as a dark absorption feature (P).

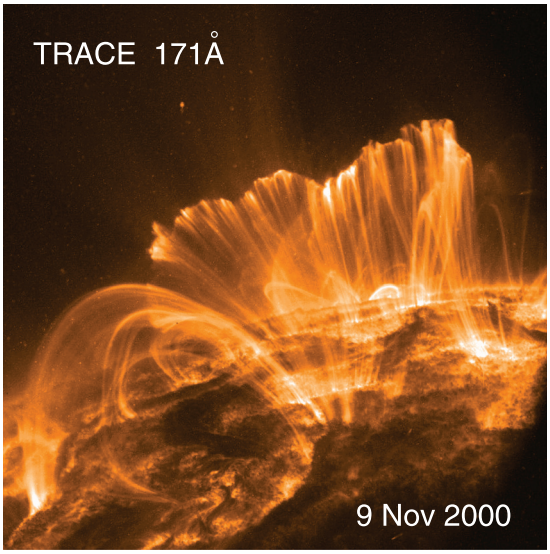

FIG. 11. An arcade of coronal loops observed by the transition region and coronal explorer (TRACE) satellite after a solar eruption. The image is taken at 171 Å corresponding to ∼1 MK. The plasma was already cooling from the height of flare. The spatial resolution is 0.5 in./pixel. One arcsecond (1in.) corresponds to ∼727 km on the solar surface. Data courtesy of the TRACE team.

quasi-stationary, occasionally buffeted by nearby eruptions causing characteristic damped oscillations.[176–181] Individual loops can show activities such as rapid variation in brightness associated with oscillations, which may be in both vertical and horizontal directions.

Thin plasma loops in X-rays and EUV were first extensively observed during the Skylab era (1970s) and led to a significant revision of the understanding of the corona: earlier, the corona was thought of as a nearly homogeneous atmosphere (Fig. 2),[182–184] but EUV[185] and X-ray[186] observations revealed that it is made up of loops at different temperatures around 6×10^6 K. These thin coronal loops are 10^4–10^5 km in height and exhibit near-uniformity along their axes[187,188] and are thought of as "field lines." Based on the assumption that the loops follow closely spaced current-free (potential) lines that fan out, the nearly uniform thickness—perhaps 30% thicker at the apex on the average—was regarded as inexplicable in terms of radiative and thermal properties.[188] The quasi-stationary loops are presumed to confine X-ray and EUV emitting plasmas, which suggests that they are thin current-carrying flux ropes. At 2 MK to 6 MK in active regions, the gravitational scale height is $H_g \approx (1-4) \times 10^5$ km. The observed thickness variation may be consistent with the magnetic forces balanced by the ambient pressure along a loop if it carries nonzero electric current. See Ref. 189 for a review of coronal loops.

The photosphere is often regarded as the Sun's surface, but it is merely an optical layer in the atmosphere where radiation becomes decoupled from the plasma. The entire region encompassing the dense convection zone, the tenuous corona, and the SW may be regarded as the Sun's plasma atmosphere, with the macroscopic plasma dynamics governed by the same basic MHD physics subject to different energy equations. The convection zone is heated from below by the radiative core, and the convective motion is describable by MHD coupled to gravity, radiative transfer, and solar rotation.[152,190–193] For observed plasma dynamics, the following ordering is generally valid:

$$\left(\frac{\rho_i}{\ell}\right)^2 \ll \frac{1}{\tau\omega_{ci}} \ll 1, \tag{3}$$

where ρ_i is ion Larmor radius, ℓ the relevant scale length, and τ the macroscopic dynamical time scale. Observable photospheric features resulting from magnetic structures rising through the photosphere have been modeled by MHD coupled with radiation.[191–193] In the corona above, the optically thick photosphere, radiation plays a negligible role in the macroscopic plasma dynamics, and standard non-radiative MHD is a good approximation.

4. Active regions

An active region is "born" as a pair of sunspots of opposite magnetic polarity, which is interpreted as the footpoints of a flux rope that has risen into the corona.[43,194,195] Often, multiple pairs of sunspots appear over a few days' time. This process has been extensively studied by MHD simulations.[192,196–199,201] A recent radiative MHD simulation of a single emerging flux rope replicated the appearance of extensive patches of small bipolar features in otherwise "quiet" photosphere around the new spots,[192] which were observed by the high-resolution *Hinode* SOT Spectro-Polarimeter (SP).[170] The bipolar features are much smaller than the underlying well-organized flux rope (Sec. IV D).

After emergence, the photospheric magnetic field of a new active region slowly disperses over larger areas. The compact cluster of spots in Fig. 9(a) (square) was a relatively new region. The large and diffuse extent of AR 9163 [*A*, Fig. 9(b)] indicates that this region had evolved for some time.

The plasma structure in the corona above an emerging or a newly formed pair of sunspots is not observable in white light against the solar disk. When an active region emerges near the limb, however, Hα observations show a complex of rapidly rising loops with plasma flows at a few tens of kilometers per second.[203] Such a structure is referred to as an *arch filament system* (AFS),[202] which also has a similar appearance in EUV.[178] Although a newly formed active region evolves over days, systems of loops and bipolar features appear over several minutes to a few hours,[43] indicating the timescale on which significant amounts of magnetic flux and energy of the order of an active region can emerge. It is thought that AFSs trace out the underlying emerging magnetic flux ropes,[204] which would leave numerous small bipolar footpoints. Until the *Hinode* SOT observation, little, if any, indication of such fine photospheric magnetic structures during flux emergence had been detected in magnetograms.

Because the photospheric pressure p_s is higher than the coronal pressure p_c ($p_s/p_c \sim 5 \times 10^5$, Table I), individual magnetic flux tubes in the photosphere (dimension ℓ_s) map across the chromosphere to larger coronal counterparts (dimension ℓ_c), by a factor of

$$\frac{\ell_c}{\ell_s} \sim \left(\frac{p_s}{p_c}\right)^{1/4} \tag{4}$$

in the transverse direction. Averaged across a magnetic structure supported by the local ambient pressure ($\mathbf{J} \times \mathbf{B} - \nabla p = 0$), one finds $p \sim B^2/8\pi$, be it in the corona or photosphere. The above scaling follows from $B\ell^2 = const$. Thus, the flux-rope footpoint at the base of the corona a_f maps to a region of the order of $a_s \sim a_f(p_c/p_s)^{1/4}$. If $p_s/p_c \sim 5 \times 10^5$, then $a_s \simeq 3.8 \times 10^{-2} a_f$. This is consistent with the interpretation that bright patches of chromospheric plage map magnetically to much smaller photospheric faculae. Conversely, small bipolar features in the photosphere correspond to much larger coronal loops.

Equation (4) assumes that the footpoints in the photosphere are similarly organized by the magnetic field as in the corona. Magnetized photospheric regions (e.g., sunspots), however, are typically made up of thin filamentary structures that rapidly expand into the corona (e.g., Fig. 8), each of which may be treated as a flux rope. Fields in the photosphere likely are not monolithic but are filamented beyond the limit of resolution.[169] The above scaling then applies to individual structures.

B. Solar eruptions: A unified view

Early observations of CMEs showed that the three eruptive processes—CME, EP, and flare—were closely associated, but the physical relationships were difficult to establish because of the limited FOV and time cadence.[69,210] Initially, CMEs were thought of as the coronal response to the thermal energy released in flares,[211–214] implying that the flare onset should precede the initiation of CME acceleration. Attempts were made to establish the CME initiation time by extrapolating the observed CME trajectories to the solar surface below the occulter assuming constant speeds. Extrapolating downward to the lower heights where (unobserved) complicated dynamics prevail is problematic, and comparisons of extrapolated CME launch times and the observed onset times of the associated flares yielded inconsistent correlations.[74,210,215–218] Spatially, flares—the source of presumed pressure pulses—were often seen to occur in one or the other footpoint of the expanding loops, not centered in the cavities as might be expected if they resulted from flare-centered heating.[210] It was also suggested that the erupting prominence "drove" the CME from below, but EPs generally lag behind associated CMEs:[71] Figure 12 shows the SMM data of the CME-EP eruption combined with the ground-based Hα observation of the initial rise of the EP. It is clear that the apex of the prominence (solid symbols) has a slower speed than the CME LE. This was confirmed as a general property by the LASCO-EIT data. The new observations were instrumental in clarifying many of the persistently ambiguous associations between different eruptive phenomena, leading to a more unified view of eruptions.

The eruption of 2000 September 12 (Fig. 1) manifested a CME, EP, and flare. It was well-observed by multiple instruments and has been widely studied.[205–209] Figure 13(a) is an enlarged view of the filament *P* shown in Fig. 10(b).

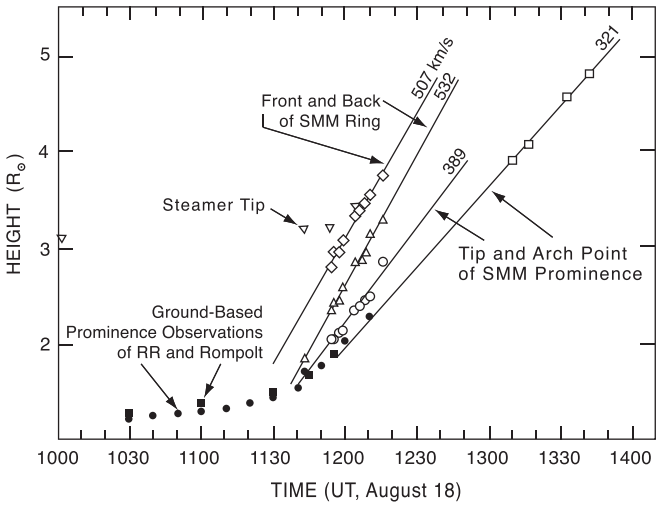

FIG. 12. Height-time profiles of several associated features observed in a CME event observed by SMM and a ground observatory. The distance between the CME LE and prominence LE increases with time. Figure 6 of Illing and Hundhausen[71] (redrawn).

This filament, which had been visible for a number of days, started to exhibit increased changes ("activation") at ~09:00 UT and significant motion at ~11:10 UT.[208] Figure 13(b) shows the prominence shortly after its liftoff. The apex (*P*, arrow) is assumed to be expanding in the solar radial direction, which implies a true speed of ~1600 km s^{-1}.[209] The prominence evidently retained its large-scale structural cohesion. There are thin strands connecting the two ends of the dark prominence to stationary bright features (*f*1 and *f*2) during the eruption. Such features are common and are interpreted as the prominence footpoints, suggesting that EPs remain magnetically connected to the Sun. Notice the two bright "ribbons," one on each side of the initial position of the filament (*R*, dashed arrows). Such a brightening is referred to as a *two-ribbon flare* and appears in Hα and EUV after the onset of eruption.

After leaving the EIT FOV of radius ~$1.3R_\odot$, the prominence was observed by the LASCO C2 and C3 coronagraphs, with Sun-centered circular FOVs of radius $2R_\odot$–$6R_\odot$ and $3.7R_\odot$–$32R_\odot$, respectively. Figure 13(c) shows a C2 image (southern half). Here, the circular disk is the C2 occulter, and the white circle marks the solar limb. The faint concentric bands around the occulter are an artifact. In this image, which shows the LOS-integrated Thomson-scattered white light from the photosphere, the eruptive prominence appears as a bright (dense) feature (*P*), expanding behind a much larger well-organized density structure, i.e., the CME LE (arrow). The evident large-scale coherence suggests magnetic organization. A nearly circular cavity is visible on the right, reminiscent of the three-part morphology (Fig. 5).[71] The CME-prominence structure is consistent with being a 2-D projection of a 3-D magnetic flux rope viewed from the side (Fig. 22; see Sec. III D), a concept distinct from either the dome or thin planar loop of the SMM era (Fig. 6).[69] These images show that the three-part feature is a small part of the larger CME structure.

Figure 13(d) is a C3 image (southern half) of the CME. The white circle marks the Sun, and the black disk is the C3

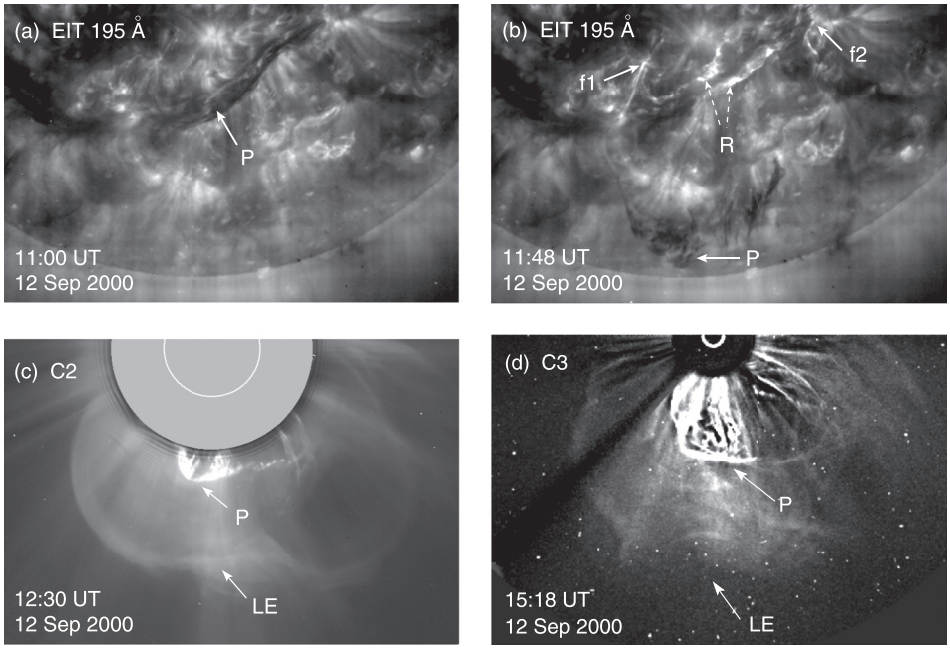

FIG. 13. EIT/SOHO (195 Å) images of the Sun (southern hemisphere) on 12 September 2000. (a) EIT image at 11:00 UT. The large filament (arrow *P*) has just started to show motion. (b) EIT image at 11:48 UT. The apex or the LE has moved significantly (*P*). Dashed arrows *R* point to two ribbons of the flare. (c) C2/SOHO image at 12:30 UT. The CME exhibits the three-part morphology[71] (bright rim, cavity, and prominence core on the right), which is a 2-D projection of the minor cross-section. The actual CME is much larger. (d) C3/SOHO image at 15:18 UT. The CME LE has expanded to approximately $22R_\odot$ (projected), corresponding to $42R_\odot$ true distance from Sun center. C2 and C3 images are constructed with the background corona subtracted from C2 and C3.

occulter (radius 3.7 $R_\odot$). The dark feature on the left is the shadow of the pylon supporting the occulter. The apex *P* of the EP and the LE of the CME are noted. The EP expanded slower than the CME LE, as in the case shown in Fig. 12. The three-part feature to the right is discernible in the same relative position as in Fig. 13(c). Evidently, the CME maintained its large-scale flux-rope structure.

Following the onset of the eruption, EIT recorded the formation and evolution of an arcade of thin bright loops. Figure 14 shows the arcade at 15:48 UT. This is the EUV counterpart of the X-ray arcade in Fig. 1 (5 min earlier). Comparing Figs. 9(b) and 10(b) to Figs. 13(b) and 14 we see that the two rows of footpoints of the arcade loops are on either side of the PIL. The two-ribbon flare observed in Hα closely coincides with the two-ribbon brightening in EUV [Fig. 2(c) of Ref. 208).

Regarding the CME-flare temporal relationship, GOES SXR and LASCO data including those from the innermost C1 coronagraph—a narrow passband Fabry-Perot interferometer imager observing from 1.1 $R_\odot$ to 3 $R_\odot$—showed that the acceleration phase of a number of CMEs, including the above 2000 September 12 event, coincided with the rise phase of the associated flare SXR emission,[219–222] This is consistent with the result of an earlier comparison of filament height-time data in Hα and impulsive hard X-ray (HXR) intensity curves.[223]

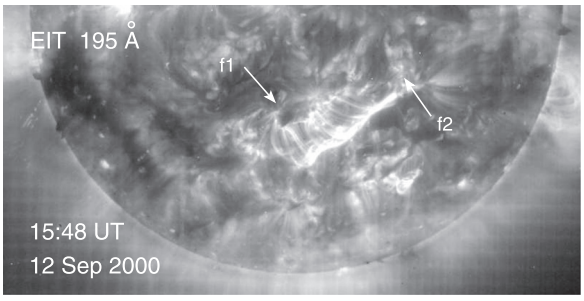

FIG. 14. Arcade of bright loops observed in EUV by EIT (195 Å), at 15:00 UT, 12 September 2000. The EUV arcade is co-located with the X-ray arcade shown in Fig. 1. The loops are similar in appearance to those seen in the TRACE image (Fig. 11) resolved at a finer resolution and viewed near the limb. The footpoints of the arcade loops correspond to the two-ribbon flare in Hα (Fig. 10) and EUV (Fig. 13).

Note that CMEs represent relatively minor perturbations of the corona: C2 and C3 images are constructed by taking the ratio of an image to the time-averaged background corona. This "subtracts" the non-erupting corona, enhancing the contribution from Thomson-scattering off free-electrons (K-corona) relative to the dusty plasma component (F-corona). For the SMM images, filters and polarizers were used to suppress the F-corona contributions.

III. PHYSICS OF CORONAL MASS EJECTIONS

The LASCO-STEREO era observations established a unified phenomenological understanding of the structure and dynamics of CMEs, EPs, flares, and MCs in the 1 AU region, providing new challenges to theoretical and numerical models. In particular, the CME dynamics observed over the 1 AU region impose stringent constraints on any models of CME driving mechanisms. It is generally assumed that the Lorentz force drives CMEs, but the actual forces acting on CMEs has been unclear until recently. The most important model element is the magnetic geometry of CMEs because the Lorentz force depends on the structure of currents and magnetic fields. Yet, these quantities cannot be measured. CME acceleration, however, is directly measurable and can constrain the driving force and therefore the model magnetic structure. Observed *dynamics* in the LASCO FOV and calculated flux-rope expansion were both essential in establishing the flux-rope CME concept. In this section, the physics of CMEs will be examined. The key observables are (1) CME/EP position-time data from which the *net* force per unit mass—acceleration—is determined, (2) temporal profiles of CME acceleration and flare SXR emissions, constraining the

relationship between the forces on CMEs and electric fields that may accelerate particles, and (3) *in situ* magnetic field and plasma properties of evolved CME ejecta at, say, 1 AU, which test the relationships between the plasma dynamics and magnetic field embodied in model equations.

A. Magnetic arcades: "Standard model"

Based on the consensus view shown in Fig. 6(a), various "cone models" of CMEs were proposed, bearing such names as "ice-cream cone"[81] and "light bulb."[224] These models are descriptive with no physical magnetic field ascribed to them, although they are still used to interpret 2-D images of CMEs propagating to 1 AU.[225–227] In the cone geometry, however, magnetic fields would have singularities,[228] and applied to observed density features of CMEs, cone models are problematic.[229] A non-singular magnetic configuration is that of the 2-D (linear or Sun-encircling) *arcade* of field "lines" anchored in the photosphere, schematically depicted in Fig. 15. A mathematical simplification is to treat the photosphere ($z = 0$) as an infinitely massive and infinitely conducting boundary of the half space, $z \geq 0$. This photospheric boundary condition decouples the coronal magnetic energy from the solar interior and has been standard in flare models.[230–249]

In its basic form, the field component B_n normal to the surface is specified at the photosphere ($z = 0$). The magnetic footpoints are assumed to move according to ideal MHD,

$$\mathbf{v}_\perp(\mathbf{x}, t) = c\frac{\mathbf{E} \times \mathbf{B}}{B^2}, \tag{5}$$

with specified $\mathbf{E}(\mathbf{x}, t)$ at $z = 0$. Conceptually, $\mathbf{v}_\perp$ is taken to be the convective fluid motion in the photosphere to which magnetic footpoints are "tied" via Eq. (5). A simple "shearing" motion of the footpoints ($\mathbf{v}_\perp$) is illustrated in Fig. 15, but converging flows may be required to produce eruptions.[250,251] Different models differ in the ways B_n and $\mathbf{v}_\perp$ are specified at $z = 0$. This is the so-called **B**-**v** paradigm.[243] The objective is to find a $B_n(x, y)$ and $\mathbf{v}_\perp(\mathbf{x}, t)$ that can cause an arcade to quasi-statically evolve from a stable configuration to an eruptive state. Mathematically, such a "catastrophic" transition from equilibrium to eruption may be characterized by bifurcations in quasi-static evolution.[230–232,237,239,252]

The concept of coronal energy build-up and storage can be traced to Carrington,[1] who noted that the sunspots being observed exhibited no unusual changes before, during, or after the white-light flare and that the brightening appeared to occur above the sunspot group. He concluded that the energy of the flare was stored in the corona. The form of stored energy was not specified. With the discovery that sunspots contained strong magnetic fields,[148] it was hypothesized that the energy of eruption was in the magnetic field; Giovanelli proposed the seminal idea that the merging or annihilation of oppositely directed magnetic field lines—now known as *magnetic reconnection*—could release energy stored in the sunspot magnetic field to power solar flares.[253,254] Merging of sunspots[255] and current loops[256] of opposite polarity that can annihilate the magnetic fields has been proposed to explain flare energy release. The magnetic energy, i.e., electric current, was taken to be built up by the differential rotation of the footpoints, a particular form of Eq. (5). The "collision" of two current loops was deemed to be a low-likelihood scenario. Interruption of the current in a single loop by the formation of double layers as a means to annihilate magnetic field has also been proposed.[257,258]

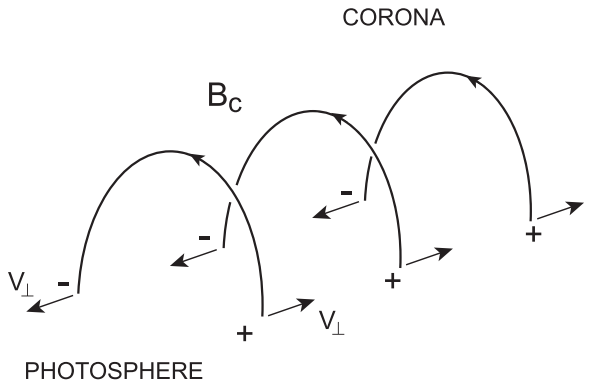

FIG. 15. Magnetic arcade. The photosphere is taken to be an infinitely massive and infinitely conducting surfaces where B_n and $V_\perp$ in the surface are specified. The magnetic field "line" footpoints are anchored in the photosphere.

The current prevailing paradigm is attributed to the concept of Carmichael,[259] expanded by Sturrock,[260] Hirayama,[261] and Kopp and Pneuman.[262] Much subsequent work has been done to refine this concept, which is often referred to as the Carmichael-Sturrock-Hirayama-Kopp-Pneuman (CSHKP) model[263] or the "standard model" of solar flares. In numerical simulations, the initial structure is typically specified as an arcade. Similar structures have been considered for prominence formation with the sheared arcades producing flux ropes via reconnection.[250,251,264,265] Within this framework, prominences are thought of as current sheets or flux ropes within arcades, supported by the repulsive Lorentz force from the image currents in the photosphere against gravity and the downward magnetic tension of the arcade field,[266–269] and if the tension is reduced or removed, prominences erupt upward because of this repulsive force.[252,270,271]

Figure 16 shows a qualitative comparison of the CSHKP concept with observation:[272] panel (a) is a *Yohkoh* image of a flare in SXR, compared with panel (b), a pictorial interpretation based on the CSHKP concept. Figure 16(c) shows another version,[273] which is a composite of selected features from various CSHKP models and interpretations of images and spectroscopic data. The arcade footpoints marked "flare ribbon" in the lower panel would correspond to the EUV ribbons R in Fig. 13(b) or the footpoints of the arcade field "lines" in Fig. 14 (see Fig. 15). The assumed magnetic field as well as the actual conditions of and implied mechanisms for the features in Fig. 16(c) (e.g., Petschek and termination shocks) are not directly observable. A broad discussion of particle acceleration by reconnection in the CSHKP picture is given in Chap. 12 of Ref. 42.

Figure 17[249] illustrates a 3-D resistive MHD simulation of the topological evolution from an initial current-free arcade to a current-carrying flux rope due to prescribed footpoint motion at $z = 0$. In this model, a current sheet is formed below the flux rope, and reconnection occurs according to

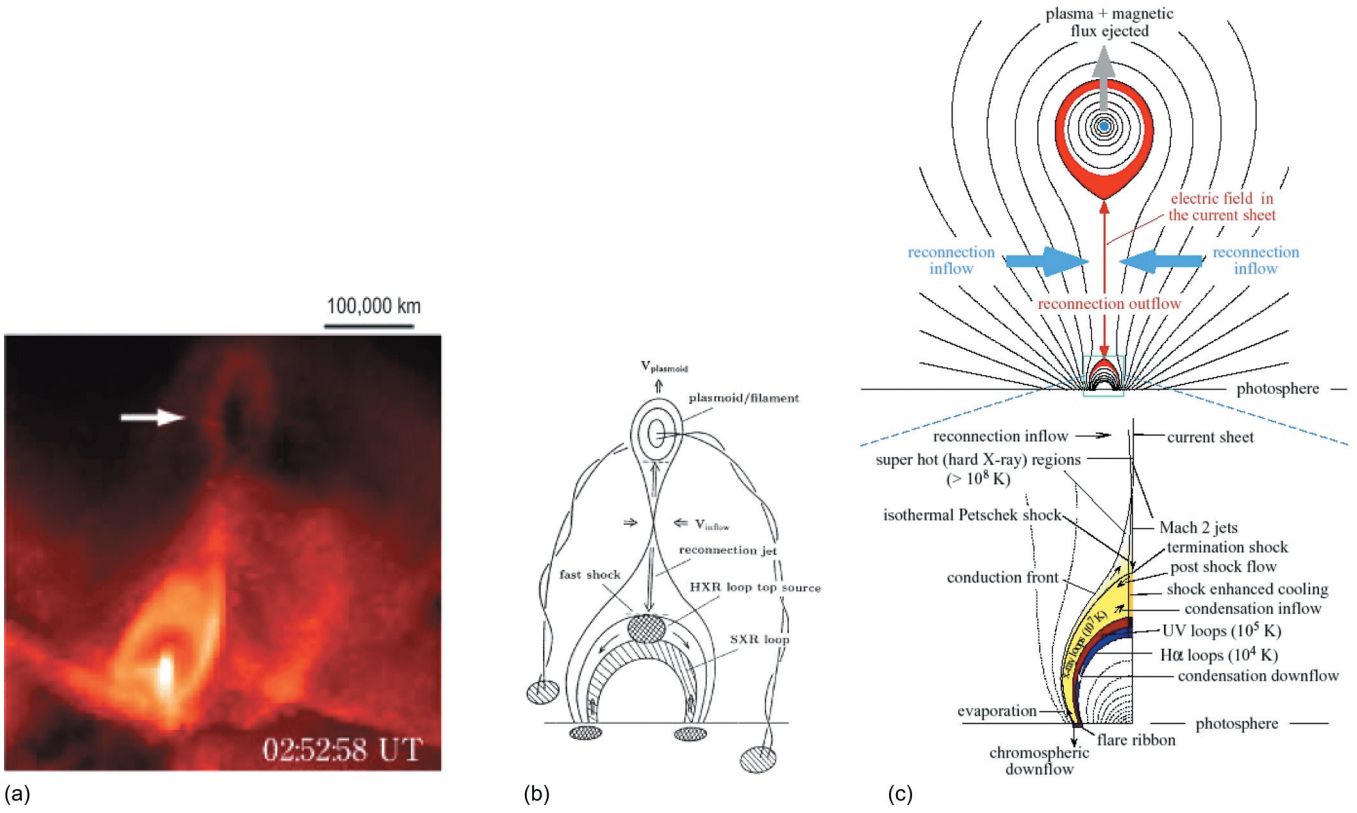

FIG. 16. Comparison of the Carmichael-Sturrock-Hirayama-Kopp-Pneuman (CSHKP) concept with observation. (a) *Yohkoh* SXT image of a flare. (b) Artist's conception of the CSHKP configuration for the event. From Ref. 272. (c) Schematic of CSHKP refined with numerous features motivated by observational and simulation interpretations. The features such as Petschek and termination shocks, condensation downflows are not directly observable. From Ref. 273.

specified resistivity, leading to the reduction of the overlying field and allowing the evolving flux rope to rise.

Figure 18[274] shows the evolution of a 2-D (Sun-encircling), initially current-free arcade with the morphology of a helmet streamer. The magnetic footpoints undergo specified "shearing" motion along the PIL, resulting in nonzero currents ($\nabla \times \mathbf{B} \neq 0$) and increased magnetic energy. The footpoint motion is generic, chosen for "convenience" to produce a sheared arcade field. Subsequently, an electric field E_{t0} is specified in the lower boundary in such a way as to produce a converging flow toward the PIL and reduce the arcade magnetic flux, where $E_{t0} \sim \partial B_z/\partial t$. This is used to mimic "flux cancellation" due to reconnection with surrounding field, likened to the cutting of overlying "tethers" holding the structure down.[275] The main energy release occurs between $t = 1380\tau_A$ and $t = 1420\tau_A$, an 8-h period, where $\tau_A = 12$ min is the Alfvén transit time. The synthetic coronagraph images (bottom) resemble the CSHKP schematic [Fig. 16(c)], and the three-part CME feature is evident. The above simulation was extended to 3-D where flux-rope formation, similar to Fig. 17, can be seen. In 3-D, the flux rope has footpoints connected to the Sun and can no longer be thought of as a detached plasmoid. Figure 4 of Ref. 274 shows their 3-D flux rope interpretation.

Figure 19[276] displays four time steps from a 2-D MHD simulation of the "breakout" model,[244] showing the normalized current density perpendicular to the figure. This model uses a quadrupolar magnetic configuration with three parallel arcades. This simulation imposes a shear flow on the footpoints of the center arcade parallel to the PIL (e.g., Fig. 15). This is shown as color-coded bands along the solar equator, with maximum $V_s = \pm 20$ km s^{-1}. This causes the center arcade to rise and reconnect with and "cut" the tethering magnetic field [panel (a)], converting the center arcade into a plasmoid, a detached flux rope, that expands away. This is followed by reconnection below the newly forming flux rope, which becomes detached from the Sun (in 2D). Following the "explosive eruption phase" due to "fast flare reconnection," the LE of this 2-D CME reaches 360 km s^{-1}, which would be a slow CME. Figure 19 shows the normalized current density as in Fig. 18. Figure 18 shows that the current density in that simulation is spatially correlated with the computed MHD density. The breakout CME shares a number of similarities with the model CME in Fig. 18. In both models, the initial rise of the magnetic structure is an ideal MHD process. The evolution of the driving force in these simulations depends on reconnection.

Eruptive scenarios involving multipolar structures were hypothesized in early models,[255,256] and later, MHD simulations were used to study plasmoid formation in 2-D (linear) multi-arcade structures.[233,234,241] Mikić *et al.*[233] found that shearing the footpoints of periodic double-arcades can cause an ideal MHD instability and lead to rapid formation of plasmoids via resistive reconnection. Using non-periodic configurations, Biskamp and Welter[234] showed that an isolated or laterally unrestricted double-arcade only expands quasi-statically under specified footpoint shearing and that it was necessary to have a minimum of three interacting arcades—a

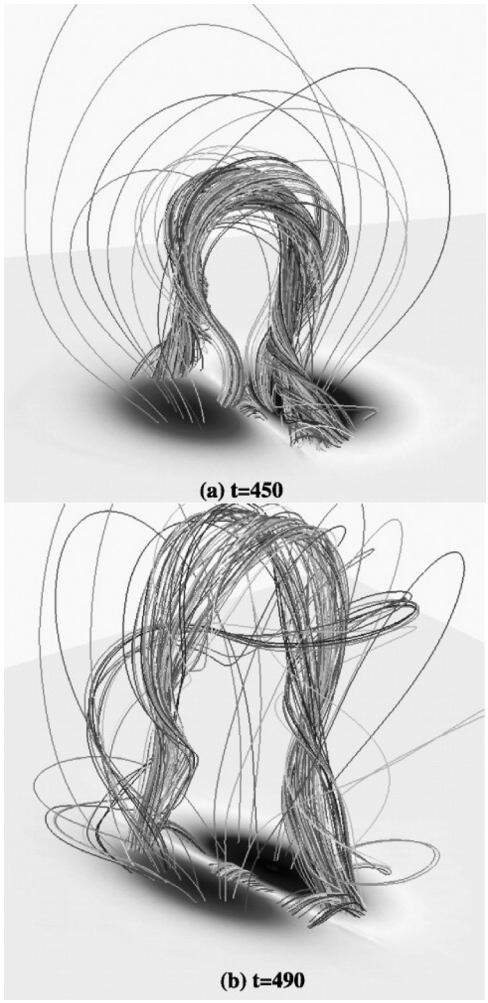

FIG. 17. A magnetic field-line representation of an expanding flux rope that has evolved from an initial current-free arcade, resulting from specified footpoint motion $\mathbf{V}(\mathbf{x})$ in the photosphere. Reproduced with permission from Amari *et al.*, Astrophys. J. **529**, L49 (2000). Copyright 2000 IOP Publishing.[249]

quadrupolar configuration—to confine the central arcade and produce eruptive behaviors. They concluded that the fast plasmoid formation in the periodic arcades[233] was caused by the artificial lateral confinement due to the symmetry and periodic boundary condition. Finn *et al.*[241] simulated nonsymmetric double arcades and obtained fast plasmoid formation when the footpoint shearing is alternated between the two neighboring arcades. They also showed that inserting unsheared flux between simulation ("hard") boundaries and the arcades, which effectively renders the numerical walls "softer," significantly reduced the instability producing the plasmoids. This suggests that if the arcade were in an open-boundary system, the instability could be absent. More recently, MacTaggard and Hood[277] carried out a 2.5-D simulation in which the initial "breakout" configuration is established with the central arcade rising through the boundary between the two side arcades (flux ropes). This simulation produced no eruption in the corona. They attributed this difference to the fact that the side arcade footpoints in their simulation can react to the motion of the central arcade while in the breakout simulations,[276,278] the shearing motion is restricted to the central arcade footpoints (Fig. 19).

These works[234,241,277] identified a number of hidden constraints due to symmetry and boundary conditions that can qualitatively alter the arcade stability and dynamics. In nonsymmetric 3-D systems, the greater degree of freedom allows energy to be distributed in less constrained and therefore more stable ways. Even in symmetric 2-D geometry, an arcade whose footpoints undergo infinite shearing does not tend to a configuration in which all the current is in the current sheet.[237] This contradicts an influential conjecture by Aly.[279,280] In this limit, the current density vanishes everywhere except at the current sheet,[279] but the current of the sheet becomes a vanishingly small fraction of the total current.

Although the specific magnetic field structures may be different, the basic process described by CSHKP models such as those shown above is the same—quasi-statically build up and confine magnetic energy in the corona and then "cut" the tethering field by reconnection to release "plasmoids." In all simulations to date, including those with adaptive mesh refinement, reconnection is due to numerical diffusion or prescribed resistivity. One fundamental gap between such simulations and reality is that the known physical length scale c/ω_{pi} and timescale ω_{ci}^{-1} of reconnection in both fluid and particle models including the Hall physics[281] differ by many orders of magnitude from the scales manifested in observed eruptions, $\sim 10^5$ km and tens of minutes. Here, $\omega_{pi} \equiv (4\pi n_i e^2/m_i)^{1/2}$ and $\omega_{ci} \equiv eB/m_i c$ are the ion plasma and Larmor frequencies, respectively, and c/ω_{pi} is the ion inertial length at which ion motion decouples from magnetized electrons. In the corona, $c/\omega_{pi} \sim$ 1–10 m and $\omega_{ci}^{-1} \sim 10^{-6}$ s (Table I), to be contrasted with the length scale of 10^4–10^5 km and timescale of tens of minutes in eruptive processes in the corona. Dynamics on the much smaller electron inertial length may also be important.[282] There is as yet no demonstrated sub-grid physical dissipation required of reconnection. The above model results are 2-D, and in 3-D, reconnection dynamics are expected to be significantly different. It is noted that the ion Larmor radius ρ_L is orders of magnitude smaller than the collisional mean-free path in the corona (Table I). Reconnecting current sheets are likely to be kinetic in nature.

Simulation models based on the CSHKP concept study the eruption of arcades *caused* by specified footpoint motions. Simulations have also shown that such motion can *result* in response to the emergence of erupting flux ropes through the photosphere, representing transport of magnetic energy.[297] Numerically, the simulation boundary is effectively placed at the base of the corona, and high footpoint speeds are imposed [$V_s = 9$ km s^{-1},[246] 65 km s^{-1},[278] and 20 km s^{-1} (Ref. 276)] Because photospheric and chromospheric features nearly corotate, these speeds would map down to the photosphere. The true quasi-static limit and catastrophic transition to eruption in such CSHKP models are not known, but the simulations do show separation of timescales between the boundary conditions and simulated coronal dynamics. Photospheric features do not exhibit motion faster than $\sim$1–2 km s^{-1}.[283,284]

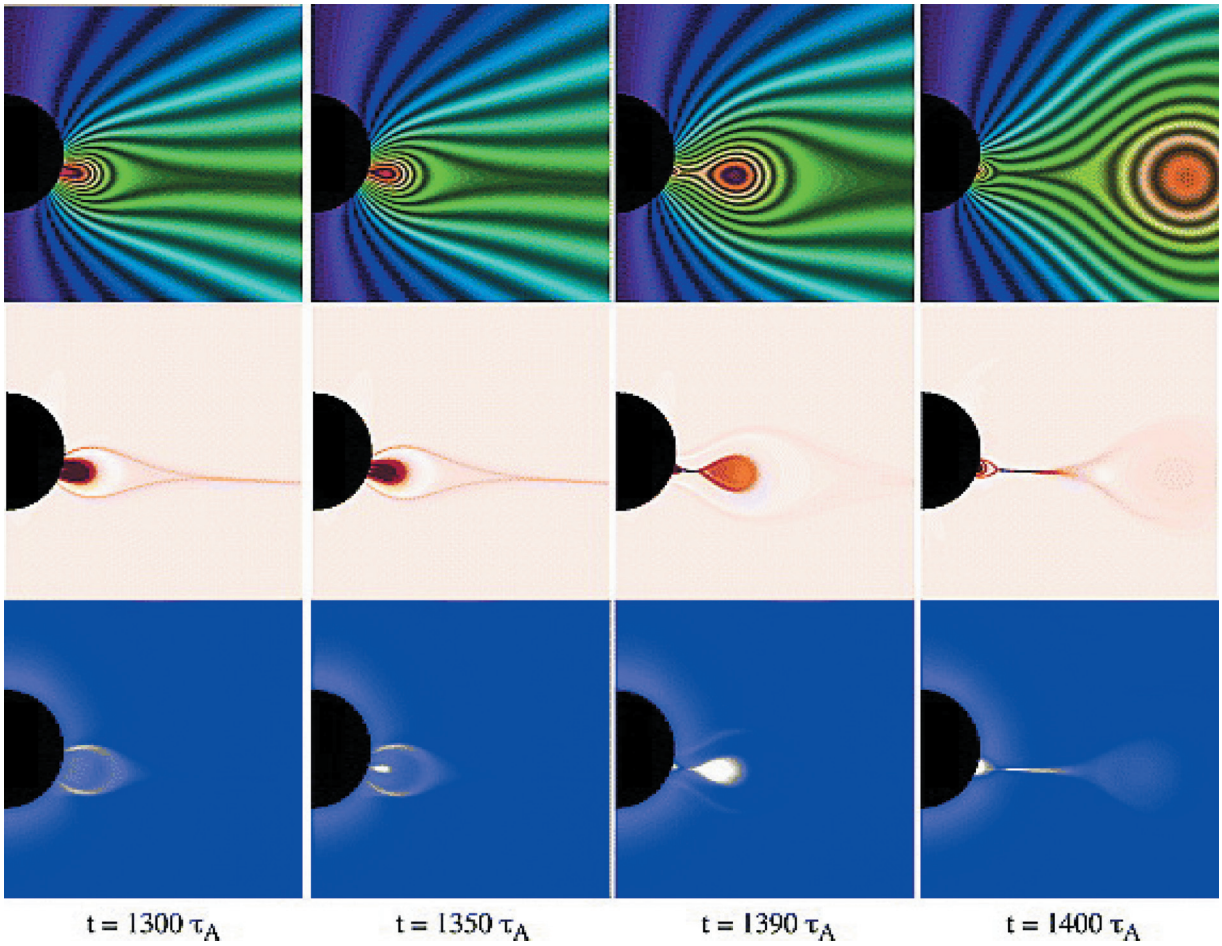

FIG. 18. Structural evolution of a 2-D sheared arcade, evolving into a plasmoid (flux rope). The stripes (top) show projected field lines. The current density out of the plane of the figure (middle) is shown. The initial arcade has maximum current in the core of a helmet streamer like structure, developing a current "sheet" high in the corona. The synthetic polarization brightness images (bottom) are based on the MHD density distribution. Time is shown in units of the Alfvén transit time across $1R_\odot - \tau_A = 12$ min for this simulation. A uniform resistivity is specified. The Lundquist number on the scale of $R_\odot$ is 2×10^5. Reproduced with permission from Linker *et al.*, Phys. Plasmas **10**, 1971 (2003). Copyright 2003 AIP Publishing.[274]

Based on the quadrupolar configuration required by the breakout model, Antiochos *et al.*[244] proposed that CMEs associated with high-latitude *polar crown prominence* eruptions, which originate from bipolar source regions, should not be classified as CMEs. They argued that such CMEs tend to be "slow," comparable to the slow SW speeds of ∼400 km s^{-1}. The typical source, however, is a bipolar region with a prominence aligned with the PIL [e.g., *A* in Fig. 9(b)], and polar crown prominence CMEs may be "fast" (much faster than, say, 600 km s^{-1}, the fast SW speed).[285,286] The average speed of CMEs is 400 km s^{-1}.[64]

Physically, the most difficult feature of the CSHKP picture to validate is the reconnection region, indicated by "reconnection inflow" and "reconnection outflow" in Fig. 16: the scale of reconnection c/ω_{pi} cannot be resolved by observation, and the relationship between the plasma processes on this scale and the macro-scales of eruption has not been established. Recent studies examining specific signatures of coronal reconnection in high-resolution data from SDO and *Hinode*, for example, timing and locations of flare heating and associated motions of emission sources,[287,288] concluded that the data were consistent with the primary flare heating taking place in the inflows and outflows outside the inferred reconnection sites but that no specific mechanisms for the observed heating could be demonstrated.

B. Photospheric plasma motion

The standard photospheric boundary condition used in the CSHKP models assumes infinite conductivity ($\sigma = \infty$) and mass density ($\rho = \infty$) and that the magnetic footpoints can be specified via Eq. (5), typically given by a continuous function $\mathbf{E}(\mathbf{x}, t)$. This boundary condition does not specify the vertical fluid motion v_z or $v_\parallel = \mathbf{v} \cdot \mathbf{B}/|\mathbf{B}|$ at $z = 0$. Photospheric plasma (fluid) elements generally move in 3-D, so that the apparent motion of an observed feature such as the footpoint of a magnetic element may not correspond to the actual fluid velocity $\mathbf{v}$. Macroscopically, a plasma element remains in the photosphere for less than ∼1000 km and 10 min, the typical size and lifetime of granules, respectively. In addition, magnetic features appear and disappear on a time scale much shorter than the quasi-static shearing time scales of days and weeks.[165] Thus, the notion that a fluid element or magnetic feature can be given a continuous or non-singular velocity field in the photospheric surface beyond the granule time and length scales is generally

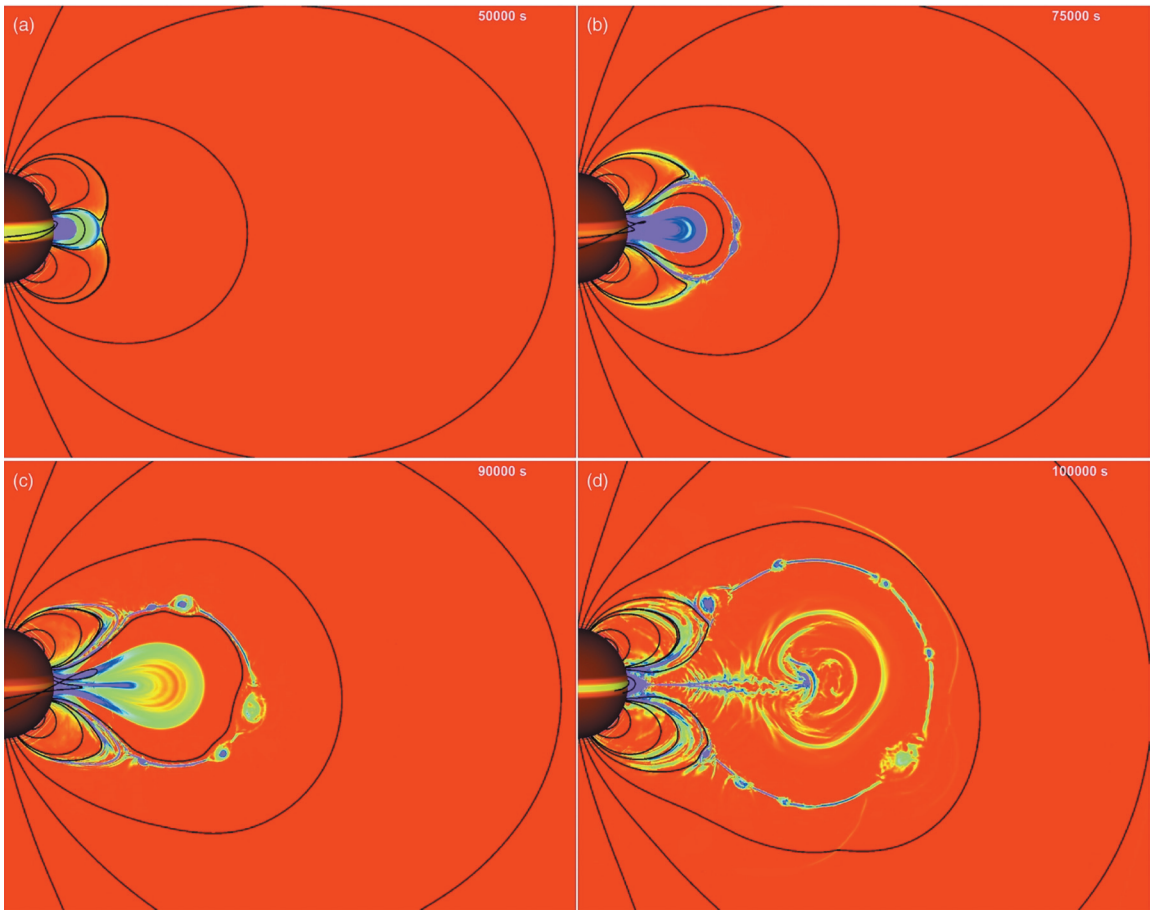

FIG. 19. "Breakout" model simulation in 2.5-D using adaptive-mesh refinement. Black curves: field lines. The yellow band along the solar equator shows specified photospheric shear. The images show normalized coronal current. (a) Onset of the "breakout reconnection" at the apex of the central arcade. (b) "Breakout" of the central arcade. (c) and (d) Subsequent evolution. Reconnection is due to numerical diffusion. Reproduced with permission from Karpen *et al.*, Astrophys. J. **760**, 81 (2012). Copyright 2012 IOP Publishing.[276]

invalid. The photospheric boundary condition has also been interpreted to mean that B_z is constant,[289] which is used in some simulations (e.g., Ref. 291). Physically, infinite conductivity only requires constancy of magnetic flux enclosed by a closed contour moving with plasma elements. The field strength may change as the contour changes. If resistive, footpoints may be dissipated away. Thus, care must be exercised in formulating simulation boundary conditions.

Magnetized photospheric plasmas move in response to energy rising from the convection zone at the local magnetosonic speed V_M:[290] neglecting gravity and radiation, we have the scaling

$$\rho\frac{d\mathbf{v}}{dt}=\frac{1}{c}\mathbf{J}\times\mathbf{B}-\nabla p\sim\rho\frac{\left(V_A^2+C_s^2\right)}{a}=\rho\frac{V_M}{\tau_M}, \qquad (6)$$

where $V_A=B^2/(4\pi\rho)$ and C_s are the characteristic Alfvén and sound speeds, $V_M\equiv\left(V_A^2+C_s^2\right)^{1/2}$, $\tau_M\equiv a/V_M$, and a is the spatial scale. Here, V_A and C_s are based on deviations of macroscopic magnetic field and pressure from equilibrium. The basic scaling of MHD processes in the solar atmosphere takes on the form $d\tilde{v}/d\tilde{t}\sim 1$, where $\tilde{v}\equiv v/V_M$ and $\tilde{t}\equiv t/\tau_M$ are the characteristic local velocity and time scales of changes.

Equation (6) reflects the fact that the basic MHD equations are scale invariant. Physically, if a quantity of energy rises through the photosphere, the plasma medium will respond at V_{Ms}. If this energy reaches the corona, the coronal plasma will respond at V_{Mc} according to the local coronal parameters. For MHD processes, $V_{Mc}\gg V_{Ms}$. For the canonical magnetized coronal and photospheric plasma parameters, $V_{Mc}\sim 10^3$ km s^{-1} and $V_{Ms}\sim 1$ km s^{-1}. On the scale of observed magnetic elements (<100 km, Fig. 8), $\tau_{Ms}\sim$ 100–200 s.

The rationale for ideal-MHD line tying in the weakly ionized photosphere is that the resistive diffusion time across dimensions of 10^5 km (e.g., active regions) is much longer than the eruptive timescale. Magnetic and electric current elements in the photosphere, however, are generally highly filamented (<100 km, Fig. 8), and the dissipative timescale on that scale would be shorter by a factor of 10^{-6}, possibly contributing to the disappearance of small magnetic features in tens of minutes.[165] Ideal MHD is difficult to justify.

C. MHD simulations of flux ropes

In contrast to the above simulations using arcades as the initial structure driven by quasi-static footpoint shearing, Wu *et al.*[37] earlier carried out the first 2.5-D MHD simulation of

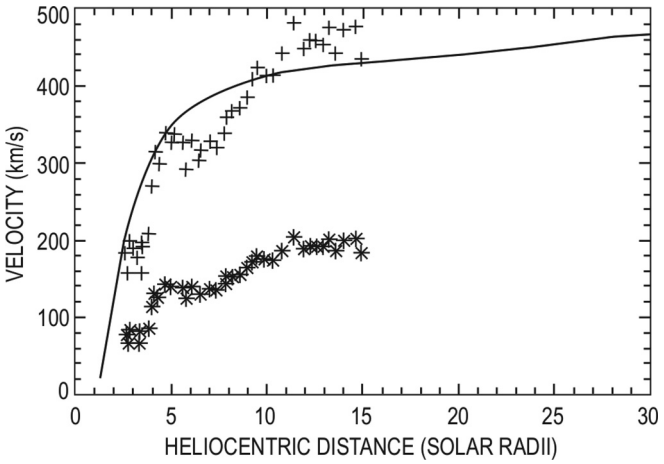

FIG. 20. Measured CME LE velocity versus height in the plane of the sky (asterisks), corrected for projection (pluses). The CME LE could be tracked to about $15R_{\odot}$. The solid curve is the computed CME LE speed versus height. Reproduced with permission from Wu *et al.*, J. Geophys. Res. **104**, 14 789 (1999). Copyright 1999 Wiley.[37]

a flux rope expanding away from the Sun and compared the resulting flux rope at 1 AU with an observed MC. This was associated with a CME observed by C2/LASCO on 6 January 1997. The MC—the presumed CME ejecta—was detected four days later by the WIND spacecraft at 1 AU. The C2 and EIT images indicated that the CME trajectory had a significant southward component. The Sun-encircling flux rope, initially in equilibrium with a model helmet streamer, was driven by the injection of poloidal flux. They calculated the expansion of the model flux rope to 1 AU and compared the results with the observed CME expansion and the magnetic structure of the ejecta detected by WIND. Figure 20 shows the simulated CME expansion velocity versus position from Sun center (curve) and the observed data (asterisks) corrected for projection (pluses). The simulated flux rope is qualitatively consistent with the LASCO CME data in expansion speed and with the observed MC in structure at 1 AU. The LASCO data, however, does not show the initial acceleration for comparison, and the 2.5-D model does not have a physical initiation mechanism.

Similarly, Manchester *et al.*[199,200] simulated a 3-D flux rope inserted into a model corona. The flux rope, initially out of equilibrium, has footpoints anchored in the photosphere and expands to 1 AU, yielding flux-rope properties consistent with those of observed MCs at 1 AU. The simulated flux rope also shows considerable deformation. The time evolution of the model structure is shown in Fig. 21. White curves indicate the magnetic streamlines and the color scale gives the fluid plasma speed, ranging from 300 km s^{-1} (blue) to 780 km s^{-1} (red). All the magnetic energy of the eruption is in the initial nonequilibrium flux rope, and the initial acceleration in the inner corona that leads to an MC-like solution at 1 AU is faster and more peaked near the Sun than is observed for CMEs (Fig. 11 of Ref. 199).

The simulations proved in principle that a CME-like flux rope can evolve to an MC-like structure, consistent with the predicted CME-to-MC connection.[86,320] This connection was more directly established for the first time by STEREO observation.[33]

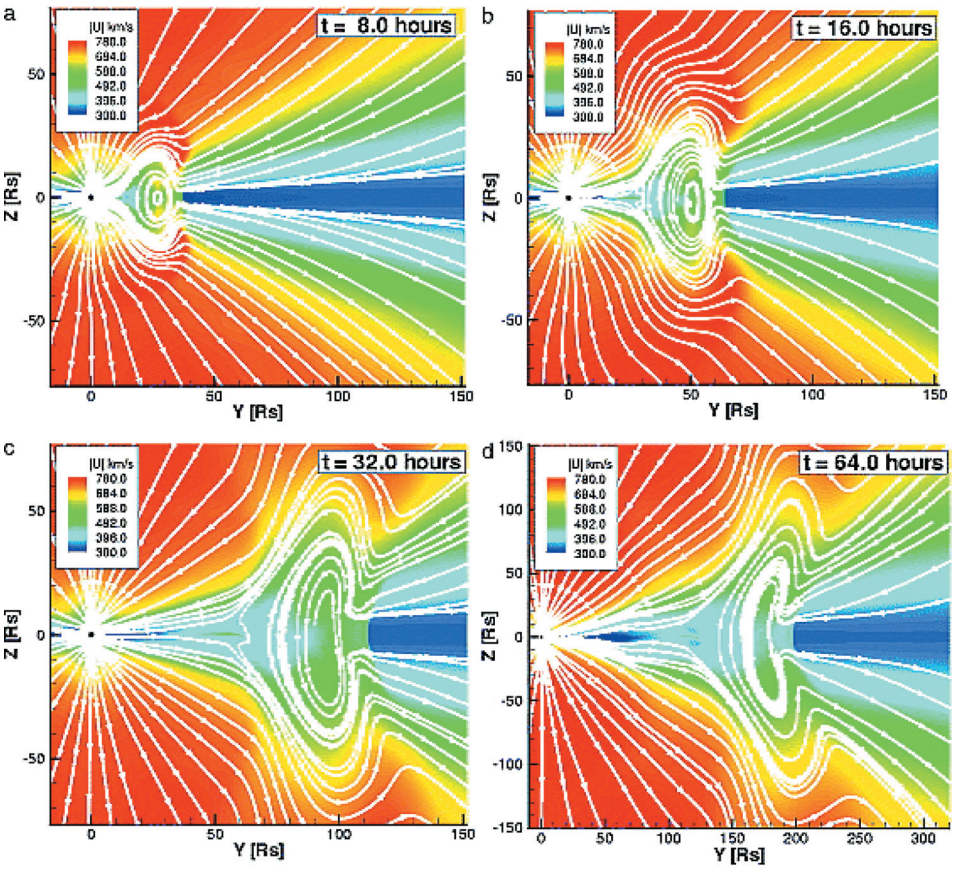

FIG. 21. Time evolution of a flux-rope CME at (a) t = 8 h, (b) t = 16 h, (c) t = 32 h, and (d) t = 64 h. Solid white lines display magnetic streamlines and the color scale shows the MHD fluid speed. Reproduced with permission from Manchester *et al.*, J. Geophys. Res. **109**, A02107 (2004). Copyright 2004 Wiley.[200]

D. Magnetic flux rope hypothesis

Instead of arcades, one may hypothesize that pre-eruption structures are equilibrium magnetic flux ropes with their footpoints anchored in the photosphere.[85,291,293,294] Eruption of flux ropes upon emergence without first establishing equilibrium has also been simulated.[295–297] Some models start with nonequilibrium or unstable flux ropes in the corona.[199,200,298] In general, however, observation suggests that pre-eruption structures exist in quasi-equilibrium [e.g., Fig. 13(a)].

Figure 22 illustrates a solar magnetic *flux rope*.[86] It is a self-organized toroidal pinch made up of a current channel and its self-magnetic field. The current density has toroidal (locally axial, J_t) and poloidal (locally azimuthal, J_p) components, related to B_p and B_t by $\mathbf{J} = (c/4\pi)\nabla \times \mathbf{B}$. The flux rope is anchored in the photosphere with its current assumed to be closed in or below the photosphere (dashed curves), with the footpoints separated by distance S_f. The subsurface current structure cannot be observed, and none is specified. With no eruption, the entire structure is assumed to be in steady state, with dissipative losses balanced by the dynamo deep in the convection zone (indicated by "*D*"). The flux rope is in equilibrium with the ambient coronal pressure, p_c, overlying field B_c, and gravity. Here, B_c is due to an electric current separate from the flux-rope current. At any given point in space, the magnetic field is a linear superposition of the contributions from all sources and may be more complex than is depicted. The polarity of B_c in the photosphere is indicated by "+" and "−" signs and is drawn in such a way that the Lorentz force $I_t B_c$ is downward. In the photosphere, this configuration would be a bipolar region similar to region *A* in Fig. 9(b) (but opposite polarity). Topologically, the toroidal field B_t is normal to the surface, and the poloidal component is tangential to the surface. The actual poloidal field "lines," however, may be undular and go in and out of the high-β photosphere as depicted.

In the corona, the prominence material is partially ionized ($0.05 < \zeta < 1$). With $n_p \sim 10^{11}$ cm^{-3} and $T_p \sim 10^4$ K, the ion-neutral collision frequency is $\nu_{in} \sim 4.5 \times 10^2$ s^{-1}. If $B = 10$ G,[55,56] the ion Larmor radius is $\rho_L \approx 10$ cm and $\beta \simeq 7 \times 10^{-2}$. Thus, on the scale of 10^5 km and tens of minutes, the neutral hydrogen is coupled to the magnetic flux rope via the ionized plasma. The visible prominence is assumed to be organized by the relatively strong magnetic field in the low-β core of the flux rope.[86] Figure 23 schematically depicts the internal structure of a flux rope with the prominence material providing an observable proxy for the trailing edge (TE) of the current channel, as indicated by the short vertical lines (*P*). A similar concept is depicted in Fig. 5 of Ref. 300.

The above configuration is of the so-called "inverse" polarity type,[51,266] in which the polarity of the magnetic field threading the prominence is opposite to that of the photospheric field (+ to − in Fig. 22). This is distinct from the so-called "normal" polarity configuration,[268] which may be

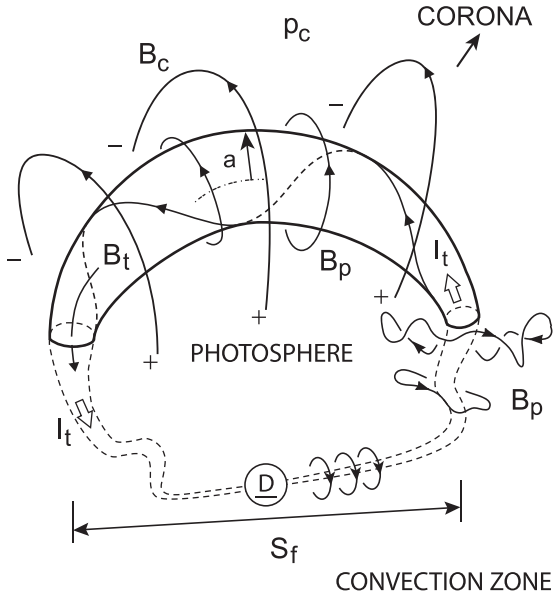

FIG. 22. Solar flux rope in the corona with pressure p_c and overlying coronal magnetic field B_c perpendicular to the flux rope, consisting of a current channel of minor radius a and the self magnetic field (B_p, B_t). The toroidal (I_t) and poloidal (I_p) currents are indicated. Footpoints of B_c are indicated by +'s and −'s. The flux-rope footpoints are separated by distance S_f. The toroidal current I_t is closed in or below the photosphere, ultimately connected to the solar dynamo schematically indicated by "D." Subphotospheric current structure cannot be observed, and no specific structure is specified. In steady state, the dynamo balances dissipative energy losses. The set of three smooth poloidal field lines are newly "injected" into the flux rope by the dynamo. A 3-D version of Fig. 5 of Ref. 220.

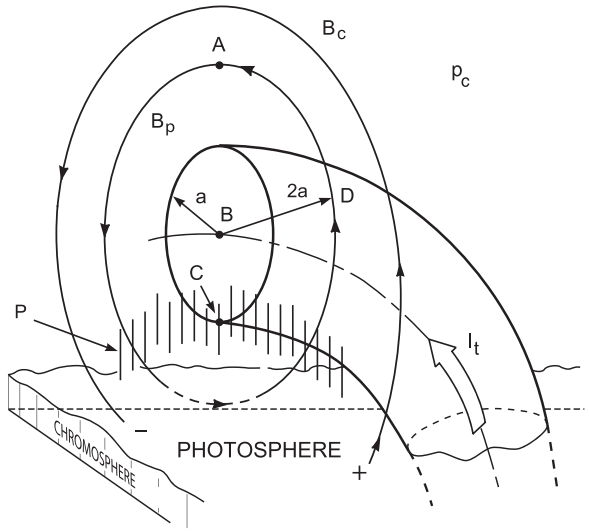

FIG. 23. Cut-out view of a model flux rope showing one leg through the chromosphere and photosphere (the bottom surface). The toroidal current (I_t), poloidal magnetic field (B_p), and overlying coronal field (B_c) are indicated, with "+" and "−" indicating the polarity of B_c or B_p in the photosphere (cf. Fig. 15). The current channel has minor radius a, apex is at point A, trailing edge of the current channel is C, and B is the centroid. The trailing edge of the flux rope is below C. B_p is the poloidal field due to I_t, and B_c is due to currents other than that of the flux rope. (The poloidal current I_p is not shown for simplicity.) $I_t, I_p, B_t = 0$ for $r > a$. Pressure is smoothly continuous at $r = a$, with p_c the asymptotic value. The flux-rope field is taken to extend to $D = 2a$. Part of the field line may be embedded in the chromosphere (dashed arc). Topologically, at the footpoints, the toroidal field ($B_t = const$) is vertical, but the poloidal component (B_p) is horizontal. Along the PIL, B_p is vertical. The short vertical line segments (*P*) indicate the prominence material. From Ref. 86.

visualized by loading the filament on the arcade top (Fig. 15) and creating a "dip" at the top of the field lines to prevent the filament from sliding off. Observationally, inverse-polarity prominences are far more numerous.[51] For good reviews of early models, see Refs. 51, 301, and 302 Note the remarkable resemblance between the CME in Fig. 13(c) and this model configuration. We will return to it later.

The initial flux rope has nonzero current satisfying $(1/c)\mathbf{J}\times\mathbf{B}-\nabla p-\rho\nabla\phi_g=0$, where ϕ_g is the gravitational potential and $\mathbf{B}$ includes B_c. The traditional adage, however, holds that current structures in the corona must start as "potential" magnetic field lines ($\nabla\times\mathbf{B}=0$) and that nonzero currents are generated by twisting the field-line footpoints. Under ideal MHD, such structures must maintain zero net current by generating return currents. Early loop models appealed to this notion[256] as do arcade models such as those discussed earlier (Sec. III A). Nevertheless, vector magnetograms of active regions show the presence of nonzero net electric currents in bipolar regions,[303–305] and there is morphological evidence that pre-formed flux ropes with nonzero net currents rise through the photosphere.[306–309] Theoretically, if poloidal flux is allowed to emerge into an existing flux rope, the toroidal current can increase with no need of any neutralizing return current. This is possible if the photosphere is finitely massive or conducting.

E. Flux-rope CMEs

The macroscopic MHD forces in this configuration[85,330] and application to CME/EP dynamics[86] have been theoretically treated. The key physics in this theory, now known as the erupting flux rope (EFR) theory of CMEs, is the major radial Lorentz hoop force.[299] Initially, the universal consensus was that CMEs were dome-like density shells instead of thin ("planar") loops [Fig. 6(a), Sec. I A), which led to a broad rejection of flux ropes as CMEs. The application of the hoop force to solar flux ropes[85,310] was also regarded as a "laboratory" technique inapplicable to solar structures. With the new LASCO observations, however, the consensus shifted to the flux rope geometry (Fig. 23),[87–89,93,291,295] and the hoop force is now incorporated into models of CMEs.[199,289,295,298,311,312] In this section, we examine the details of the 3-D magnetic topology underlying CMEs and EPs and the macroscopic forces acting on them.

1. Observed morphology

Figure 24(a) shows the image of the first CME to be identified as an expanding flux rope,[87] obtained by the LASCO C2 coronagraph on 13 April 1997 shortly after LASCO commenced routine observation in late 1996. The CME was observed to be erupting off the west limb (to the right; see Fig. 1) and slightly south of the ecliptic plane. A nearly circular rim A is evident, with the LE a, trailing edge (TE) c, upper rim d_1, and lower rim d_2 indicated. The centroid of A is denoted by b and is determined by the average of the coordinates of a, c, d_1, and d_2. Close examination shows that A contains concentric striations, with a concave

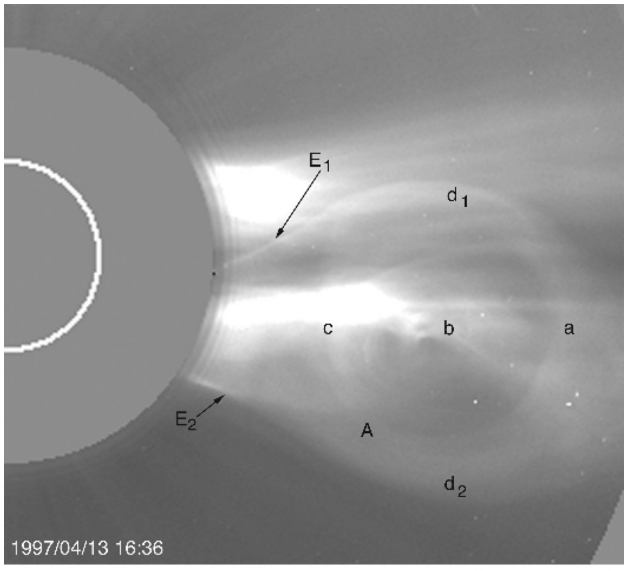

(a)

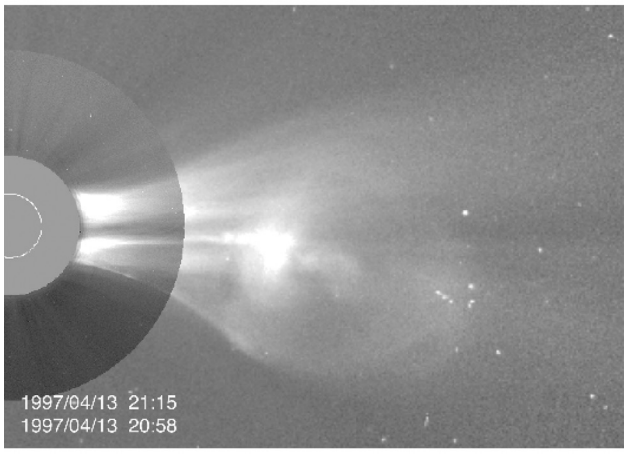

(b)

FIG. 24. CME observed on 13 April 1997. (a) C2 image of a three-part CME at 16:36 UT, 13 April 1997, exhibiting a bright rim, cavity, and a core. No C1 or C2 data exist prior to 16:00 UT. (b) C2-C3 composite of the CME, with the C2 image obtained at 21:15 UT and C3 image at 20:58 UT. The bright white dots in the C3 FOV are stars. From Ref. 87.

up feature at c. The circular rim encloses a relatively dark cavity and a bright core. There is a pair of relatively bright features E_1 and E_2 connected to the rim A. Figure 24(b) is a C2-C3 composite of the CME: the LE of the CME had reached $\sim 15\ R_\odot$ and the width $D=|\mathbf{d}_1-\mathbf{d}_2|$ had increased to $\sim 8\ R_\odot$. The bright concave up feature at c was still located at the TE of A, which remained nearly circular. It is evident that the CME maintained its structural integrity and by implication its magnetic topology. The CME structure remained identifiable until the LE reached $\sim 25\ R_\odot$ beyond which it was too faint to track accurately. Significantly, E_1 and E_2 remained continuous in the C2-C3 FOV and showed little change relative to the occulter for as long as they could be discerned.

Although this CME exhibited the prototypical three-part morphology [Fig. 5(c)], it was interpreted as an expanding *toroidal* flux rope as shown in Fig. 25(a): the Sun is viewed from the north and the flux-rope major axis lies in the

ecliptic plane. Here, "toroidal" means that the structure can be approximated as a segment of a torus. The circular rim *A* in Fig. 24(a) is interpreted as the projection of minor circumferences, a few of which are illustrated. The striations can result if any nonuniformity from one circumference to the next is present. Figure 25(b) shows a synthetic coronagraph image of a model 3-D flux rope with a hollow density distribution peaked near the outer edge, $r = 2a$ (Fig. 23). Its footpoints are located slightly south of the equator. The assumed density distribution is convolved with the Thomson scattering function[72] and integrated along lines radiating from an observer at 1 AU $\simeq 215\ R_\odot$ [indicated by *OBS* in Fig. 25(a)]. The method is described in the Appendix in Ref. 95. The synthetic image exhibits all the salient features of the CME in the C2 data, showing that the observed CME is consistent with being a magnetic flux rope. The prominence has been omitted for simplicity, but one located in the flux rope [short line segments, Fig. 25(a)] would appear as a bright feature in the cavity extending toward the Sun [Fig. 24(a)]. In the earlier planar loop concept,[75,76] the circular rim *A* would be the CME loop, orthogonal to the new flux rope configuration.

While the specified hollow density distribution in Fig. 25(b) is *ad hoc*, theoretical calculations show that flux ropes naturally develop density peaks near the edge at $r \simeq 2a$.[294,313] The 2.5-D MHD simulation shown in Fig. 18 (bottom panels) also shows similar features.

The presence and persistence of the bright features E_1 and E_2 is significant. Similar long-lasting bright rays/streamers following CME eruptions were also observed in the more limited SMM FOV,[71] but the structural relationship to the expanding CME loop could not be ascertained. The large-FOV LASCO images show that E_1 and E_2 correspond to the outer edges of the legs projected on to the plane of the sky. This provides evidence that expanding CMEs remain connected to the Sun, contrary to the notion that CMEs are plasmoids detached from the Sun. Certain observed bright rays and concave upward Y-shaped features, for example, those at *c* in Fig. 24(a) and its C3 counterpart in Fig. 24(b), have been interpreted as current sheets and disconnection.[314–316] Numerical simulations in 2D have also shown field reversal below flux ropes[248,274,276] (e.g., Figs. 18 and 19). Figure 26 shows a synthetic image of the same 3-D flux rope as in Fig. 25(b) except that the two footpoints are placed such that the line connecting them is at 25° with the solar equator. The figure shows a Y-shaped bright feature that results from the overlap of the projections of the two legs and TE of the apex (concave up). In fact, these legs are more than a solar radius apart with no current sheets. This figure provides a specific 3-D magnetic topology and an alternative to the current-sheet interpretation of Y-shaped features. Recall that the corona is optically thin, and brightness in coronagraph images is proportional to the LOS-integrated column density of free electrons.

Figure 27 shows another CME, this one having the morphology of a hollow flux rope viewed from the side (LE *a* and TE *b*). The bright feature at the TE is the prominence,

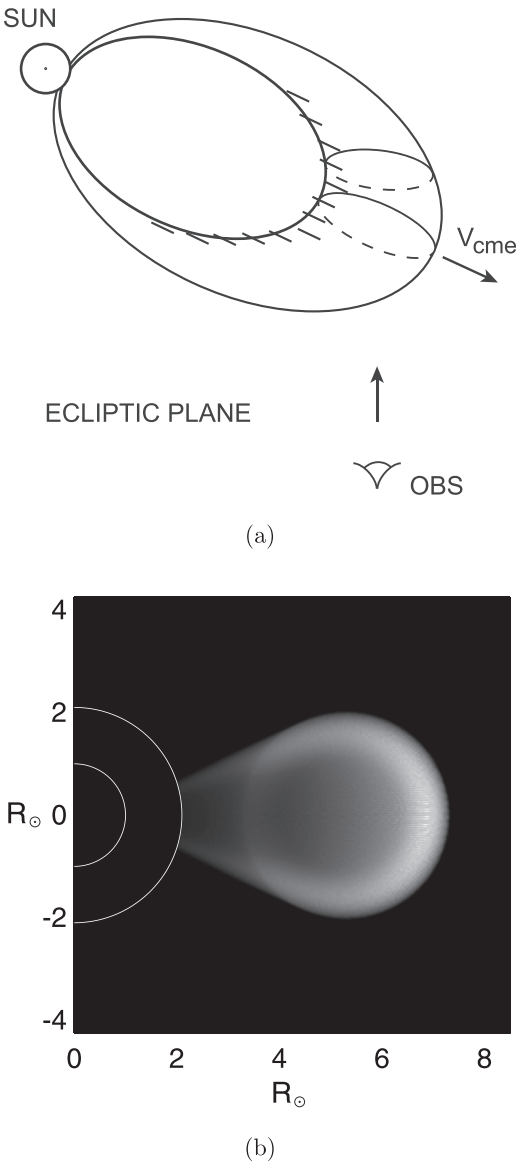

FIG. 25. (a) Interpretation of the CME of 1997 April 13, viewed from the solar north. The outermost magnetic surface of a flux rope lying in the ecliptic plane is indicated by two minor radial circumferences. The velocity of the apex (V_{cme}) and the line of sight from the observer are indicated. The short line segments represent the prominence, the counterpart of *P* in Fig. 22. (b) Synthetic C2 coronagraph image: both footpoints are placed on the solar equator. A quantitative realization of the schematic given in (a) using Thomson scattering function. The prominence is not included.

with the same spatial relationship to the CME flux rope as the event in Fig. 13. Figure 28 is a high-resolution view of an eruptive prominence, whose "legs" remained virtually stationary during the eruption. This image was obtained by EIT using the He II 304 Å emission line, and the intensity is proportional to n^2 integrated along the LOS. The emission indicates a temperature of 5×10^4 to 6×10^4 K and does not show the hot corona or the associated CME. In interpreting this image, keep in mind that an observed prominence is only a small part of a flux rope [Figs. 5(c), 13(c), 13(d), and 27]. Prominences are sometimes modeled as "kinked" flux ropes,[317] but a prominence may simply occupy a helical "bundle" of field lines in an un-kinked magnetic flux rope (e.g., Figs. 13 and 28).

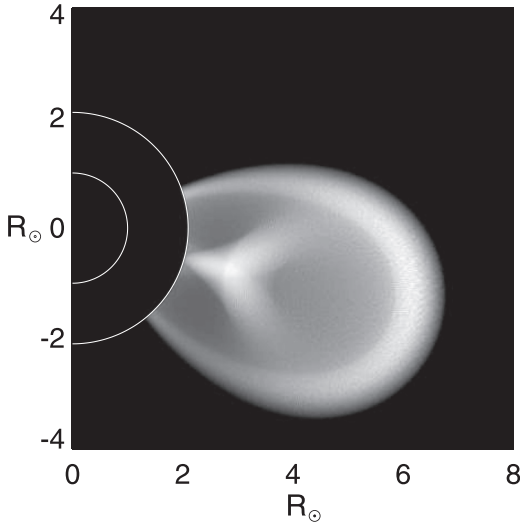

FIG. 26. Synthetic coronagraph image of a flux rope oriented at angle with respect to the solar equator. The footpoints are placed so that the line segment connecting them is at 25° to the equator. Otherwise, the flux rope is identical to that in Fig. 25(b). The cavity contains a Y-shaped density feature resulting from the overlap of flux-rope legs that are separated by $1/2$–$1R_\odot$.

2. Identification of flux-rope CMEs: Observed dynamics

The LASCO images of the CME shown in Fig. 24 exhibit features virtually identical to those of the SMM event in Fig. 5(c) that were interpreted as the projection of a dome-like structure. Although the recent morphological studies support the flux rope interpretation,[88,89,91,92] absent a direct observation of the 3-D magnetic and density structures, an interpretation based on 2-D images is ultimately insufficiently constrained and non-unique. The key additional constraint in the flux rope identification was the observed CME dynamics, i.e., if a CME is an erupting flux rope, then the theoretically calculated flux-rope dynamics must agree with the observed CME expansion.[87] The wide FOV of LASCO allowed one to track features such as a, b, c, d_1, and d_2

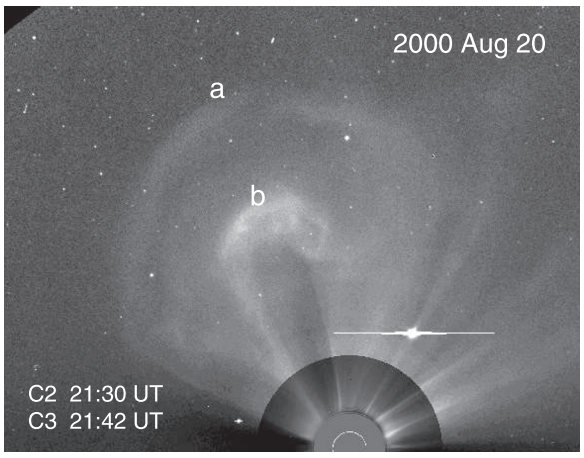

FIG. 27. CME observed on 20 August 2000. A C2-C3 composite image of a flux-rope CME viewed from the side, with the LE (a) and TE (b) of the flux-rope CME indicated. The bright feature at b is the coronal counterpart of the prominence, similar to that shown in Fig. 13(c). Viewed end-on, e.g., from the right, the prominence material would appear as a bright vertical structure in the cavity, as in Figs. 5(c) and 24. The saturated bright feature is a planet.

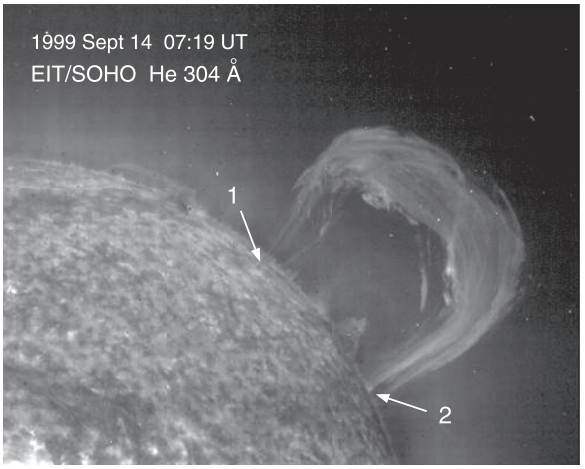

FIG. 28. Erupting prominence, observed in He 304 Å by EIT on board SOHO. The "legs" of the prominence are visible, denoted by "1" and "2." Footpoint "1" is in front of the limb.

through the initial acceleration and beyond. An important quantity is the aspect ratio, defined by

$$\Lambda(t) \equiv \frac{\mathcal{R}_b(t)}{D}, \tag{7}$$

where $\mathcal{R}_b \equiv Z_b(t) + R_\odot$ is the distance of b from Sun center, Z_b the height b from the photosphere, and $D(t) = |\mathbf{d}_1 - \mathbf{d}_2|$ the transverse width. The aspect ratio Λ embodies the coupled expansion in two orthogonal directions. The EFR solutions (below) were shown to simultaneously fit the trajectories of a, b, and c as well as the aspect ratio $\Lambda(t)$.[87] This comparison is more stringent than if only the LE motion is considered.

A more complete view of CME dynamics was afforded by a CME observed by the ground-based MK3/MLSO and LASCO instruments, yielding detailed data from $1.2R_\odot$ to $32R_\odot$. Morphologically, this CME was similar to the CME shown in Fig. 24 with the exception that the inferred flux-rope axis was more inclined relative to the ecliptic plane. Figure 29 shows the position-time data for the LE (squares) and centroid (circles) and the EFR solution for this event. These features are the counterparts of a and b in Fig. 24. (TE c, not shown to avoid clutter, is slower than the centroid.) Panel (a) shows the observed LE (solid) and centroid (dashed) trajectories. The theoretical solution replicates both trajectories throughout the FOV. Panel (b) shows the aspect ratio $\Lambda(t)$ and the flux injection function $d\Phi_p(t)/dt$ for this event (see Appendix for $d\Phi_p(t)/dt$). The data show that the observed $\Lambda(t)$ is maximum early in the MK3 FOV ($t <$ 19:30 UT), decreasing after this time. The calculated $\Lambda(t)$ replicates the data except for the first few data points. For these early times, the full width of the CME was not observed, so that the true values of Λ are equal to or less than the data points (squares). Panel (c) gives the speed of the LE a. The calculated TE speed (dashed curve) shows a comparable degree of agreement with data. The early acceleration phase was blocked by the occulter. The peak acceleration ended by 20:00 UT.

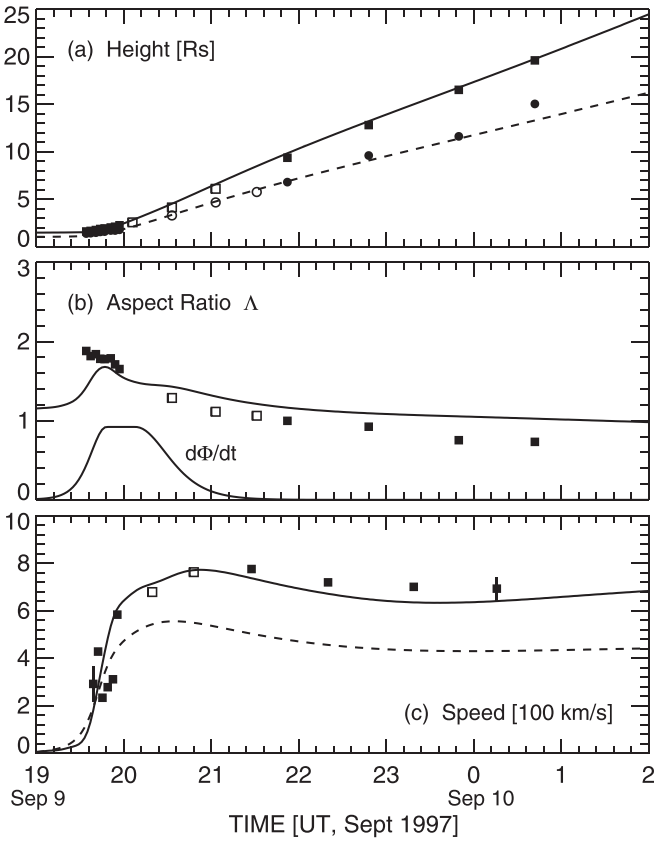

FIG. 29. Trajectory of the LE and transverse dynamics of the CME on 1997 September 9. MK3 and LASCO data (squares for LE and circles for the centroid) and the EFR model solution (solid curves for LE and dashed curves for the centroid). Solid symbols for the MK3 and C3 data and open symbols for the C2 data. (a) Projected heliocentric positions (in $R_\odot$). Error bars are ~1%–2%, roughly the size of the symbols. (b) Observed and theoretical aspect ratio Λ, Eq. (7). The error in Λ is ~10%. The first few points are most uncertain—probably too large—because the full width of the CME might not have been observed. Calculated flux injection $d\Phi_p(t)/dt$ for this solution is shown in units of 6×10^{18} Mx s^{-1}. (c) The projected speed V of the LE a (squares) and the centroid b. From Ref. 95.

The EFR solution replicates the correlation between the enhanced value of Λ and the acceleration peak, which approximately coincides with the rise phase of $d\Phi_p(t)/dt$. Similar temporal relationships have also been found in other events.[96,209] In the EFR model, the initial increase in $\Lambda(t)$ is caused by the increase in pinch force arising from an increasing $\Phi_p(t)$ that reduces the rate of increase in $D(t)$, and the subsequent decrease in $\Lambda(t)$ results from the faster expansion of $D(t)$ than $\mathcal{R}(t)$. This is characteristic of 3-D flux ropes with stationary footpoints expanding under the Lorentz hoop force, as will be discussed below. The calculated flux rope expansion in the two orthogonal directions is consistent with the observed CME dynamics.

Following the identification of the first flux-rope CME, much support for the new CME concept has been found based on dynamics[94–96,220,318] and morphology.[88,219,221,222,285,319–321] Thernisien *et al.*[88] constructed synthetic images of flux ropes[95] from a wide range of vantage points and showed that images of CMEs are generally consistent with being projections of 3-D hollow flux ropes. Similarly, the so-called halo CMEs[78] can be interpreted as projections of Earth-directed flux ropes.[320] It is now believed that most, if not all, CMEs are flux ropes.[89,92] Perhaps the most important observational improvement was the large FOVs of LASCO and SECCHI instruments that have allowed observation of CME dynamics in the entire 1 AU region. This is a unprecedented testbed for any proposed CME models.

F. Dynamics of solar flux ropes

As noted earlier, the Lorentz force is generally regarded as the "most likely force" driving CMEs and EPs.[271] The idea is that a current loop in the corona induces an image current in the infinitely conducting metal-like photosphere and experiences a repulsive Lorentz force. In equilibrium, this is balanced by the downward magnetic tension force due to the overlying B_c field. As the arcade footpoints are sheared, the current and the repulsive force increase quasi-statically. An eruption results when the forces are unbalanced by some "MHD instability," "catastrophic loss of equilibrium," "tether cutting" by reconnection, or some combination thereof. These concepts underlie essentially all models of CMEs and interpretations of simulation results.[233,238,239,244–246,248–250,252,264,269,270,292,322] In its basic form, the image-current force is treated using a linear current sheet or flux rope parallel to the photosphere.[236,252,266,271] Yet, the repulsive force due to a photospheric image current as the driver of CMEs has not been tested against observed CME dynamics, and possible image currents in the weakly ionized photosphere have not been evaluated.

In reality, a solar flux rope with its footpoints rooted in the photosphere is necessarily curved. Such a structure experiences a self force, the so-called hoop force, which arises from the self magnetic field of the current ($I_t \times B_p$). It is dependent on the major radial curvature $\kappa \equiv 1/R$ and is identically zero in a straight flux rope ($R \to \infty$). This Lorentz force has a textbook counterpart for a metallic current ring where pressure and toroidal field are absent.[323] The application to plasma structures was originally derived for axisymmetric equilibria in tokamaks[299,324] and introduced into the solar physics literature in a study of macroscopic equilibrium of 3-D solar loops with nonzero pressure.[310] It was later extended to the dynamics of nonaxisymmetric flux ropes with stationary footpoints.[85] For the solar application, the minor radial dynamics, minor radial variation along the flux rope, and the stationary footpoints during expansion are found to be essential.

In the first application to solar eruptions[85] and recent studies of the hoop force,[289,298,311,312] the minor radius was taken to be uniform along the flux rope. It was found early on that with this assumption, no solution could be found to simultaneously replicate CME dynamics near the Sun *and* MCs at 1 AU, the presumed counterpart of CMEs. This simplification becomes invalid as the flux rope expands because the apex minor radius grows much larger than the footpoint minor radius (Fig. 24). Extending the theory to allow the minor radius to be nonuniform, the calculated flux-rope dynamics were shown to be consistent with those of observed CMEs and MC structures at 1-AU.[36]

The above model-data consistency was still limited in that the evolved flux ropes at 1 AU could only replicate small MCs. The reason was traced to the fact that the tenuous but hot cavity plasma and the relatively cold but dense prominence mass were treated as one fluid. This is not physical: the former is coupled to the pressure force while the latter to gravity. The theory was extended to treat the two components separately.[86] The revised theory was shown to reproduce observed CME dynamics and CME ejecta at 1 AU consistent with the observed range of MCs, provided some prominence mass is included in the initial equilibrium. Specifically, the prominence mass affects the initial equilibrium magnetic field and therefore the Lorentz force and CME dynamics to 1 AU. This reinforces the concept that prominences are an integral part of CMEs.

This theory, now known as the EFR theory, has been tested against CME/EP trajectories observed by SOHO and STEREO with good agreement.[33,87,94–96,209,220,318] It has been shown that the solution that best matches the observed trajectory of a CME also predicts the measured magnetic field and the plasma parameters of the ejecta at 1 AU (Ref. 33) and the temporal profile of the associated SXR flare emissions in the low corona.[209]

The EFR equations evidently capture (1) the essential macroscopic physics of CME-prominence dynamics manifested in coronagraph data, (2) the evolution of the CME magnetic field, and (3) the physical connection between CME acceleration and associated solar flare energy release (SXR data) as manifested in close temporal correlation. The EFR theory is discussed in detail below.

1. Inductance and magnetic energy of solar flux ropes

Consider a toroidal magnetic flux rope in equilibrium as illustrated in Fig. 22. The poloidal magnetic flux enclosed by the partial torus and the photosphere is given by $\Phi_p(t) \equiv \oint B_p dA_\perp$, where $dA_\perp$ is an area element of integration. This quantity can be written as

$$\Phi_p(t) = cL(t)I_t(t), \tag{8}$$

where the total toroidal current is $I_t \equiv 2\pi \int J_t(r) r dr$, c is the speed of light, and $L(t)$ is the inductance, which depends on the geometrical size of the current structure.[323] If the minor radius $a(\theta)$ increases exponentially or linearly in θ from a_f at the footpoints to a_a at the apex, the self-inductance is[220,325]

$$L(t) = \frac{4\pi\Theta R}{c^2}(\mathcal{L} + \Delta), \tag{9}$$

where $2\pi\Theta R$ is the arc length of the flux rope, $\Theta(t)$ is the fraction of a complete circle,

$$\mathcal{L}(R, a_a, a_f) \equiv \frac{1}{2}\left[\ln\left(\frac{8R}{a_f}\right) + \ln\left(\frac{8R}{a_a}\right)\right] - 2 + \frac{\xi_i}{2}, \tag{10}$$

and $R(t)$ is the major radius and is assumed to be uniform along the flux rope. The additive quantity $\Delta(t)$ is determined by how a increases from a_f to a_a. For exponentially increasing $a(\theta)$[36,86]—motivated by the exponential decrease in the stratified pressure $p_c(Z)$—we have $\Delta(t) = 0$, and for linearly increasing minor radius,[325]

$$\Delta(t) \equiv 1 - \frac{\nu + 1}{2(\nu - 1)}\ln(\nu), \tag{11}$$

where $\nu(t) \equiv a_a(t)/a_f$ is a geometrical factor. Without affecting the basic physics and equations of motion, we will assume $a(\theta)$ to be exponential so that $\Delta = 0$. Thus, $L = (4\pi\Theta R/c^2)\mathcal{L}$ is used in the remainder of the paper. (If $a(\theta)$ is linear, $|\Delta/\mathcal{L}| < 0.2$–$0.3$ for CMEs within 1 AU).

The dimensionless internal self-inductance is

$$\xi_i \equiv \frac{2}{a^2 B_{pa}^2}\int_0^a r B_p^2(r) dr, \tag{12}$$

which is typically of order unity. For hollow surface current distributions, $\xi_i = 0$. For non-force-free distributed $J_t(r)$, $\xi_i \simeq 1$.[86] Here, $B_{pa} \equiv B_p(r = a)$ is the poloidal component at the edge of the current channel. The dimensional form is $L_i = (2\pi\Theta R/c^2)\xi_i$. The external self-inductance L_e is then $L_e = L - L_i$. The total poloidal magnetic energy is[323]

$$U_p = \frac{1}{8\pi}\int B_p^2 d^3\mathbf{x} = \frac{1}{2}LI_t^2. \tag{13}$$

As the structure expands, minor radius a_a at the apex becomes much greater than a_f at the footpoint ($a_a \gg a_f$), and Eq. (10) shows that

$$L(t) \simeq \frac{2\pi\Theta R}{c^2}\ln\left(\frac{8R}{a_f}\right). \tag{14}$$

This means that the poloidal magnetic energy U_p of an expanding flux rope resides predominantly in the legs where the field is strong ($B_p \propto I_t/a$) and $L \to L_e$. In contrast, the hoop force is determined by the local values of $\ln(8R/a)$. This is an essential 3-D effect, permitting the EFR equations to model the macroscopic dynamics of flux ropes in 3-D.

The fact that L mainly depends on R/a_f rather than R/a is important: $R(t)/a_f \propto R$ varies more rapidly than $R(t)/a(t)$, leading to the characteristic S_f-scaling law of expanding flux ropes manifested in the observed CME acceleration profiles[318] (Secs. III G 2 and III G 3). It also gives rise to an observable difference in the magnetic field pitch at the apex $\Gamma_a(t)$ and the footpoints $\Gamma_f(t)$ ($\Gamma_a(t) = const$ and $\Gamma_f(t) \neq const$, Appendix), indications of which can be found in observed prominences.[326,327] For the apex, observed CME data show that R/a—equivalent to Λ, Eq. (7)—increases significantly during the acceleration phase[95,96] (Appendix). See Fig. 29(b).

2. MHD forces on solar flux ropes: Equations of motion

Within the framework of ideal MHD, the local force density is given by $\mathbf{f}(\mathbf{x}) = (1/c)\mathbf{J} \times \mathbf{B} - \nabla p - \rho\nabla\phi_g$, where $\mathbf{J} = (c/4\pi)\nabla \times \mathbf{B}$, ρ is the mass density, and ϕ_g is the gravitational potential function. The major radial force per unit length of the flux rope is approximately[85]

$$F_R = \left(\frac{\Phi_P^2}{c^4 R L^2}\right) f_R(t) + F_d + F_g, \tag{15}$$

where F_d and F_g are the drag and gravitational forces, Φ_p is given by Eq. (8), and f_R is $\mathbf{J}\times\mathbf{B}/c-\nabla p$ integrated over a toroidal segment of unit length. Here,

$$f_R(t)\equiv \ln\left(\frac{8R}{a}\right)+\frac{1}{2}\beta_p-\frac{1}{2}\frac{\bar{B}_t^2}{B_{pa}^2}+2\left(\frac{R}{a}\right)\frac{B_c(Z)}{B_{pa}}-1+\frac{\xi_i}{2}, \tag{16}$$

is a dimensionless function of order unity.[220] Defining

$$h_R(t)\equiv \ln(8R/a)-1+\xi_i/2, \tag{17}$$

the hoop force is $F_{hf}=(\kappa I_t^2/c^2)h_R$, with $\kappa=1/R$. The average toroidal self-field $\bar{B}_t(t)$ gives the tension force $F_{tens}=-\kappa a^2\bar{B}_t^2/8$ along R, and $\beta_p(t)$ arises from ∇p

$$\beta_p(t)\equiv\frac{8\pi(\bar{p}-p_c)}{B_{pa}^2}, \tag{18}$$

where $\bar{p}$ and p_c are the average internal and coronal pressures. Thus, β_p is the pressure differential across the minor radius, which leads to the major radial force $F_p=(\kappa I_t^2/c^2)\beta_p$. The B_c term is the downward Lorentz force $F_c=I_tB_c/c$ (Fig. 23). Note that F_c has no curvature dependence. The form of $J_t(r)$ enters the analysis only through ξ_i and does not explicitly affect the other terms. For simplicity, $J_t(r)$ is taken to have the same functional form throughout the flux rope and $\xi_i=const$ is assumed.

The system of equations is closed by an adiabatic index of $\gamma\simeq 1.2$. This value is *ad hoc* but is found to yield SW properties consistent with *in situ* data out to about 4 AU. Reasonable coronal properties are also obtained near the Sun with $\gamma=1.05$.[328] These values correspond to good thermal conduction from the hot corona.

As the flux rope expands in response to increasing $\Phi_p(t)$, $L(t)$ varies according to Eq. (9), and the magnetic field components evolve according to

$$B_p(t)=2I_t(t)/ca(t),\quad \bar{B}_t(t)=\Phi_t/\pi a^2(t), \tag{19}$$

where $a=a_a$, $I_t(t)=\Phi_p(t)/cL(t)$, and $\Phi_t=const$.

The expression (16) is familiar in tokamak research and was derived by Shafranov[299] for an axisymmetric toroidal flux rope equilibrium (i.e., tokamak plasma) confined in a toroidal vacuum ($p_c=0$) vessel. The characteristic $\ln(8R/a)$ dependence of the "hoop force" on the major radial curvature $\kappa=1/R$ is evident. The overlying field B_c plays the role of the "vertical" field that balances the hoop force in tokamaks. Solar flux ropes, however, have a number of essential differences from tokamaks: they are embedded in the corona of pressure p_c with no metallic walls, non-axisymmetric with stationary footpoints, and highly dynamic. The finite ambient pressure, $p_c\neq 0$, means that $\beta_p<0$ is possible, which allows equilibrium flux ropes even with $B_c=0$ without violating the virial theorem.[310] In axisymmetric structures, there is no counterpart of the length scale S_f.

Applying Eq. (15) to the apex, the major radial motion is determined by

$$M\frac{d^2Z}{dt^2}=\left(\frac{\Phi_p^2}{c^4RL^2}\right)f_R(t)+F_g+F_d, \tag{20}$$

where $Z(t)$ is the height of the centroid of the apex, $M(t)\equiv\pi a^2\bar{\rho}_T$ is the total mass per unit length, and $\bar{\rho}_T(t)\equiv m_i\bar{n}_T(t)$ is the total mass density averaged over the minor radius, consisting of the cavity plasma ($m_i\bar{n}$) and prominence material ($m_i\bar{n}_p$) so that $\bar{n}_T\equiv(\bar{n}+\bar{n}_p)$. Mass M is ascribed to the centroid of a toroidal section (no spatial distribution).

The minor radial dynamics are approximated by

$$M\frac{d^2a(t)}{dt^2}=\left(\frac{I_t^2}{c^2a}\right)\left(\frac{\bar{B}_t^2}{B_{pa}^2}-1+\beta_p\right). \tag{21}$$

Given Eq. (18), this equation simply states that $\bar{B}_t$ and $\bar{p}$ tend to expand the minor radius $a(t)$ while B_{pa} and p_c tend to decrease the minor radius.

Equation (16) is based on the conjecture that the hoop force acting on a section of a nonaxisymmetric torus is determined by the *local* curvature κ. Accordingly, the local hoop force per unit length was obtained by dividing by $2\pi R$ the total force on an axisymmetric torus.[85] Subsequently, the local hoop force on a flux rope with arbitrary $R/a\gg 1$ was rigorously derived.[330] The derivation, which uses the principle of virtual work, shows that the *local* circular approximation, Eq. (16), is valid with error of $\mathcal{O}(a/R)$. Equation (15) shows that the hoop force vanishes in a straight flux rope: $F_R\propto R^{-1}\ln(8R/a)\to 0$ as $R\to\infty$. The *curvature* at a point on a curve is a non-local quantity because it depends on neighboring points and that magnetic field as well as the inductance is non-local.

Recall that B_c is the overlying coronal field perpendicular to the plane of the flux rope. In general, there is a toroidal component of the coronal field, B_{ct}, which is due to a current source external to the flux rope. This component enters the major and minor radial force equations as $\bar{B}_t^2-B_{ct}^2$,[299] where B_t refers to the toroidal self-field. The equations can be rewritten by replacing $\bar{B}_t^2$ with $B_t^{*2}\equiv\bar{B}_t^2-B_{ct}^2$ everywhere without affecting the solutions. If a component $B_{ct}\neq 0$ is given, it is B_t^{*2} that is directly computed, from which the flux rope field $\bar{B}_t$ must be obtained using $B_{ct}(Z)$. For CMEs, the EFR model has been used with $B_{ct}=0$. For thin coronal loops in an arcade (e.g., Fig. 11), $B_{ct}\neq 0$ may be more appropriate, which should make such loops "stiffer." In an axisymmetric flux rope model,[312] a dipole magnetic field due to a (subsurface) line current along the axis of symmetry was used to model B_{ct}. An MHD simulation of this configuration found it necessary to turn off the line current ($B_{ct}=0$) to produce eruption.[291]

3. Gravitational force on CMEs

Gravity is weak relative to the Lorentz hoop force but does significantly affect the long-time dynamics through the initial magnetic field (Sec. III G 1). The gravitational force per unit length at the apex is

$$F_g(t)=\pi a^2m_ig(Z)(n_c-\bar{n}_T), \tag{22}$$

where $n_c(Z)$ is the coronal density, $\bar{n}_T=\bar{n}+\bar{n}_p$,

$$g(Z) = g_\odot/(1 + Z/R_\odot)^2, \tag{23}$$

and $g_\odot = 2.74 \times 10^4$ cm s^{-2} at the solar surface. Gravity acts primarily on the cold prominence component of mass in the initial equilibrium, increasing the downward force without affecting the flux rope pressure. This is directly coupled to the magnetic field via the Lorentz force (Sec. III G 1). A parametric study in which $\chi_0 \equiv \bar{n}_{p0}/\bar{n}_0$ is varied shows that the values $5 < \chi_0 < 30$ produce results compatible with observed CME/EP dynamics near the Sun and properties of MCs at 1 AU.[86] Here, the prominence component is assumed to drain out and fall back to the Sun with about 15% entrained by the expanding flux rope, which is consistent with observational estimates. With $\chi_0 < 5$ or $\chi_0 > 30$, no solutions consistent with observed MCs are found. This clearly shows the CME flux rope and prominence mass must be integrally coupled to correctly model the CME-MC evolution.

4. Drag force

The drag force F_d describes the momentum coupling between the expanding flux rope and the ambient medium. For a flux rope of effective minor radius $2a$ presenting an area of $4a$ per unit length at the LE,[320]

$$F_d(t) = -2c_d a\rho_c(V_{LE} - V_{SW})|V_{LE} - V_{SW}|, \tag{24}$$

where c_d is the drag coefficient, $V_{SW}(Z)$ is the speed of the ambient SW (or corona), $V_{LE}(t) \equiv dZ_{LE}(t)/dt = V + 2w$ is the speed of the LE. This follows from $Z_{LE} = Z + 2a$, where $w(t) \equiv da(t)/dt$. If the CME LE is faster than V_{SW}, then $F_d < 0$ so that the SW retards the CME. If the SW overtakes the CME, then V_{LE} is replaced by $V_{TE} = V - 2w$, and $F_d > 0$ so that the SW adds to the outward driving force.

Equation (24) assumes that in a fully ionized corona-SW medium, a magnetized flux rope of minor radius $2a$ having a speed differential of $\Delta V \equiv V_{LE} - V_{SW}$ relative to V_{SW} displaces momentum density $\Delta P = \rho_c|\Delta V|$ per unit time. With the cross-sectional area of $4a$ per unit length, the flux rope transfers momentum at the rate of $4a\Delta P\Delta V$. Defining c_d in the usual form $F_d = -(1/2)c_d(4a)\Delta P\Delta V$, Eq. (24) follows.

The original drag model was couched in terms of aerodynamic drag for a solid cylinder ($w = 0$).[85] Its applicability to CMEs, which are deformable structures, is predicated on the validity of the scaling $F_d \propto \Delta V^2$, which was shown to be valid for a straight cylindrical flux rope in 2.5-D MHD simulations.[332,333] It was found that c_d strongly depends on the orientation of the ambient magnetic field $\mathbf{B}_{SW}$ relative to the flux rope axis: c_d is smaller ($c_d \ll 1$) if $\mathbf{B}_{SW}$ is parallel to $\mathbf{V}$ than if $\mathbf{B}_{SW}$ is aligned with the flux rope. The results showed that the values $c_d \sim$ 1–3 are reasonable for CME flux ropes. The 2.5D simulation could not realistically treat $\mathbf{B}_{SW}$ draped around the flux rope. Simple momentum transfer models, for example, deflection or specular reflection of fluid elements at the boundary surface yield $c_d = 1$ and $c_d = \pi$, respectively.

In reality, the simplification $w = 0$ (solid cylinder) is invalid for expanding CMEs ($w \neq 0$). Yet, with $c_d =$ 1–3, the theory successfully replicated CME dynamics observed within the LASCO FOV.[86,87,94–96] Beyond this distance ($\sim 32R_\odot$), however, the theory was found to be inadequate: regardless of the choice of c_d and input parameters, no solution could be found to replicate both LASCO and STEREO data. This was traced to the fact that with $w \neq 0$, the LE of the expanding CME displaces more ambient mass and faster, i.e., greater momentum transfer. This difference is cumulative and becomes pronounced over distances of a few tens of $R_\odot$. With $w(t) \neq 0$ in the revised Eq. (24) and the previously used values $c_d =$ 1–3, the EFR theory was able to replicate the observed CME trajectories in both the LASCO and STEREO FOV extending to 1 AU.[33,209] This is an example of the strong constraint imposed by observed dynamics over a sufficiently large distance. In the earlier analysis of a halo CME and associated MC,[320] $w \neq 0$ was also found to be necessary to match both the observed near-Sun dynamics and the MC at 1 AU, but no data along the CME path were available to test the calculated trajectory.

The original drag model with $w = 0$ has been used to model the deceleration of CMEs adopting equations of the form $MdV/dt = F_d$,[334–338] and the value of c_d has been estimated by fitting the solutions to observed CME trajectories.[334,338] This assumes that there are no significant forces other than drag on CMEs, but the observed data provide no evidence to support this. More to the point, the comparison is between different quantities: the computed CME motion is due to the drag force only while the observed CME motion is governed by the *net* force. Theoretical analyses show that CME dynamics in the SW are determined by the competition between the Lorentz force and drag force.[86,220] See Sec. III G 2.

Finally, the so-called "snow plow" effect can also produce a contribution that depends on $(\Delta V)^2$. The plowed material is then shed, which limits the total amount of material that can be accumulated. Some observational evidence of the snow-plow effect exists.[93] This effect has been modeled using the so-called virtual mass[332] in analogy to fluid dynamics,[339] with c_d replaced by $c_d/(1 + \rho_c/2\bar{\rho})$.[332,333,337] This mass-loading factor may be absorbed into the definition of c_d, provided $\rho_c/\bar{\rho}$ is slowly varying. For CMEs, the factor "2" is *ad hoc*, and the mechanism of virtual mass in CME drag has yet to be studied. Drag coupling to the SW is manifested in the MC speed distributions at 1 AU, showing a narrower spread than the CME speeds near the Sun,[340] supporting the theoretical prediction.[86]

5. 3-D geometrical constraint on the hoop force

During the expansion of a flux rope, the footpoints are assumed to be stationary ($S_f = const$), and for simplicity, major radius is taken to be uniform along the flux rope, i.e., $R(\theta) = const$. In contrast, $a(\theta) \neq const$. With $Z(t)$ given by Eq. (20), the major radius is

$$R(t) = \frac{Z^2(t) + S_f^2/4}{2Z(t)}. \tag{25}$$

Together with $a(t)$ from Eq. (21), Eq. (9) yields the inductance $L(t)$. Given Φ_p (Sec. III G), the toroidal current $I_t(t)$

$= \Phi_p(t)/cL(t)$ and poloidal magnetic field $B_p(t) = 2I_t/ca(t)$ are calculated. Although the model equations only treat $Z(t)$ and $a(t)$, the resulting dynamics are fully 3-D because the inductance $L(t)$ is for a 3-D flux rope. Thus, $L(t)$ self-consistently couples the magnetic field and expansion of the flux rope—the "M" and "HD" in MHD, respectively.

The above equation states that the toroidal axis is a circular arc, which implicitly assumes that the net major radial force, including the drag force, is symmetric around the flux rope. This is generally not the case. In particular, the ambient SW medium imposes a preferred direction on flux-rope dynamics via the drag force, and R/a is expected to be non-uniform along the flux rope. A more general treatment has been developed in which the transverse expansion is self-consistently and separately calculated.[331] Correctly modeling the transverse expansion is important for predicting the CME ejecta impact on the Earth, but it does not alter the nature of the forces. In the present paper, the simpler circular axis approximation is used.

6. Stationary footpoints of flux ropes

An important constraint on the flux-rope dynamics is that the flux rope footpoints be stationary in the photosphere, which is much denser ($n_s \sim 10^{17}$ cm^{-3}) than the corona ($n_c \sim 10^9$ cm^{-3} at the base). If the major radial force F_R on the footpoints is comparable to that on the apex, the characteristic ("terminal") speeds at the apex V_a^* and at footpoints V_f^* are related by

$$F_R \sim 4c_d a_f \rho_s V_f^{*2} \sim 4c_d a_a \rho_c V_a^{*2}, \tag{26}$$

where ρ_s (ρ_c) is the surface (corona) mass density. If c_d is comparable in both mediums, we obtain

$$\frac{V_f^*}{V_a^*} \sim \left(\frac{a_a \rho_c}{a_f \rho_s}\right)^{1/2} \sim 10^{-4}, \tag{27}$$

where Eq. (4) has been used. With $V_a^* \sim 10^3$ km s^{-1} and $a_a \sim a_f$ near the Sun during the initial acceleration, Eq. (27) gives $V_f^* \sim 10^{-4} V_a^* \sim 100$ m s^{-1}, indistinguishable from the ubiquitous "slow" speeds in the photosphere and consistent with Eq. (6). In the EFR theory, the footpoints are stationary in this sense, to be distinguished from ideal MHD "line tying" with infinite conductivity, Eq. (5). Note that the TI equation is a limiting case of Eq. (20) based on a number of important assumptions (next section).

In the solar physics literature, the flux-rope footpoints are often said to be "line-tied" to the photosphere ($\sigma, \rho = \infty$) via ideal MHD (Sec. III A). Isenberg and Forbes proposed to incorporate the line-tying of the footpoints into the derivation of the hoop force,[289] using a current loop with the footpoints embedded in an equipotential ($\mathbf{E} = 0$) surface and applying a magnetostatic image-current method. They required $B_t = const$ in the boundary. The derivation includes the Lorentz hoop force ($J_t B_p$) with the usual $\ln(8R/a)$ term and the repulsion from the image current, but assumes $B_t = 0$ and $\nabla p = 0$. An unusual feature in this work is that the current enters (and leaves) the infinitely conducting surface at the embedded footpoints. The standard method of images[323,341,353] excludes charges and currents from the conducting surface. It is based on the uniqueness theorem for boundary-value problems. Mathematically, the limit of physical charges entering the surface is singular, $E \to \infty$, which is not the physical limit in which the real and image charges would cancel, resulting in $E \to 0$. The method was not shown to be applicable to the configuration where the current enters the conducting surface.

The repulsion due to the image current has been invoked as the force responsible for eruption of EPs and CMEs,[236,252,266,271,354] and is regarded as an essential part of the toroidal hoop force.[289,354] This image current method was taken to be mathematically equivalent to the derivation of Garren and Chen.[330] For the case in which the flux rope is low and the return current is shallow below the photosphere, the repulsion from the return current has similar effects; see Fig. 8(b) of Ref. 330 for the calculated force. The return current is the physical current required to maintain conservation of current. If the flux rope is high or the return current (or image current, if any) is deeper below the photosphere, the repulsion, which rapidly decreases with distance, is insignificant relative to the hoop force due to the local curvature at the apex. This is because the hoop force is determined by the *local* curvature κ, with a correction of $\mathcal{O}(a/R)$. In eruption, $I_t(t)$ also decreases in time as the flux rope expands (Appendix), further reducing the long-range interaction with the photosphere.

Physically, if the surface has finite resistivity, the magnetic field can enter the surface, and any image current would be dissipated unless it is driven (Sec. III B). The condition $V_f^*/V_a^* \ll 1$ is also taken to imply that the photospheric and coronal timescales are "strictly separated," justifying the decoupling of subphotospheric and coronal dynamics. Different parts of a magnetic structure threading both regions have their respective velocity scales, Eq. (27), and dynamical decoupling need not be implied by $V_f^*/V_a^* \ll 1$. Simulations such as those of Refs. 297 and 277 provide a glimpse of the plasma/MHD dynamics involving this two-region system. The above analysis shows that regardless of dissipation, photospheric footpoints of a coronal structure generally move more slowly by a *finite* factor due to inertia.

7. MHD stability of flux ropes

In the 2D straight-cylinder geometry, flux ropes were found to be unstable, and it was regarded as puzzling that coronal loops were observed to be long-lasting.[342,343] Of the instabilities, the kink was proposed as a mechanism for eruption.[344–346] In 3-D toroidal equilibria with finite R/a, the force-balance conditions ($d^2Z/dt^2 = 0$ and $d^2a/dt^2 = 0$, Sec. III G 1) were found to constrain ($\bar{p} - p_c$) and B_p/B_t in such a way as to render the flux ropes stable.[310] Linearly, local Suydam stability[348] and the external kink stability[349] are both satisfied. Nonlinearly, 3-D flux rope tends to become more stable to the kink as it expands because twist per unit length tends to decrease.[347] This is favorable for application to solar flux ropes, which typically are quasi-

stationary for extended periods of time (days). Filaments and by implication the underlying flux ropes can be set into stable and damped oscillations ("winking" filaments) by large-amplitude perturbations from nearby eruptions,[350,351] which attests to their stability and robustness.

With $B_c = 0$ and Φ_p held constant, the nonaxisymmetric solar flux rope with stationary footpoints is absolutely stable to major radial expansion.[85] The timescale of oscillation and acceleration is $\tau_R = R/V_{Aa}$, where V_{Aa} is based on B_{pa} and $\bar{n}$ of the flux rope. If Φ_p is increased by a limited amount, the flux rope can expand and reach another equilibrium at a greater height. The new equilibrium is established by the balance between the upward hoop force $I_t B_p$ and the downward tension $I_p B_t$ and pressure gradient β_p. During the expansion, $I_t B_p$ does work against tension, and the ratio $\bar{B}_t^2/B_p^2$ increases, increasing tension relative to the hoop force. The linear stability analysis was extended to the case with $B_c \neq 0$.[329] With $B_c(Z)$ providing a potential barrier, a slow increase in Φ_p and the flux rope magnetic field can cause the flux rope to rise and overcome the potential barrier. Once the stability threshold is exceeded ($Z > Z_{crt}$), the flux rope expands. This scenario, termed "magnetic energy release," has been modeled.[325] Similarly, the torus instability (TI) model[298,352] calculates the "instability" conditions for specific forms of $B_c(Z)$; using the field profile $B_c(Z) \propto Z^{-n}$, the critical value n_{cr} has been derived such that a flux rope is unstable to major radial expansion for $n > n_{cr}$.

G. EFR theory of solar eruptions

In this section, the EFR theory described above is applied to CMEs, and the physical results are discussed with emphasis on the relationship between the equations of motion and observed dynamics.

1. Magnetic field of initial structure

The pre-eruptive coronal structure is assumed to be an equilibrium flux rope defined by a number of geometrical parameters, the important ones being S_f, Z_0, and R_0/a_0, where subscript "0" refers to the initial flux rope at $t = 0$. The model corona and IP medium into which the flux rope expands are based on empirical models and are specified as functions of Z.[86] These quantities are $n_c(Z)$, $T_c(Z)$, $p_c(Z)$, $B_c(Z)$, and $V_{SW}(Z)$. Here, $p_c(Z) = 2n_c k T_c(Z)$, where k is the Boltzmann constant and $T_c(Z = 0) = 2 \times 10^6$ K (= 172 eV) at the base of the corona. The coronal and SW outflow velocity $\mathbf{V}_{SW}$ is taken to be radial, with $V_{SW}(Z = 0) = 0$ and $V_{SW}(Z \to \infty) = V_{SW}^*$. At 1 AU, the canonical asymptotic values are $V_{SW}^* = 400$ km s^{-1} for the slow wind and $V_{SW}^* = 600$ km s^{-1} for the fast wind.[117]

In the initial flux rope, the magnetic field is determined—not specified—by the force-balance requirements: $d^2Z/dt^2 = 0$ and $d^2a/dt^2 = 0$ at $t = 0$. Including a $B_{ct} \neq 0$, the minor radial equilibrium yields

$$\frac{\bar{B}_t^{*2}}{B_{pa}^2} = 1 - \beta_p, \tag{28}$$

where $\bar{B}_t^{*2} = \bar{B}_t^2 - B_{ct}^2$. Eliminating $\bar{B}_t^{*2}$ from $d^2Z/dt^2 = 0$, we obtain B_{pa} in terms of $B_{c0} \equiv B_c(Z_0)$ and pressure differential $\bar{p}_{T0} - p_{c0}$ at the initial apex height Z_0:

$$B_{pa0} = \frac{R_0}{a_0}\Lambda_R^{-1}\left[-B_{c0} + \left\{B_{c0}^2 - \left(\frac{a_0}{R_0}\right)^2 \Lambda_R\left[8\pi(\bar{p}_T - p_c) + 4\pi m_i R_0 g_0 (n_c - \bar{n} - \bar{n}_p)\right]\right\}^{1/2}\right], \tag{29}$$

where $B_{pa0} = B_{pa}(Z_0)$, $\Lambda_R \equiv \ln(8R_0/a_0) - 3/2 + \xi_i/2$, and $g_0 = g(Z_0)$. Here, the external field B_{ct} is included to show how it can be eliminated. The total pressure is $\bar{p}_T = 2\bar{n}k\bar{T} + 2\bar{n}_p k\bar{T}_p$, where subscript p on scalar quantities refer to prominence while unsubscripted quantities refer to the hot cavity plasma. On vector quantities, p designates *poloidal* component or direction. Note that $\bar{T}_p \ll \bar{T}$, with the bar denoting quantities averaged over the minor radius. The above equation shows that for given B_{c0}, the poloidal field for the initial equilibrium is $B_{pa0} \sim -(2R_0/a_0)B_{c0}$ so that $|B_{pa0}| > |B_{c0}|$ for typical CME flux ropes for which $R_0/a_0 \simeq 2$.[96] Equilibrium is also possible for $B_c = 0$ provided $\beta_p < 0$ (i.e., $\bar{p} < p_c$).[310] Equation (29) is characteristic of toroidal flux rope equilibria with finite R/a.

Inserting $\bar{T} = T_c \simeq 2 \times 10^6$ K and $B_c \simeq 1$ G into Eq. (29), we find $B_{pa0} \approx 3$ G. For CME-like flux ropes, $B(r = 0) \simeq 3B_{pa}$[33,86] so that $B(r = 0) \simeq 10$ G, which is comparable to the estimated magnetic fields in quiescent prominences.[55,56] Significantly, prominence magnetic fields were found to increase with height.[55] This is consistent with the model flux-rope structure (Fig. 22), having maximum field on the axis ($r = 0$).[133,138]

2. Main and residual acceleration phases

The observed acceleration of CMEs provides a direct measure of the net force. Two observed quantities of importance are the profile of acceleration and geometrical dimension of the eruptive structure, in particular S_f. CME acceleration is well documented based on the data from several space-borne and ground-based telescopes.[67,70,355–358] The data show that CMEs exhibit one main acceleration peak close to the Sun, typically below $4R_\odot$,[70,321,356,358] followed by slower acceleration or deceleration extending to

$30R_\odot$ (SOHO)[285] and beyond. To understand the forces, one must establish the equations of motion whose physical solutions can correctly replicate the observed CME dynamics.

To show the spatial and time dependence of CME acceleration, write Eq. (20) as

$$\frac{d^2Z}{dt^2} = \frac{\Phi_p^2}{8\pi\mathcal{M}_T\Theta R^2\mathcal{L}^2} f_R + (F_d + F_g)/M, \tag{30}$$

where $\mathcal{M}_T(t) \equiv 2\pi\Theta RM$ and F_d and F_g do not depend on curvature or magnetic field. This can be written as

$$\frac{d^2Z}{dt^2} = \frac{R}{\tau_R^2} f_R + (F_d + F_g)/M, \tag{31}$$

where $\tau_R \equiv R/V_{Aa}$, $V_{Aa} \equiv B_{pa}(t)/(4\pi\bar{\rho}_T)^{1/2}$, and $\bar{\rho}_T(t)$ is given following Eq. (20). Defining

$$k_R \equiv \frac{1}{R\ln(8R/a_f)} \tag{32}$$

and using Eq. (14), Eq. (30) has the form

$$\frac{d^2Z}{dt^2} = \frac{1}{2\pi\Theta\mathcal{M}_T} k_R^2(t)\Phi_p^2(t) f_R + (F_d + F_g)/M. \tag{33}$$

The factor k_R^2 arises from $1/R^2\mathcal{L}^2$ above and captures the inductive and geometrical properties of the hoop force acting on an expanding flux rope. With the major radial curvature $\kappa \equiv 1/R$, we have the dominant scaling

$$\frac{d^2Z}{dt^2} \sim \kappa^2\left[\ln(8R/a_f)\right]^{-2} f_R, \tag{34}$$

where f_d and f_g with no dependence on curvature, as well as Φ_p, $\mathcal{M}_T$ and Θ have been dropped for simplicity; this does not affect the scaling discussion here.

Evaluating $dR/dZ = 0$ using Eq. (25), we find that κ is maximum at $Z = Z_*$ where

$$Z_* = S_f/2. \tag{35}$$

At this height, the toroidal axis is semicircular. Consider an initial flux rope and its expansion. Figure 30 shows how geometry determines the curvature and therefore the hoop force during the expansion. If the initial flux rope is flatter than a semicircle (loop 1), Eq. (25) shows $R_1 > S_f/2$. As the flux rope apex rises, R decreases, reaching minimum, i.e., maximum κ and k_R, at $Z = Z_*$ (loop 2, $R_2 = S_f/2 < R_1$). Thus, acceleration peaks at $Z \simeq Z_*$, Eq. (34).

Past this peak (loop 3, $Z > Z_*$, $R_3 > R_2$), acceleration decreases with k_R according to

$$\frac{d^2Z}{dt^2} \simeq \frac{k_R^2(t)}{k_{R*}^2}\left(\frac{d^2Z}{dt^2}\right)_* = Q_R(t)\left(\frac{d^2Z}{dt^2}\right)_*, \tag{36}$$

where the asterisk denotes values at $Z = Z_*$, with $k_{R*} \equiv k_R(Z_*) = [(S_f/2)\ln(4S_f/a_f)]^{-1}$. Thus, the CME acceleration is rapidly "quenched" by the factor

$$Q_R(t) \equiv \frac{k_R^2}{k_{R*}^2} = \left[\frac{(S_f/2)\ln(4S_f/a_f)}{R\ln(8R/a_f)}\right]^2. \tag{37}$$

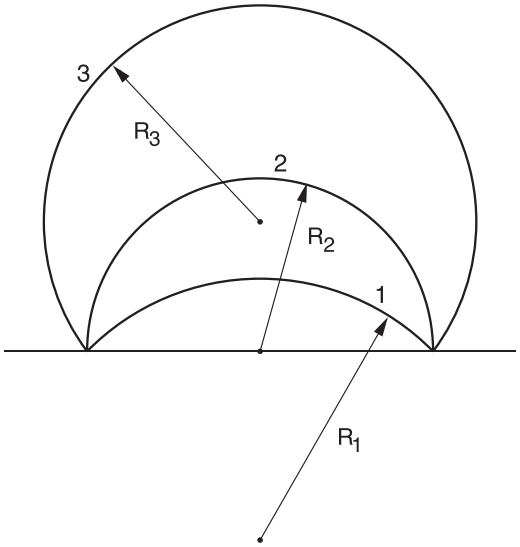

FIG. 30. Schematic of a rising flux rope represented by arcs 1, 2, and 3, having radii of curvature R_1, R_2, and R_3, respectively. Curvature is $\kappa \equiv 1/R$. Curvature is maximum for arc 2: $\kappa_2 > \kappa_1, \kappa_3$. Reproduced with permission from J. Chen and J. J. Krall, Geophys. Res. **108**, 1410 (2003). Copyright 2003 Wiley.[220]

This quenching factor—$Q_R \sim (S_f/R)^2(\ln S_f/\ln R)^2$—is significantly stronger than $R^{-2}(t)$, and the quenching occurs on the scale S_f in height. For concreteness, define Z_m as the height where the acceleration is 1/4 of the maximum, i.e., $Q_R = 1/4$. This condition can be solved for Z_m, yielding

$$Z_m \simeq 3Z_* = (3/2)S_f. \tag{38}$$

Thus, the bulk of acceleration is limited to below Z_m, and CME acceleration generally should have one main peak. This phase is referred to as the *main acceleration* phase.[220] The subscript "m" refers to "main." In this phase, the net force is predominantly determined by the competition between the hoop force (I_tB_p) and the downward Lorentz force I_tB_c, with a significant but smaller contribution from the tension I_pB_t.

For $Z > Z_*$, the Lorentz hoop force monotonically decreases with expansion, with the net acceleration now determined by the competition between the hoop force and the drag force F_d. This phase is referred to as the *residual acceleration* phase.[220] The "main" and "residual" acceleration phases are distinguished by the dominant contributors to the net force. These phases correspond to the empirically identified "acceleration" and "propagation" phases, respectively.[219]

Note that the actual height $\tilde{Z}_*$ of maximum acceleration is determined by $k_R^2(t)\Phi_p^2(t)f_R(t)$. While k_R^2 decreases with time t, Φ_p and f_R both increase for $Z > Z_*$. Thus, the observable $\tilde{Z}_*$ is slightly greater than Z_*.

It is instructive to examine the individual force terms in Eq. (16) applied to an observed CME. Figure 31(a) shows the individual forces calculated for the CME of 9 September 1997. The EFR solution for this event from which these terms are computed has been presented in Fig. 29. In the initial flux rope, the equilibrium is established mainly by the balance between the hoop force F_{hf} (curve 1), Eq. (17), and

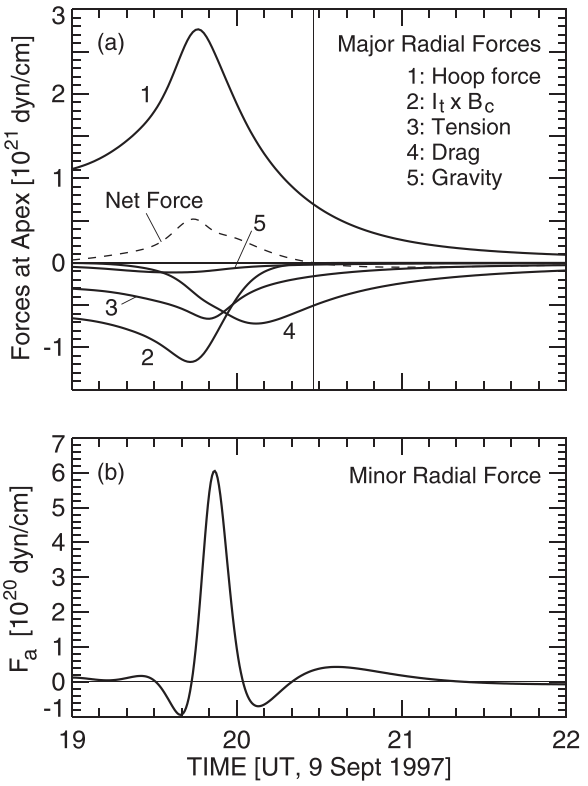

FIG. 31. Forces on the apex of the CME of 1997 September 9. The forces are calculated using the best-fit EFR solution shown in Fig. 29. The solution yields $M_T = 2.8 \times 10^{16}$ g, of which a half is the cavity mass, and $S_f \simeq 0.7R_\odot$, a typical CME source dimension. (a) Major radial forces [Eq. (15)]. The initial equilibrium is dominated by the F_{hf} (curve 1) and F_c (curve 2), with F_{tens} (curve 3) making a significant but relatively small contribution. The vertical line marks the end of the main acceleration phase. (b) Minor radial force [Eq. (21)] at the apex.

$F_c = I_t B_c/c$ (curve 2), with tension F_{tesn} (curve 3) playing a smaller but significant role. The flux rope is initialized to be nearly neutrally buoyant and nearly force-free: $F_g, F_p \ll F_{hf}$ (F_p is comparable to F_g and is not shown). The predicted total initial mass of the flux rope is $M_T = 2.8 \times 10^{16}$ g, of which a half is taken to be the cavity mass. The hoop force F_{hf} peaks at $t \approx$ 19:45 UT ($\sim 2.7 \times 10^{21}$ dyn cm^{-1}), which is quenched to 1/4 of the maximum value at about $t =$ 21:29 UT (dashed vertical line). This defines the end of the main acceleration phase. The ensuing residual acceleration ($t >$ 21:29 UT) is mainly the net of the hoop force and drag force (see Ref. 86). The decrease in F_d after $t \approx 20$ UT is mainly due to the decreasing ρ_c. Figure 31(b) gives the *net* minor radial force F_a, Eq. (21). The maximum value of F_a is comparable to that of the net radial force F_R.

The calculated net force is consistent with a recent observational determination of the driving force on a CME of estimated mass $\sim 3 \times 10^{15}$ g:[364] the net force reached $\sim 3 \times 10^{19}$ dyn at $\mathcal{R} \sim 3R_\odot$, rapidly decreasing to and remaining at $\sim 3 \times 10^{18}$ dyn from $7R_\odot$ to $18R_\odot$. This is a factor of 10 smaller than the net force on the 9 September 1997 CME with a calculated $M_T = 2.8 \times 10^{16}$ g.

The minor radial dynamics are important. A number of models have used only the major radial equation.[76,266,289,298] Often, the minor radial equation (21) is neglected. The TI model[298] explicitly eliminates this equation by assuming $d^2a(t)/dt^2 = 0$ and $\beta_p = 0$. Equation (28) shows that these two simultaneous conditions constrain the self-fields such that $\bar{B}_t^2(t)/B_{pa}^2(t) = 1$. Furthermore, in order to remove the explicit occurrence of $a(t)$ in Eq. (15), they impose $R/a = const$. Figure 31(b) shows that $d^2a/dt^2 \neq 0$ and Fig. 29(b) shows that both theoretical and observed aspect ratios $\Lambda(t)$, which is directly related to R/a, are not constant. The inability to physically evolve B_t in the flux rope has adverse implications in terms modeling eruptions, in particular, the so-called *failed eruptions*.[365] It is noted that the system does not evolve in a force-free manner even if a flux rope is force-free ($\mathbf{J} \times \mathbf{B}/c = 0$) at one instant of time. This is because the expansion of the flux rope volume $\pi a^2(t)R(t)$ generally causes $\bar{p}(t)$ to evolve differently from $p_c(Z)$ where $Z(t)$ is the apex centroid height. Therefore, $\beta_p(t)$ is not constant in time. In the linear regime, however, $d^2(\delta a)/dt^2 \sim (a/R)(d^2(\delta Z)/dt^2)$ allows one to use the approximation $d^2a/dt^2 \approx 0$, but $\beta_p(t) \neq 0$ must be allowed.[85] This approximation is invalid beyond the linear regime.

3. Constant-S_f flux-rope scaling law

The above analysis led to the observable prediction that CME acceleration peaks at $Z = Z_{max}$ satisfying

$$Z_* < Z_{max} < Z_m. \tag{39}$$

This S_f scaling and the quenching factor Q_R are geometrical effects characteristic of the hoop force, independent of the magnitude of acceleration and flux rope size.

In this section, we examine how the S_f-scaling law can be manifested in the observable CME and EP trajectory data. First, S_f refers to the footpoints of the magnetic flux rope, which cannot be directly observed. We therefore use a number of observational proxies to estimate S_f. See, for example, the PIL in Fig. 9(b): S_f is the chord connecting the two ends of a PIL or prominence footpoints. Second, for prominences (e.g., Fig. 28), the model CME structure (Fig. 22) defines a geometrical relationship between the magnetic field and the prominence density structure: $S_f = S_p + 2a_f$.[318]

For CMEs and EPs, the footpoint separation S_f and the apex height Z_{max} at which the acceleration is maximum can be observationally determined. Such measurements were made for 17 CMEs and EPs, and the relationship between the measured Z_{max} and S_f was investigated. The CMEs were observed by LASCO, and the prominence data were derived from LASCO observation or the Nobeyama Radioheliograph (NoRH) observation at the Nobeyama Radio Observatory (NRO, Japan).[366] Figure 32 shows the results, where the vertical axis is the measured Z_{max} and the horizontal axis is the measured S_f based on observed proxies. The solid circles (open triangles) show the data for the observed EPs (CMEs). The S_f-scaling law, Eq. (39), requires that the data points lie between two straight lines, $Z_{max} = S_f/2$ (line A) and $Z_{max} = (3/2)S_f$ (line B). See Eqs. (35) and (38). This figure implies that the acceleration profiles of all the CMEs and EPs in this set of events satisfy the S_f-scaling law. The open diamond marked by S is an MHD simulation of a flux rope with stationary footpoints,[291] which is consistent with the predicted S_f-scaling. It has also been noted that the main

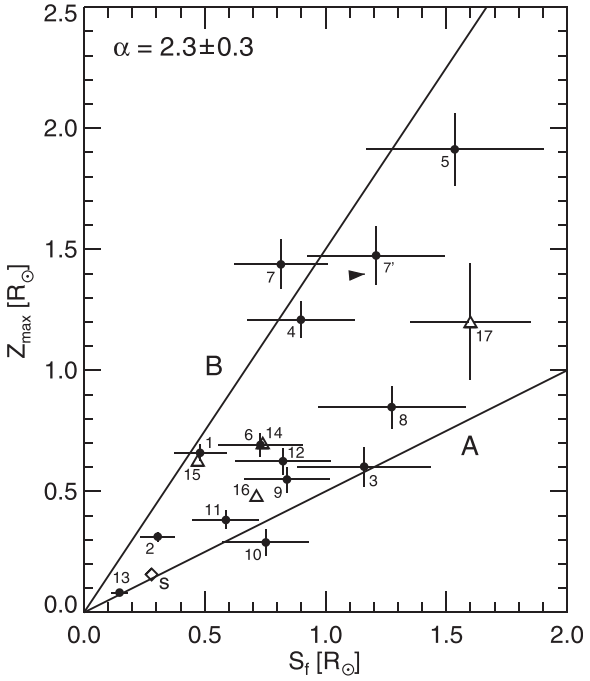

FIG. 32. Plot of observationally inferred S_f vs. Z_{max}, where S_f is the distance between the flux-rope footpoints. EPs are represented by filled circles, and CMEs are shown as open triangles. Line *A*: $Z_{max} = S_f/2$, Eq. (35). Line *B*: $Z_{max} = (3/2)S_f$, Eq. (38). $\alpha = R_0/a_0 = 2.3$ for the sample of events. The uncertainty in estimated α, taken to be $\Delta\alpha \pm 0.3$, results in uncertainties in both S_f and Z_{max}. The error bars show the estimated total error due to height measurements and Δα. Data points 7 and 7′ correspond to two possible values of S_f for the back-side event 7. The diamond marked is from an MHD simulation.[291] From Ref. 318.

acceleration duration is proportional to the source region dimensions,[367] in agreement with Eq. (38).

The parameter $\alpha(t) \equiv R(t)/a_a(t)$ refers to the magnetic flux rope and is not directly measurable. For the prominence, it is derived from the CME-prominence geometrical relationship $S_f = S_p + 2a_f$ assumed in the EFR theory. For the events in Fig. 32, the average value of α is $\bar{\alpha} = 2.3 \pm 0.3$. Values of $\alpha = 2$–2.5 have been found in previous studies.[87,94,96] The quantitative agreement seen in Fig. 32 supports the assumed geometry [Figs. 22 and 25(a)] and observed CME-EP morphology (Fig. 27).

In a study of CME kinematics observed by the MK3 K-coronameter between 1.2 and $2.4R_\odot$ (projected),[356] it was reported that CMEs associated with flares showed little acceleration in the FOV while those associated with prominences exhibited significant acceleration (say, greater than $40\,\mathrm{m\ s^{-2}}$). The interpretation is that the acceleration is localized below $\sim 1.2R_\odot$—"impulsive"—for the former class while it occurs "gradually" over greater heights for the latter. Similarly, it was reported[70] that active region-associated CMEs, of which flare-associated CMEs would be a subset, tend to be impulsive compared to prominence-associated CMEs. The median acceleration of prominence-associated CMEs is $\sim 50\,\mathrm{m\ s^{-2}}$ (averaged over the MK3-SMM FOV, probably excluding the main acceleration phase for most events), while the active region-associated CMEs have the median value of $\sim 160\,\mathrm{m\ s^{-2}}$,[70] with higher values ($> 1000\,\mathrm{m\ s^{-2}}$) inferred in some events.[70,321,355,362] Based on these perceived differences, it was proposed that two distinct acceleration mechanisms exist.[356,359–361,363] Indeed, a qualitative model was advanced to explain the postulated CME types based on different reconnection scenarios in different magnetic configurations: gradual for normal polarity versus impulsive for inverse polarity.[361]

In coronagraph images, a certain amount of the initial dynamics is occulted. The amount of unobserved dynamics is minimum when the event is on the limb in the FOV. More of the initial acceleration is visible, and the observer would classify it as a "gradual" event. If the same CME is directed more toward (or away from) the observer, much of the main acceleration phase may be blocked by the occulter, leading to the classification of an "impulsive" CME. This projection effect was excluded in the original analysis.[356] Theoretically, the acceleration of a more compact flux rope with a smaller S_f (flare- and active region-associated events) reaches maximum and is then quenched at a lower height (the $S_f/2$ scaling, above). This would be interpreted as impulsive according to the above definition. Prominence-associated flux ropes are typically longer—have greater S_f—than compact active region flux ropes, so that the main acceleration phase extends higher—$Z_{max} \sim S_f/2$—than that for compact CMEs. They would be called "gradual." If the size of the eruptive structure (specifically, S_f) and the projection effect are accounted for, no bimodal distributions of CME acceleration are indicated.[220] This is consistent with more detailed analyses of observed CME acceleration profiles.[368–370]

The S_f-scaling law is reminiscent of an earlier finding[293] that a flux-rope prominence becomes unstable at apex height $\sim S_f/2$. The two results are sometimes presented as similar,[371] but the S_f scaling law refers to the height where the acceleration peaks rather than to a stability threshold, two distinct physical processes.

4. Uniqueness of S_f scaling

Magnetic fields in the corona cannot be directly measured, and any inference on the structure has intrinsic uncertainties. We have emphasized the importance of dynamics as an additional *observable* discriminator. The preceding discussion focused on one such property, the S_f-scaling law, that is characteristic of partial toroidal flux ropes driven by the Lorentz hoop force. Although Fig. 32 supports the S_f-scaling law in the data, it cannot prove this interpretation as unique. It is certain, however, that equations for flux ropes with no counterpart of S_f would lead to different solution sets.

For example, Kliem and Török[298] proposed a model of the onset of CME acceleration, often referred to as the "torus instability" (TI). This work calculates the dynamics of a force-free flux rope in an ambient field of the form $B_c \propto Z^{-n}$ and evaluates the critical n_{cr} such that for $n > n_{cr}$, the flux rope cannot be held in equilibrium by B_c. This has been used to interpret observations[372] and laboratory experiments.[365] The TI equation is the $\beta_p = 0$ limit of Eq. (20), along with $R/a = const$ and $d^2a/dt^2 = 0$, which leads to $\bar{B}_t^2/B_{pa}^2 = 1$ (Sec. III G 2). The TI equation in the notation here, $M(d^2Z/dt^2) = (\kappa I_t^2/c^2)(h_R - 1/2) + F_c$, has the same apparent structure as the EFR equation (16), where h_R is given by Eq. (17). It is, however, axisymmetric with no

footpoints so that the length S_f does not occur. To adequately replicate observed CME acceleration, an additional assumption, $I_t(t) = const$, was imposed to mimic stationary footpoints. This led to solutions in better agreement with observed CME acceleration,[298] showing that the internal scale S_f is essential for modeling CME dynamics. The disadvantage of the above method is that $\Phi_p = cLI_t \neq const$ as L increases, violating the assumption $\Phi_p = const$.[373]

Roussev *et al.*[291] carried out a 3-D MHD simulation of flux ropes with different initial field line "twist" (i.e., pitch angle). The initial structure (Fig. 33) is based on the axisymmetric toroidal flux rope proposed by Titov and Démoulin (TD),[312] identifying the upper part of the torus with the coronal structure. The simulation footpoints are "line-tied" to the conducting boundary ($z = 0$) with high but finite mass density and low plasma temperature compared to the corona. The transition to the corona occurs in a layer of thickness $\sim 6 \times 10^3$ km. Unlike the CSHKP simulations above,[274,276,278] the footpoints are held stationary. The TD model employs a pair of subsurface "magnetic charges" ($\pm q$ at $x = \pm L$, $z < 0$ in the figure) to generate a dipolar overlying magnetic field B_c and a line current (I_0) at some depth to generate a toroidal component B_{ct} in the corona. It was found to be necessary to set $I_0 = B_{ct} = 0$ to produce an eruption. This flux rope—stationary but non-equilibrium with sufficient magnetic field twist, i.e., toroidal current—was able to overcome B_c and erupt away. With less twist, the flux rope rose and reached a new equilibrium height.

With $I_0 = 0$, the simulated flux rope is essentially the same as the EFR structure [see Figs. 23 and 33(a)]. It is, therefore, subject to the S_f scaling law. In the eruptive case, the initial flux rope has $Z_0^R = 8 \times 10^4$ km and $R_0^R = 10^5$ km, so that $S_f^R = 1.96 \times 10^5$ km from Eq. (25). Here, "R" refers to the *Roussev* et al. simulation. Judging the peak acceleration to occur at time $t \simeq$ 5–6 min [Fig. 33(b)], one obtains $Z_{max}^R \simeq 1 \times 10^5$ km. This is consistent with Eq. (39) with $Z_*^R = 0.98 \times 10^5$ km (diamond *S*, Fig. 32). The eruptive and non-eruptive solutions are nearly indistinguishable until the apex reaches 4–5 times the initial height. The S_f scaling is unaffected.

As for CSHKP arcade models in 3-D, they necessarily develop footpoints (e.g., Fig. 17). If stationary footpoints are fully formed before the main acceleration phase, the EFR theory and the S_f scaling should be applicable. This can be tested by CSHKP simulation models such as those discussed in Sec. III A. Indeed, the Roussev *et al.* simulation seems to supports this expectation, although it has reconnection below the flux rope not included in the EFR theory. Roussev *et al.* interpreted their simulations in terms of an axisymmetric flux rope model that does not possess the S_f scale.[312] Physically, however, the simulated equations more accurately describe the EFR flux rope with $S_f = const$.

H. EFR theory: Physical predictions

1. Onset of eruption

Consistent with the observed persistence of pre-eruption structures, an initial flux rope satisfying $d^2Z/dt^2 = 0$ and $d^2a/dt^2 = 0$ is stable to various MHD instabilities[87,310] but

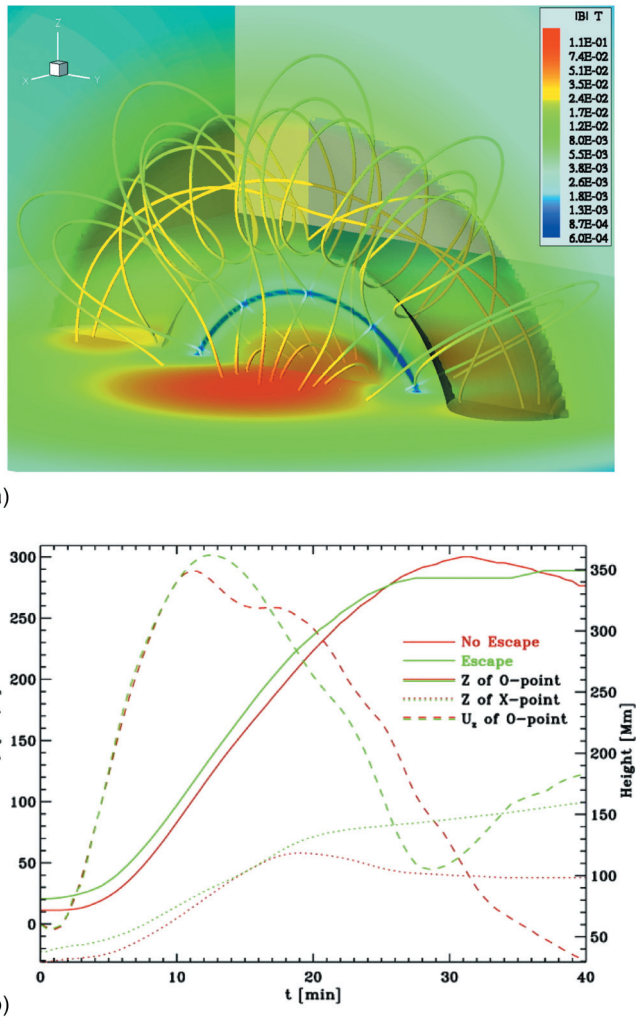

FIG. 33. Numerical simulation of flux rope dynamics. (a) 3-D flux rope with stationary footpoints. The solid lines are magnetic field lines, and the color code indicates the magnetic field strength in units of tesla. The surface shaded in gray is an isosurface of $B_z = 0$. The flux rope is initialized out of equilibrium. The cartesian coordinate system is shown. (b) Simulation results for two flux ropes: one eruptive (green) and the other non-eruptive (red). Right axis: Height-time curves for the centroid of the apex (solid curve) and the X-point below the flux rope (dotted curve). Left axis: Apex velocity (dashed curves). Reproduced with permission from Roussev, Astrophys. J. Lett. **588**, L45 (2003). Copyright 2003 IOP Science.[291]

may be driven out of equilibrium. Krall *et al.*[325] investigated a number of physical scenarios within ideal MHD and found that poloidal flux injection produced the best fit to the LASCO CME trajectories. A similar finding was made in a 2-D MHD simulation.[37] If the poloidal flux function $\Phi_p(t)$ is increased, I_t increases according to $I_t(t) = \Phi_p(t)/cL(t)$, causing $f_R(t)$ to increase. This continues until the flux-rope expansion causes $L(t)$ to increase faster than $\Phi_p(t)$. Mathematically, it is convenient to specify the function $d\Phi_p(t)/dt$,[86] from which $\Phi_p(t)$ can be calculated: $\Phi_p(t) = \int_0^t (d\Phi_p/dt')dt'$. The function $d\Phi_p(t)/dt$ is the rate at which a packet (pulse) of *poloidal* flux enters the flux rope ("injected") from a source outside the initial structure and is referred to as the *poloidal flux injection* function. Once $d\Phi_p(t)/dt$ is given, the mathematical solution of Eqs. (20) and (21) is uniquely determined. No mechanism for $d\Phi_p/dt$ has been specified, but Appendix gives the functional form,

a generic pulse, used in the theory. To model an observed CME, $d\Phi_p(t)/dt$ is calculated (not specified) subject to the requirement that the solution fit the CME data. Figure 29(b) shows a $d\Phi_p(t)/dt$ calculated for the observed CME.

The injection of poloidal flux into a structure having $\Phi_p(t)$ and $L(t)$ corresponds to the injection of poloidal magnetic energy U_p at the rate of

$$\frac{dU_p(t)}{dt}\Big|_{inj} = \frac{\Phi_p(t)}{c^2 L(t)}\frac{d\Phi_p(t)}{dt}. \tag{40}$$

Here, $U_p(t) = (1/2)L(t)I_t^2(t) = (1/2)\Phi_p^2(t)/c^2L(t)$ is the poloidal energy of the flux rope. As Φ_p increases, the flux rope expands, and $L(t)$ evolves. The resulting change in the magnetic energy, $-(1/2)(\Phi_p^2/c^2L^2)/(dL/dt)$, does not affect the amount of the injected poloidal energy. Thus, the total injected energy is

$$\Delta U_p|_{inj} = \frac{1}{c^2}\int_0^t \frac{\Phi_p(t')}{L(t')}\frac{d\Phi_p(t')}{dt'}dt'. \tag{41}$$

Although $I_t(t)$ initially increases with $\Phi_p(t)$, $I_t(t) = \Phi_p(t)/cL(t)$ can decrease if $L(t) \propto R\ln(8R/a_f)$ increases fast enough. This occurs when $dI_t(t)/dt < 0$, i.e.,

$$\frac{1}{L}\frac{dL}{dt} > \frac{1}{\Phi_p}\frac{d\Phi_p}{dt}, \tag{42}$$

which occurs when the apex height Z exceeds $Z_* = S_f/2$, reinforcing the importance of the length S_f in CME dynamics. At the apex, the initial increase in $I_t(t)$ results in an increase in $B_{pa}(t) \propto I_t(t)/a(t)$ and a decrease in $a(t)$. In the footpoints where $a_f = const$, $B_p \propto I_t$ with $\bar{B}_t = const$. Thus, the magnetic pitch of the flux rope at the apex varies differently from that at the footpoints (Appendix and Sec. III F 1). The component B_p is nominally horizontal in and below the photospheric surface, and the toroidal component B_t is "vertical." The constancy of B_t is consistent with magnetogram data that the vertical (LOS) flux does not show significant changes during eruptions.[304,305] Both field components are expected to be highly filamentary on small scales (e.g., Fig. 8) and complex in the high-β medium (Sec. IV C).

It should be noted that the "photosphere" in the EFR model is the base of the corona. The actual connection to the photosphere is not specified, except that I_t is conserved across the boundary layer ($\nabla \cdot \mathbf{J} = 0$). No present-day models of eruption including simulation models (Sec. III A) treat the boundary region, across which the plasma pressure varies by approximately five orders of magnitude (Sec. II A 4). The rapid variations in magnetic fields in this layer are currently modeled using force-free and non-force-free models, and much remains unknown.[374,375] High-resolution observations (e.g., Fig. 8) suggest that the filling factor is small, and it is likely that the toroidal current is filamented to scales not yet resolved. Nevertheless, macroscopically, the magnetic connection is relatively "rigid" in that bright coronal loops remain closely tied to the photospheric magnetogram features as the Sun rotates. To the extent that macroscopic quantities such as I_t and $\bar{B}_t$ are used, the filling factor does not affect Eqs. (15) and (21).

2. Physical solution and predictions

It has been shown that for observed CMEs, one can find $d\Phi_p(t)/dt$ profiles that generate CME trajectories closely replicating the data.[87,94–96,220,318] In this section, we discuss EFR solutions for observed CMEs and examine the *physical predictions* of such solutions.

Consider the basic equation of motion (20). Focusing on the Lorentz force contribution and noting $\mathbf{J} \times \mathbf{B} = (c/4\pi)(\nabla \times \mathbf{B}) \times \mathbf{B}$, Eq. (20) may be formally written as

$$\frac{d^2Z}{dt^2} = \mathcal{A}\left(\mathbf{B}, \frac{d\Phi_p}{dt}, S_f, V_{SW}, B_{c0}, c_d\right), \tag{43}$$

showing that CME acceleration $\mathcal{A}$ depends on a number of physical quantities, the most important of which are listed in the parentheses. Here, $V_{SW}(Z)$ is the SW speed as seen by the CME apex at $Z(t)$, with $V_{SW}^* = V_{SW}(Z \to \infty)$. This equation shows that $\mathcal{A}$ depends on quantities that cannot be directly measured. In contrast, the left-hand side (LHS) is determined by two directly measured quantities, Z and t. Thus, the LHS is treated as a known, and the RHS—$\mathbf{B}(t), d\Phi_p(t)/dt, S_f, V_{SW}^*, c_d, \ldots$—are treated as unknowns to be calculated in terms of $Z_{data}(t_i)$, the CME position data, where t_i is the i-th observing time ($i = 1, \ldots, N$). Thus, the formal solution for $d\Phi_p(t)/dt$ takes on the form

$$\frac{d\Phi_p(t)}{dt} = \mathcal{G}_1\left[Z_{data}(t_i)|S_f, V_{SW}^*, B_{c0}, c_d, \ldots\right], \tag{44}$$

where $\mathcal{G}_1$ is a functional of the trajectory $Z_{data}(t_i)$ and depends on S_f, V_{SW}^*, c_d, …, the initial flux rope and system parameters. These quantities must be solved for *simultaneously*. Denoting the n-th unknown on the RHS as q_n, we may formally re-write Eq. (44) as

$$q_n = \mathcal{G}_n\left[Z_{data}(t_i)|q_j, j \neq n\right], \tag{45}$$

where $j, n = 1, \ldots, K$. In this notation, $q_1 = d\Phi_p(t)/dt$. We may choose $q_2 = S_f$, $q_3 = V_{SW}^*$, and so on. Solving Eq. (45) is equivalent to solving Eq. (43). The magnetic field $\mathbf{B}_{CME}(t)$ is given by the solution, $R(t)$ and $a(t)$, via Eqs. (8) and (19).

In practice, an iterative "shooting" method is used to solve Eq. (45) for an observed trajectory $Z_{data}(t_i)$. For this purpose, it is first necessary to define a measure of the "distance" in function space between the CME data $R_{data}(t_i)$ and the theoretical solution $R_{th}(t_i)$:

$$\mathcal{D} \equiv \frac{1}{T}\sum_{i=1}^{N}\frac{|Z_{data}(t_i) - Z_{th}(t_i)|}{\Delta Z_i}\delta t_i, \tag{46}$$

where ΔZ_i is the uncertainty in Z_{data} at t_i, N is the number of data points, $\delta t_i = t_{i+1} - t_i$, and $T = \sum_i \delta t_i$. Thus, $\mathcal{D}$ measures the average deviation of $Z_{th}(t_i)$ from the observed trajectory $Z_{data}(t_i)$ relative to ΔZ_i. If the deviation is equal to ΔZ_i for all i, we obtain $\mathcal{D} = 1$: a value of $\mathcal{D} < 1$ means that the solution is within the error bars on the average.

Given the data $Z_{data}(t_i)$, the shooting method solves the coupled Eqs. (20) and (21) forward for $Z_{th}(t)$ that minimizes $\mathcal{D}$. First, a trial flux rope is specified. This can be a "generic"

flux rope (e.g., $S_f = R_\odot/2$) or one based on observational estimates. In practice, a hybrid approach is used to expedite the computation: when available, S_f is estimated from the candidate source structure, and Z_0 is determined from the height data; most other parameters q_n are started from standard values such as $B_{c0} \simeq 1$–5 G (the lower the initial height, the stronger B_{c0}), $V^*_{SW} = 400$ km s^{-1}, and $R_0/a_0 = 2$. Once a flux rope is initialized, $d\Phi_p(t)/dt$ is adjusted until $\mathcal{D}$ is minimized for the given initial flux rope. Next, a flux rope is chosen with a different S_f, and a new $d\Phi_p(t)/dt$ is obtained. The process is repeated until the value of S_f is found that minimizes $\mathcal{D}$. At this point, q_1 and q_2 in Eq. (45) have been tentatively determined. This is iterated for all q_n, and the overall minimum-$\mathcal{D}$ solution $Z_{th}(t)$ is accepted as the *physical* solution for the input trajectory $Z_{data}(t_i)$. The quantities $d\Phi_p/dt$, S_f, V^*_{SW}, $\cdots$ are now the predictions of the EFR model. The results show that the converged solutions are insensitive to the initial trial flux ropes.

The observed spatial quantity is *elongation*, which is the angular distance from the Sun. Elongation ϵ of an observed feature is related to the "true" distance $\mathcal{R}$ from Sun center by

$$\mathcal{R} = R_{Obs}\frac{\sin\epsilon}{\sin(\epsilon+\mu)}, \quad \mu \equiv \cos^{-1}(\cos\phi\cos\theta), \tag{47}$$

where R_{Obs} is the distance of the observer from Sun center and $\mathcal{R}$ is $\mathcal{R} = Z + R_\odot$, so that $\Delta\mathcal{R} = \Delta Z$. For an observer at 1 AU, $R_{Obs} = 215R_\odot$. Here, ϕ and θ are the longitude and latitude of the source location, and the feature is assumed to be moving along the radial line emanating from ϕ and θ. The solar disk center is $\phi = 0$ and $\theta = 0$. The location of the source structure is usually inferred using EUV or Hα. With this observational input, the "true" (de-projected) distance of the observed (projected) LE position is calculated. In tracking the apex, Eq. (47) assumes that it is a localized "object." There is a certain amount of uncertainty in relating the observed CME—a density feature—to the unobservable magnetic structure. This is reflected in $\Delta Z_i = \Delta\mathcal{R}_i$.

Of the EFR predictions, certain quantities can be tested with existing data: (1) the temporal profile of $d\Phi_p(t)/dt$ versus that of $\mathcal{I}_{SXR}(t)$, (2) calculated S_f versus the observed pre-eruption footpoints, and (3) magnetic field and plasma parameters of the model CME at 1 AU versus *in situ* data for MCs (e.g., $\mathbf{B}_{1AU}$, $\bar{n}_{1AU}$, and $\bar{T}_{1AU}$). Some quantities such as the value of $d\Phi_p(t)/dt$ and $V_{SW}(\mathcal{R})$ encountered by a CME have not been measured.

3. Dynamics and evolution of CME magnetic field to 1 AU

Let us examine a CME that was continuously tracked by STEREO from the Sun to 1 AU where the ejecta properties were measured. For this event, the observed CME trajectory and *in situ* ejecta data can be used to test calculated theoretical results. On 2007 December 24, the COR1-A coronagraph detected a CME, which was observed to propagate through the FOVs of COR1, COR2, HI1, and HI2 on STEREO-A, providing well-resolved position-time data to 1 AU. The CME was also observed by COR2-B (on STEREO-B). Figure 34 shows the alignment of the two STEREO spacecraft, separated by approximately 44°. In the COR2-B FOV, the CME appeared as a halo around the Sun with slight asymmetry. Based on this asymmetry, the CME apex was estimated to expand in the direction at ~40° E from STEREO-A, nearly toward STEREO-B. This trajectory is indicated (dashed arrow marked "CME") in Fig. 34.

In the STEREO-A images, the CME exhibited a typical flux-rope morphology (e.g., Fig. 24), with the inferred toroidal axis slightly inclined above the ecliptic plane. The inferred 3-D magnetic geometry is shown in Fig. 35. Figure 36 shows the position-time data of the LE (symbols). Shortly (~6 h) after the observed LE of the CME overlapped the projected position of STEREO-B in the HI2-A FOV, the IMPACT magnetometer[376] and PLASTIC plasma instruments[377] aboard STEREO-B detected the prototypical magnetic and plasma signatures of MCs[27]. The observed magnetic field is plotted in Fig. 37(a). Shown here are the magnitude (red) and the components in the spacecraft R-T-N coordinates (Fig. 35). The identifying magnetic signature of MCs is the smooth rotation of the IMF over many (> 10) h, manifested in this event as more than 24 h of northward $B_N(>0)$ followed by 24 h of southward $B_N(<0)$. The quantity ϑ (black curve) measures the rotation angle as defined in Eq. (2), with the substitutions $N \leftrightarrow z$ and $T \leftrightarrow -y$. The two vertical lines indicate the maximum and minimum in ϑ, which are the LE and TE of the MC.[27] The measured plasma parameters inside the MC are $\bar{n}_{MC} = 5 \times 10\,\mathrm{cm}^{-3}$ and $\bar{T}_{MC} \approx 3 \times 10^4$ K. In the SW outside the MC, $T_{SW} \approx 6 \times 10^4$ K, where both T_{MC} and T_{SW} refer to proton temperatures. A key plasma characteristic of MCs is $T_{MC} < T_{SW}$.[27]

The EFR model was applied to this event to test the theory in the Sun-1 AU region.[33] Figure 36 shows the minimum-$\mathcal{D}$ solution (solid curve, $\mathcal{D} = 0.68$) for the observed trajectory (symbols). With $\Delta\mathcal{R}_i = 1\%$ for all i, the average deviation is $\langle\Delta\mathcal{R}\rangle\mathcal{D} = 0.68\%$. That is, the model trajectory and position-time data agree to within 1% throughout the 1-AU FOV.

The solution is used to calculate the model **B** field and plasma parameters at 1 AU for comparison with the *in situ*

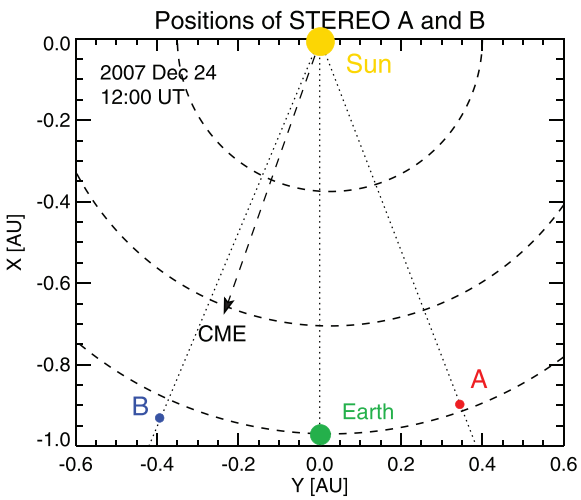

FIG. 34. Positions of STEREO A ("ahead") and STEREO B ("behind") at 12:00 UT on 24 December 2007. The dashed curves show, from inside outward from the Sun, the orbits of Mercury, Venus, and Earth, respectively.

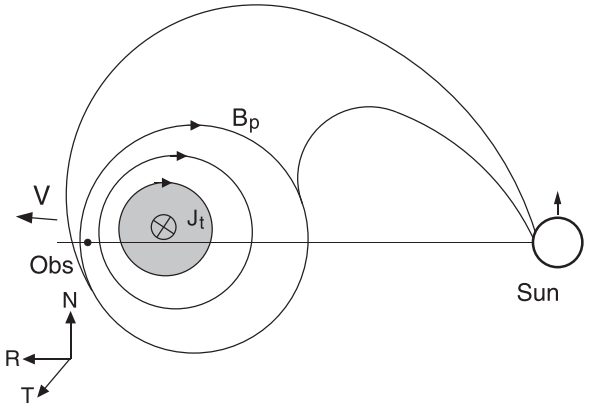

FIG. 35. Schematic of a magnetic cloud (MC) passing over STEREO B ("Obs") inferred from the source location and HI2/STEREO-A images. Only one half of the structure (into the figure) is shown. The shaded area is the current channel. The outermost magnetic surface is shown slightly past the observer in the ecliptic plane. The direction of the magnetic field is based on the polarity evidenced by photospheric magnetograms. The centroid of the apex is slightly above the observer in the ecliptic plane. The spacecraft coordinates R, T, and N are indicated. From Ref. 33.

STEREO-B data. Figure 37(b) shows $\mathbf{B}_{th}(t)$ inside the model MCs. The actual flux-rope orientation and therefore the components cannot be determined unambiguously. In this plot, the axis of the flux rope is taken to be at 55°, to roughly match the duration of the observed MC field. This is nearly equal to the angle independently calculated from the IMF data.[378] The maximum magnitude B_{CME}, in contrast, is independent of the flux-rope orientation and can be directly compared to the data: the predicted value $B_{CME} = 11.8$ nT is nearly equal to the measured value of 12.0 nT. Additionally, the rotation angle ϑ (black solid curve) of the model field along the assumed spacecraft path is similar to that of the measured magnetic field. Thus, the relationship between B_T and B_N in the calculated flux rope is consistent with that in the observed MC. For example, B_T is greater than B_R in the observed as well as model MC fields. For both the model and observed MC, the B_T and B_R components essentially vanish where the B_N component peaks.

The calculated plasma parameters are $\bar{T} = 4 \times 10^4$ K, $T_{SW} = 7 \times 10^4$ K, and $\bar{n}_p = 5\,\mathrm{cm}^{-3}$, in good agreement with the *in situ* values (above). In the EFR theory, the characteristic lower temperature in MCs arises from the adiabatic

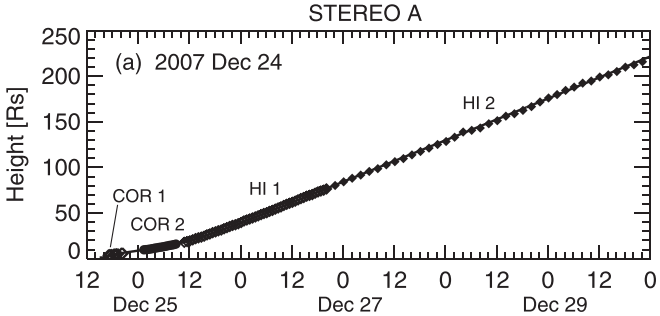

FIG. 36. CME of 2007 December 24. SECCHI-A position-time data for the CME LE (diamonds and circles). Solid curve is the best-fit initial-value solution of the EFR theory, which has $\mathcal{D} = 0.68$ [Eq. (46)], corresponding to 0.68% on the average for $\Delta\mathcal{R}_i = 1\%$. From Ref. 33.

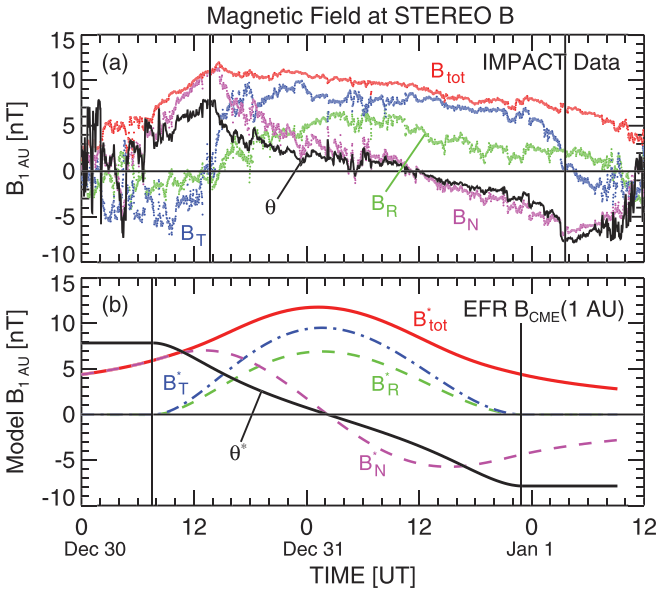

FIG. 37. Comparison of *in situ* magnetic field at 1 AU and best-fit CME ejecta magnetic field. (a) IMPACT/*STEREO-B* data (3-min average) in the R-T-N coordinates. B_R (green), B_T (blue), and B_N (magenta). $\vartheta = \sin^{-1}(B_N/B)$ is the rotation angle, scaled (×5) to better fit the plot. The vertical lines designate the LE and TE of the MC,[27] which is the current channel ($r < a$). The observed maximum field is $B_{tot} = 12.0$ nT. (b) Field $\mathbf{B}^*$ of the model ejecta at 1 AU, intersected by the observer at 55°. $B_N = B_p$ extends to $r = 2a$. No ambient IMF is included. Solid red curve: B^*_{tot} with $B_{max} = 11.8$ nT. Solid black curve: $\vartheta^*(t)$ (scaled). The assumed geometry is given in Fig. 35 except that the toroidal axis is taken to be in the ecliptic. See Ref. 33 for a discussion of this event.

expansion with $\gamma \simeq 1.2$. Additional ejecta parameters are shown in Table II.

The agreement between the calculated magnetic field and the measured MC field is significant: the input for the model—the position-time data—contains no magnetic field information. Evidently, the equations of motion correctly capture the relationship between the CME expansion and the evolution of the ejecta magnetic field.

The dependence of the CME magnetic field at 1 AU on input solar parameters has been investigated.[331] It was found that given the same initial flux rope, $B_{CME}(1\,\mathrm{AU})$ is sensitive to the total poloidal energy injected, $\Delta U_p|_{inj}(t \to \infty)$, not the functional form of $d\Phi_p(t)/dt$. Throughout this ideal MHD process, the magnetic flux is conserved except for the injected amount. Energetically, poloidal magnetic energy is converted to the kinetic energy and gravitational potential energy of the flux rope. Furthermore, the energy and momentum are coupled to the ambient medium via the drag term. By virtue of doing work against tension ($\mathbf{V} \cdot \mathbf{F}_{tens}$), poloidal energy is also converted to toroidal energy.

The synthetic field is calculated along a path through the center of the apex, but the actual centroid of the CME appeared to have been slightly above STEREO-B (Fig. 35). The difference in $|\mathbf{B}|$ is expected to be small because the gradient in B at $r = 0$ is small [Fig. 37(b)], but the "true" maximum value of $|\mathbf{B}_{CME}|$ was likely somewhat greater. The LE of the model CME overlapped the projected position of STEREO-B approximately 6 h before the commencement of the actual MC passage at the spacecraft. This is consistent

TABLE II. Predicted quantities of minimum-$\mathcal{D}$ solutions for 2008 December 24 CME.[a]

No.	$\mathcal{D}$[b]	S_f (10^5 km)	B_{c0} (G)	M_T[b] (10^{15} g)	$\bar{B}_{t0}$[b] (G)	ΔT_p (min)	$(d\Phi_p/dt)_{max}$ (10^{18} Mx/s)	V^*_{sw} (km/s)	B_{1AU}[c] (nT)	$\bar{T}_{1AU}$[c] (10^4 K)
1[d]	0.68	1.8	1.8	3.3	2.39	70	1.0	441	11.8	4.30
2	1.10	1.5	2.0	1.7	2.41	66	0.9	418	11.9	4.25
3	1.28	2.5	2.0	7.3	2.60	68	1.4	486	12.0	4.38
4	0.80	1.8	1.6	4.2	2.32	70	1.1	442	11.8	4.31
5	0.79	1.8	2.0	2.7	2.46	68	1.0	441	11.9	4.28
6[e]	0.78	1.8	2.0	3.3	2.63	64	1.1	441	12.3	4.26
7[f]	0.72	1.8	1.8	3.3	3.31	72	1.1	440	13.6	4.16
8[g]	0.71	1.8	1.8	3.3	2.39	70	1.0	442	12.6	6.52

[a]Solution 1 is the overall minimum-$\mathcal{D}$ solution. All solutions are constrained by the CME LE trajectory data. For each solution, $d\Phi_p(t)/dt$ and V^*_{sw} are varied to minimize $\mathcal{D}$. Each initial flux rope is specified by S_f, α_0, $\chi_p \equiv \bar{p}_0/p_{c0} = 1$, $\chi_n \equiv \bar{n}_{p0}/\bar{n}_0 = 0.6$, $B_{c0} = -1$ G, and $c_d = 1$ are used for all solutions except as noted for solutions 6 and 7. The equality $B_{pa0} = \bar{B}_{t0}$ results from $\chi_p = 1$. Here, subscript "0" refers to initial quantities defined at the initial centroid position Z_0.
[b]Calculated using the equilibrium force-balance conditions.
[c]B_{1AU} is the field strength on the flux rope axis. $\bar{T}_{1AU}$ is the average temperature in the flux rope. $T_{sw} \simeq 6.8 \times 10^4$ K in the ambient SW. $T_0 = 1$ MK at the initial height Z_0.
[d]Total poloidal energy injected is $\Delta U_p = 2.0 \times 10^{31}$ erg. Use $\Delta U_p \propto (d\Phi_p/dt)^2_{max}\Delta T_p$ to scale to other solutions.
[e]$\chi_n = 1.0$.
[f]$B_{c0} = -1.5$ G.
[g]The model coronal temperature at Z_0 is set to $T_0 = 1.5 \times 10^6$ K. The initial structure is the same as for solution 1. The calculated 1 AU flux rope density is $\bar{n} = 5.7\,\mathrm{cm}^{-3}$, with $n_{sw} = 5.2\,\mathrm{cm}^{-3}$.

with the apex of the flux rope passing slightly away from STEREO-B in longitude. The synthetic field accounts for the expansion of $a(t)$ during the observation—note the slight asymmetry—but does not include possible distortion of the minor radial cross-section. Numerical MHD simulations have shown that the flux-rope interaction with the ambient medium can result in such distortions.[37,199,333] The theoretical calculation also does not include the so-called Shafranov shift,[324] which is evident in Fig. 7 of Ref. 37

4. Physical connection between CMEs and flares

The above event did not show significant flare emissions. Here, we discuss CME-flare events where the source structures can be inferred.

Physically, flux injection function $d\Phi_p(t)/dt$ corresponds to an electromotive force (emf)

$$\mathcal{E}(t) \equiv \oint \mathbf{E}\cdot d\mathbf{l} = -\frac{1}{c}\frac{d\Phi_p(t)}{dt}, \tag{48}$$

which is the total electric potential drop around a closed loop along the flux rope and a path connecting the two footpoints. The spatial distribution of $\mathcal{E}$ is not predicted by the EFR theory, but the hot and highly conducting coronal part of the flux rope cannot support a significant potential drop. Thus, the bulk of the emf drop should be in the lower atmosphere between the footpoints, where resistivity is higher. The characteristic electric field $\hat{E}$ is

$$\hat{E}(t) \equiv \frac{\mathcal{E}(t)}{S_f}, \tag{49}$$

which is typically of the order of $\hat{E} \sim 1$–$10\,\mathrm{V\,cm}^{-1}$ along a distance of the order of $S_f \sim 10^5$ km, a highly super-Dreicer field of the same temporal profile as $d\Phi_p(t)/dt$. Table II shows that for the event of 2008 December 24, $(d\Phi_p/dt)_{mx} \sim 10^{18}$ Mx s^{-1}, which is $\mathcal{E} \approx 10^{10}$ V across $S_f \simeq 1.8 \times 10^5$ km. The full-width-at-half-maximum (FWHM) duration for $\mathcal{E}(t)$ is $\Delta T_p \simeq 70$ min. There is an emf-induced electric current between the two footpoints, but it has not been treated. This current is distinct from and opposite to the "image" current.[266,289]

The EFR theory does not treat particle acceleration and radiation mechanisms. Nevertheless, one can conclude that if the emf accelerates charged particles that subsequently radiate, the calculated temporal profile of $\mathcal{E}(t)$—a prediction of the theory—should be closely correlated with that of the associated SXR light curve $\mathcal{I}_{SXR}(t)$ regardless of the acceleration mechanism, provided that the timescale of acceleration and radiation is much shorter than $\Phi_p(t)(d\Phi_p/dt)^{-1}$. This prediction was tested using an ensemble of CMEs for which the associated SXR data were available.[209]

Shown in Fig. 38(a) are the trajectory data $\mathcal{R}_{data}(t_i)$ for a CME (symbols) observed by STEREO-A and a number of EFR solutions (curves). In this event, the EUVI/STEREO-A instrument observed a bright loop identified as the EUV counterpart of the CME. This loop (open diamonds) was quasi-stationary prior to the eruption. After the eruption, the LE was tracked by COR 1 (solid circles) and COR 2 (open diamonds). In this plot, distance is expressed in units of $R_\odot$ and is derived using Eq. (47). Panels (b) and (c) show the LE speed and acceleration, respectively, derived from the successive position data points. In panel (d), the observed GOES 1–8 Å SXR light curve $\mathcal{I}_{SXR}(t)$ is shown (dashed curve). The CME was tracked by SECCHI/STEREO-A to 1 AU and has been discussed elsewhere.[209] Here, only the data for the main acceleration phase are given.

The position uncertainties are taken to be 2% of the measured distance, i.e., $\Delta\mathcal{R}_i = 0.02\mathcal{R}_i$ for all i. The error bars are comparable to the size of the symbols in panel (a). A few representative velocity error bars are shown, propagated from

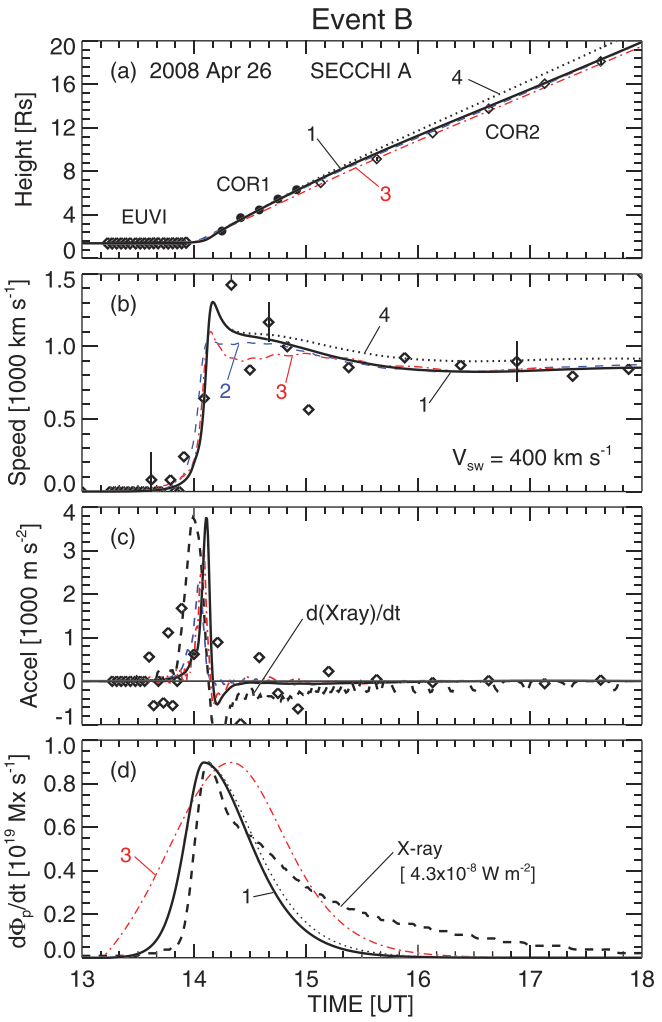

FIG. 38. Data for CME of 2008 April 26 in the inner corona and GOES SXR data, $\mathcal{I}_{SXR}(t)$. The CME was tracked to 1 AU, but only data in the inner FOV (EUVI/COR1/COR2 SECCHI-A data) are shown (symbols). In each panel, solution 1 (solid curve) is the minimum-$\mathcal{D}$ solution ($\mathcal{D} = 0.46$, $\Delta\mathcal{R}/\mathcal{R} = 0.92\%$). Solutions 2–4 correspond to different specified $d\Phi_p(t)/dt$. (a) LE trajectory. (b) LE speed. (c) LE acceleration and $d\mathcal{I}_{SXR}(t)/dt$. (d) $d\Phi_p(t)/dt$ and SXR light curve, $\mathcal{I}_{SXR}(t)$ (dashed, black). Curve 1 is well correlated with $\mathcal{I}_{SXR}(t)$ (Sec. III H 4). The time axis starts at 13:00 UT, 2008 April 26. Solutions 1–4 are tabulated and discussed in Ref. 209.

the position data. The error for acceleration is much greater and is not shown to keep the plot uncluttered. The plots show that the LE of the CME accelerated to ~1400 km s^{-1} in about 30 min, slowing down somewhat thereafter. Panel (c) shows that the main acceleration phase is sharply peaked, with the FWHM duration of approximately 10 min.

Images of the candidate source region show that a filament erupted. Using the length of the filament as a proxy for S_f, a trial value of $S_f \simeq 2 \times 10^5$ km is obtained. Using the EUVI data, the initial apex height is estimated to be $Z_0 = 2 \times 10^5$ km, and we assume $\alpha_0 = R_0/a_0 = 2$. These values are used to define the trial flux rope at $t = 0$. The shooting method yields the solution with $\mathcal{D} = 0.96$ or 1.9% of the position data ($\Delta\mathcal{R} = 2\%$). Next, S_f, Z_0, and other quantities are varied (one at a time), and the process is iterated to find the overall best-fit solution (Sec. III H 2) that minimizes $\mathcal{D}$ with respect to all the quantities. This is shown as solution 1 in Fig. 38, which has $\mathcal{D} = 0.46$, or 0.92%. This solution predicts $S_f = 2 \times 10^5$ km, $Z_0 = 1.8 \times 10^5$ km, and $\alpha_0 = 2.5$, all similar to the respective initial guesses. These quantities, including $d\Phi_p(t)/dt$, are physical predictions of the model demanded by $\mathcal{R}_{data}(t_i)$. Table III shows several solutions and various predicted quantities.

Keep in mind that given a CME trajectory, the minimum-$\mathcal{D}$ solution is unique and not dependent on initial guesses such as S_f, Z_0, and α_0. For the above event, the model predicts a value of S_f approximately equal to the observational estimate. The calculated S_f was found to be within 25%–50% of the observational proxies for the events studied.[209] This implies that the EUV and Hα images provide a good proxy for S_f. Conversely, S_f can be inferred from the observed CME trajectory.

Another quantity given by solution 1 is the driving function $d\Phi_p(t)/dt$ shown in panel (d) (solid curve designated "1"). Because the post-flare cooling processes are not included in the EFR model, the details of the decay phase are excluded, and only the rise phase and durations of the peaks in $d\Phi_p(t)/dt$ (ΔT_p) and $\mathcal{I}_{SXR}(t)$ (ΔT_{SXR}) are examined. For the GOES X-ray data, the FWHM duration is $\Delta T_{SXR} \simeq 45$ min. The FWHM duration of $d\Phi_p(t)/dt$ is $\Delta T_p \simeq 41$ min, slightly shorter than the observed duration. The characteristic maximum electric field predicted by Eq. (49) is $\hat{E}_{max} = 4.49$ V cm^{-1}, where $\mathcal{E}_{max} = 8.1 \times 10^{10}$ V. In Fig. 38(c), the time derivative $d\mathcal{I}_{SXR}(t)/dt$ of the observed GOES SXR data is shown (dashed curve, scaled to fit the plot). The temporal profile of $d\mathcal{I}_{SXR}(t)/dt$ is similar to the acceleration profile: the main acceleration phase coincides with the rise phase of the observed SXR light curve, which is shown in panel (d) (dashed curve). This is in agreement with and providing a physical explanation for the empirical findings.[219,221,222] In turn, $d\mathcal{I}_{SXR}(t)/dt$ is known to be correlated with hard X-ray (HXR).[379] The predicted $d\Phi_p(t)/dt$ for this event—extracted from the position-time data $\mathcal{R}_{data}(t_i)$—correctly captures the flare emission timescales and known temporal associations among distinct quantities.

The dependence of EFR solutions on the form of $d\Phi_p(t)/dt$ has also been investigated. Figure 38 shows a number of solutions, obtained by imposing different $d\Phi_p(t)/dt$ with all other quantities held unchanged. Here, we focus on solutions 3 and 4. Solution 3 (red, dash-dot) is given by $d\Phi_p(t)/dt$ with a much longer ramp-up time constant (τ_1) than for solution 1. The ramp-down time constant (τ_2) is unchanged at $\tau_2 = 33.3$ min. Here, τ_1 and τ_2 are defined in Appendix. Specifically, τ_1 is increased to $\tau_1 = 50$ min from the minimum-$\mathcal{D}$ value $\tau_1 = 13.6$ min (solution 1). The start time (t_1) and $d\Phi_p/dt|_{max}$ are adjusted to minimize $\mathcal{D}$, which yields $\mathcal{D} = 0.68$. This is measurably worse than solution 1, but the average deviation is still 1.4%. Overall, solution 3 yields a slower maximum expansion speed, $V_{LE} \simeq 1100$ km s^{-1} versus $V_{LE} \simeq 1300$ km s^{-1} (solution 1). After $T \sim 15{:}00$ UT, the velocity curves are virtually indistinguishable as are the height-time curves. The temporal profile of the acceleration (panel c), especially the timescale, is nearly unaffected by the significant difference in the driving term.

This can be understood as follows. Equation (31) shows that the timescale of acceleration is $\tau_R = R/V_{Aa}$, It

TABLE III. Best-fit initial flux rope parameters for 2008 April 26 CME.[a]

No.	$\mathcal{D}$	S_f (10^5 km)	Z_0 (10^5 km)	α_0	χ_p	χ_n	B_{c0} (G)	M_T (10^{15} g)	B_{pa0} (G)	B_{t0} (G)
0	0.96	2.0	2.0	2.0	1.0	1.0	–2.0	2.3	4.38	4.38
1	0.46	2.0	1.8	2.5	0.5	1.0	–2.0	1.4	4.93	5.09
2[b]	0.43	2.0	1.8	2.5	0.5	1.0	–2.0	1.4	4.93	5.09
3[c]	0.68	2.0	1.8	2.5	0.5	1.0	2.0	1.4	4.93	5.09
4[d]	2.12	2.0	1.8	2.5	0.5	1.0	2.0	1.4	4.93	5.09
5	1.13	4.0	1.8	2.5	0.5	1.0	–2.0	4.7	4.93	5.09
6	0.54	1.0	1.8	2.5	0.5	1.0	–2.0	0.9	4.93	5.09

[a]Solutions constrained by the LE trajectory of the CME of 2008 April 26. Solution 1 is the overall minimum-$\mathcal{D}$ solution.
[b]Best-fit solution with $c_d = 3$.
[c]Best-fit solution with τ_R is prescribed to be 50 min. All other initial parameters remain unchanged from solution 1.
[d]τ_2 is set to $\tau_2 = 36.3$ min, 10% greater than that for solution 1. All other parameters remain unchanged.

is determined by the initial flux rope dimension (i.e., R_0) and magnetic field (B_{pa0}), which are not affected by the different $d\Phi_p(t)/dt$. The observed acceleration timescale, therefore, provides a measure of B_{pa} and R_0 of the initial flux rope. For solution 1, Eq. (29) leads to $\bar{B}_{t0} \simeq 5.1$ G and $B_{pa0} \simeq 4.9$ G, so that on the axis of the flux rope ($r = 0$), we obtain $B_t \simeq 3\bar{B}_{t0} \simeq 15$ G and $B_p = 0$.[86,138] The main acceleration is quenched by the factor $Q_R \sim (S_f/R)^2(\ln S_f/\ln R)^2$, Eq. (37). This results from the S_f-scaling law, a purely geometrical effect, and is insensitive to the profile of $d\Phi_p(t)/dt$.

Next, the ramp-down timescale τ_2 is increased by 10% with τ_1 unchanged. The resulting solution (dotted) is designated as "4" in panels (a)–(c). This solution has $\mathcal{D} = 2.12$, which is much worse than $\mathcal{D} = 0.46$ for solution 1. The main acceleration phase is identical to that of solution 1, but the residual acceleration is slightly greater. Figure 38 shows the observed CME trajectory and model calculation to $100R_\odot$ ($\sim$1/2 AU), indicating that the solution is sensitive to how $d\Phi_p(t)/dt$ decreases. Even though the injection of poloidal flux is brief relative to the entire trajectory and the main acceleration is strongly quenched by Q_R, the difference during the residual acceleration phase is cumulative. Thus, the long-time CME trajectory is a strong constraint on τ_2 and the duration of flux injection ΔT_p.

The above analysis was repeated for four other events including short- and long-duration flares, showing similarly close agreement between the temporal profiles of $d\Phi_p(t)/dt$ and observed $\mathcal{I}_{SXR}(t)$, specifically $\Delta T_p \sim \Delta T_{SXR}$. Evidently, the EFR theory can extract the CME acceleration timescale τ_R and the temporal profile of $\mathcal{I}_{SXR}(t)$ from $\mathcal{R}_{data}(t_i)$. In particular, the rise phase of $\mathcal{I}_{SXR}(t)$ is correctly inferred. This supports the hypothesis that the emf $\mathcal{E}(t) \propto d\Phi_p(t)/dt \neq 0$ accelerates particles responsible for the associated solar flare emissions. In this process, particle acceleration results from DC electric fields, rather than waves, providing a theoretical basis for DC acceleration models.[380–382]

In the "standard model," the reconnection electric field leads to particle acceleration. As the arcade top reconnection progresses upward [top, Fig. 16(c)], the accelerated particles are mapped along the reconnected flux surfaces to the chromosphere, where they heat the plasma to form the two ribbons ["flare ribbons," Fig. 16(c)]. As successive flux surfaces are reconnected outward (Fig. 18), the bright Hα ribbons "move" outward. Accordingly, mapping the observed flare ribbons onto magnetograms [Figs. 9 and 13(b)] and assuming that all the LOS flux "swept up" by the ribbons represent reconnected flux, the reconnection electric field has been inferred.[383,384] Interestingly, such estimates—in the range of 0.2–5 V cm^{-1} (Ref. 383)—are not dissimilar to those derived from $d\Phi_p/dt$ ($\sim$2–8 V cm^{-1}, see above).[209] The reconnection electric field has also been evaluated for flare emissions using a 2.5-D resistive MHD simulation[248] with a model current-dependent resistivity, yielding $\sim$10 V cm^{-1}. Specified resistivity has also been used to model energy release in flares.[385]

The emf $\mathcal{E}(t)$ cannot be directly measured, but a number of testable properties can be inferred from Eq. (30). First, $\mathcal{E} \propto M_T^{1/2}$ because Φ_p scales with $M_T^{1/2}$. Second, CME structures with longer S_f afford longer distances over which runaway particles can be accelerated. Thus, the maximum particle energy gained scales with $M_T^{1/2}$ and S_f. The radiated power scales with the number of particles accelerated by $\mathcal{E}(t)$. Although fast CMEs are often expected to be correlated with powerful flares, these properties show that flare power has no explicit or simple relationship to CME speeds.

IV. MODELS OF SOLAR ERUPTIONS: OPEN QUESTIONS

A. EFR and CSHKP: Observational discriminators

Largely thanks to the observations of CME dynamics with wide FOVs (e.g., SOHO and STEREO), several new tenets of CME physics have been established. Notably, the hypothesis of flux-rope CMEs and the attendant hoop force as the driving force have been validated by the observed morphology and dynamics of CMEs; the predicted flux-rope expansion from the Sun to 1 AU and the evolved magnetic field at 1 AU determined by the hoop force show quantitative agreement with both remote-sensing and *in situ* data. That is, observed CMEs do behave like erupting flux ropes in the 1-AU region around the Sun.

The presence of the predicted S_f-scaling law in the observed CME acceleration data (Fig. 32) constitutes direct evidence that CMEs are flux ropes with stationary footpoints ($S_f = const$) prior to the main acceleration phase. Non-equilibrium initial flux ropes with stationary footpoints[199,291]

should also manifest the S_f scaling (e.g., point S in Fig. 32). In the CSHKP models, footpoints evolve out of arcades via reconnection. Unstable flux ropes rising through the photosphere[296,297] would also have evolving footpoints. The effects of evolving footpoints on CME acceleration would depend on the timescale of their formation, but it is certain that equations of motion having no S_f scale length do not produce the S_f-scaling law.[298,311] It is an open question as to when eruptive flux ropes are formed, but observational evidence of pre-eruption cavities[97,98] and flux ropes[99] is emerging.

A novel addition to solar eruption research is the concept of poloidal flux injection $d\Phi_p(t)/dt$ as the driver. This is regarded as a controversial challenge to the CSHKP paradigm,[46,274] but in fact this quantity occurs in traditional models as well. In a recent simulation of the "breakout" model, the poloidal flux Φ_p and toroidal flux Φ_t of the newly formed flux rope were calculated as functions of time.[278] Figure 39 shows that $\Phi_p(t)$ in the simulation increases while $\Phi_t(t)$ is nearly constant, both of which are in agreement with the EFR theory. In the simulation, the profile of $d\Phi_p(t)/dt$ is determined by numerical reconnection. The plot confirms that the physical quantity—increase in $\Phi_p(t)$—is present in both models and by extension in other CSHKP models (e.g., Figs. 17 and 18).[386] To the extent a flux rope is formed, the increased hoop force I_tB_p due to the increase in $\Phi_p(t)$ will accelerate the flux rope according to Eqs. (20) and (21). The simulated acceleration profile was not published so that its temporal relationship to the simulated $d\Phi_p(t)/dt$ cannot be determined. It is interesting to note that not only is the downward force reduced by tether cutting but also the resulting $d\Phi_p(t)/dt$ increases the hoop force. This coupling of hoop force and reconnection adds new insight to the usual notion that the repulsive force from the "image" current unbalanced by the weakened tether drives the eruption.

As for the source of $d\Phi_p(t)/dt \neq 0$, two distinct interpretations are possible: (1) the coronal arcade field (B_c) is the source of poloidal flux and is "converted" into the "private" poloidal field (B_p) of the evolving flux rope [Fig. 16(c)]; or (2) the poloidal flux is transported along the subphotospheric part of the flux-rope system and "injected" into the coronal part (Fig. 23). The traditional "standard model" demands the former and excludes the latter scenario by virtue of the photospheric (infinite conductivity) boundary condition. The EFR formulation, in contrast, does not require or preclude either scenario. Nevertheless, the main acceleration phase is largely driven by the magnetic energy in the initial flux rope in the EFR model. A CSHKP-like scenario with $d\Phi_p/dt = 0$ ("magnetic energy release") on timescales of eruption is possible.[325] Neither the subphotospheric mechanism of poloidal flux transport nor the sub-grid physics of reconnection in CSHKP simulations has been established.

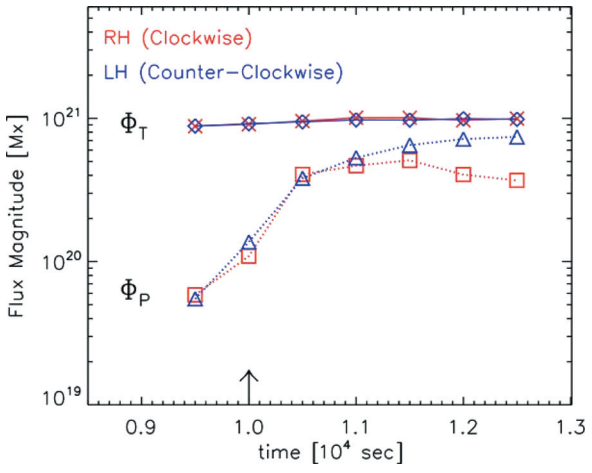

FIG. 39. Numerical calculation of the toroidal flux $\Phi_t(t)$ and poloidal flux $\Phi_p(t)$ in the "breakout" model for two scenarios. The short arrow indicates the approximate identifiable onset time of the eruptive flare reconnection. Reproduced with permission from Lynch *et al.* Astrophys. J. **697**, 1918 (2009). Copyright 2009 IOP Science.[278]

The function $\Phi_p(t)$ provides a quantifiable common point for comparison, a model discriminator between the EFR theory and arcade models. One testable prediction is the temporal relationship between the reconnected flux $d\Phi_p/dt$ and CME acceleration in arcade models. Another is the minor radial dynamics $a(t)$ in relation to $d\Phi_p(t)/dt$. In the CSHKP picture, reconnection adds new flux surfaces to the newly forming flux rope (i.e., $d\Phi_p/dt > 0$). Thus, the evolution of $a(t)$ has the ideal-MHD component, Eq. (21), plus a non-ideal correction from the addition of flux surfaces by reconnection. In Fig. 39, this occurs from $\sim 9.5 \times 10^3$ s to $\sim 1.1 \times 10^4$ s; this would be the main acceleration phase (Sec. III G 2), where the hoop force overcomes the overlying field B_c. In contrast, the ideal-MHD EFR eruption preserves magnetic surfaces, and $a(t)$ is governed by Eq. (21), with the prediction that the aspect ratio $\Lambda(t)$, Eq. (7), increases during the main acceleration phase (Appendix). This has been seen in CME data [Fig. 29(b)] and a number of observed events.[96,220] The counterpart of $\Lambda(t)$ in CSHKP models (e.g., Figs. 18 and 19) has not been investigated.

To date, observed aspect ratios have not pointed to a need to introduce a non-ideal MHD correction to Eq. (21) (Appendix for more details). The evolution of $a(t)$ during the initial stages of eruption is often occulted or difficult to observe. Nevertheless, new observations of pre-eruption cavities are emerging[97,98] and may in the future shed light on the earliest phase of the acceleration.

B. Interplanetary CME dynamics

Interplanetary MC data also provide additional means to test the minor radial structure and expansion of model CMEs. Published results show that model CME flux ropes in 2.5D[37] and 3D[199] simulations as well as in the analytic EFR CME model[86,320] can reproduce the basic macroscopic properties of observed MCs at 1 AU. In Ref. 320, the response of the magnetosphere was simulated using the calculated CME ejecta to drive a SW-magnetosphere interaction model.[388] In these studies, no data for the CME dynamics between the Sun and L1 Lagrange point were available for model-data comparison. With STEREO data, the EFR model was shown to reproduce the observed trajectory of a CME from the Sun to 1 AU as well as the magnetic field of the evolved MC measured at 1 AU.[33]

In situ magnetic field data [Fig. 37(a)] generally do not allow one to determine the true minor radius of a CME flux rope expanding past a single observer because its orientation relative to the observer is not known. In contrast, minor radial expansion of a flux rope as a function of distance is independent of flux-rope orientation. There have been statistical studies of the observed size of MCs as a function of heliocentric distance ($\mathcal{R}$).[135,389,390] This information—extending to ~4 AU—can be compared with the prediction of Eqs. (20) and (21): $a(t)$ expands as $a \propto \mathcal{R}^{\iota}$ with $\iota \simeq 1$ for $\mathcal{R} \simeq 0.3$–2 AU and $\iota \simeq 0.7$ for $\mathcal{R} \simeq 2$–5 AU.[86] These values of ι are consistent with the statistical values of observed MCs.[135,389] The subtle dependence of ι on $\mathcal{R}$ is traced to the increasing importance of the pressure term $\beta_p = 8\pi(\bar{p} - p_c)/\, B_{pa}^2$ as MCs expand over distances of the order of 1 AU. To date, no comparisons of CSHKP model predictions with data have been carried out, but the ability to continuously track CMEs and measured the ejecta quantities at 1 AU provides a challenging framework for CME-MC model validation.

As noted earlier, force-free ($\mathbf{J} \times \mathbf{B} = 0$) flux ropes have been used to model solar and interplanetary flux ropes[133,134,256] and the minor radial expansion of CMEs,[136] but non-force-free flux ropes have also been considered.[139] A flux rope that is force-free at one instant of time need not remain force-free. The minor radial dynamics in EFR, determined by Eq. (21) with $\beta_p \neq 0$, is non-force-free. The aspect ratio $\Lambda(t)$, a measurable manifestation of $a(t)$ relative to $R(t)$ that can be predicted by different models (e.g., Refs. 37, 199, 249, 274, 276, 278, and 387), may serve as a model discriminator. The force-free simplification is usually justified by the argument that the plasma β so small that pressure can be neglected. An equilibrium flux rope in an unconfined medium, however, requires the ambient pressure to balance the Lorentz force so that it cannot be force-free everywhere.[138]

C. Poloidal flux injection: Photospheric signatures

Carrington perceived the flare brightening and its apparent motion to be so akin to a "sudden conflagration" that he expected to find noticeable large-scale changes in the photosphere.[1] Comparing the sunspot sketches drawn before and after the flare, Carrington was unable to discern "any change whatever," concluding that the brightening was the release of energy stored in the corona above the sunspots. The form of this energy was not identified, but after the discovery of magnetic fields in sunspots,[148] magnetic energy in the corona became the leading candidate, giving rise to the seminal idea of magnetic reconnection as a means to release the stored energy.[253] Ever since, this paradigm of coronal energy storage and release via reconnection has guided the models and interpretations of energetic solar phenomena.

Subsequent to Carrington, photospheric changes that may indicate the emergence of energy from below to power flares—some "unusual" and "rapid" changes—have been sought with largely negative conclusions.[391–393] Such studies found changes in magnetograms, but they were judged to be transient and "evolutionary" (i.e., "usual" and "slow"). This interpretation is based on intuitive expectations rather than comparisons with signatures predicted by physical mechanisms: the question of what to look for and on what spatio-temporal scales was not addressed. Nevertheless, the adage that the photospheric magnetic field does not change before, during, or after flares became the accepted assumption of flare models, a legacy of Carrington's notion.

Later observations have found systematic changes associated with eruptions,[394–399] and Sudol and Harvey[399] have suggested that the long-held adage should be re-examined. The physical processes implied by such changes are now a matter of new research.[304,305] Separately, a number of studies have examined the magnetic helicity budget in connection with CMEs.[400–402] In these studies, the LOS magnetograms of CME source regions were used to deduce the horizontal velocity of magnetic footpoints and estimate the flux of magnetic helicity $K \equiv \int_V \mathbf{A} \cdot \mathbf{B} d^3\mathbf{x}$ into the corona. They concluded that the observed photospheric motion is insufficient to account for the estimated helicity or energy ejected by the CMEs. They suggested that injection of sub-photospheric twisting of field lines, i.e., poloidal flux injection in the language of the EFR theory, is needed. Here, for the flux rope topology, $K \sim \Phi_p \Phi_t$ so that $\Delta K = \Delta \int \mathbf{A} \cdot \mathbf{B} d^3\mathbf{x} \sim (d\Phi_p/dt)\Phi_t \Delta t$, where $\Phi_t = const$ (Sec. III F 2). The field lines penetrate the photosphere so that the relative helicity must be used to obtain gauge-invariant estimates. Helicity injection necessarily implies flux injection, but the converse is not implied.

A caveat is that the helicity inferred from photospheric data cannot be unambiguously related to the energy of a specific coronal structure without additional knowledge because the energy $U_p = \Phi_p^2/2c^2L \propto K^2/(a^4\bar{B}_t^2 L)$ depends on L and $\Phi_t = \pi a^2 \bar{B}_t$ of the structure into which helicity is injected. A similar caveat applies to poloidal flux injection because $U_p \propto \Phi_p^2/L$.

Coronal storage of magnetic energy lends itself to a conceptually pleasing and mathematically tractable formulation of solar eruptions in the half space $z \geq 0$: specify the normal component of the magnetic field $B_n(x, y)$ and the flow field $\mathbf{v}_\perp(x, y, t)$, treating the photosphere ($z = 0$) as an infinitely conducting and infinitely (i.e., non-reactive) massive surface.[243] This formulation decouples the corona from subphotospheric magnetic fields on the dynamical timescales. The focus of all models within the CSHKP paradigm is to find a form of $B_n(x, y)$ and $\mathbf{v}_\perp(x, y, t)$ that can quasi-statically build up and then eruptively release the stored magnetic energy.

Against this historical legacy, the fact that the EFR model allows the injected flux ($d\Phi_p/dt \neq 0$) to be of subphotospheric origin became controversial among coronal MHD modelers.[41,42,274] The argument is that if the energy of eruption of 10^{30}–10^{32} ergs is injected through the photosphere to drive a CME, it *must* significantly disturb the massive photosphere regardless of mechanisms. This argument has been quantified by Forbes,[403,404] shown in full in Fig. 40. Consider a patch of purely horizontal magnetic field B_h in area A in the photosphere. The Poynting vector is $\mathbf{S} = (c/4\pi)\mathbf{E} \times \mathbf{B}$. Using $\mathbf{E} + (1/c)\mathbf{V} \times \mathbf{B} = 0$, one obtains $S_z = (1/4\pi)V_z B_h^2$, where $B_h \equiv |\mathbf{B}|$ and z is the vertical direction. If this Poynting flux persists for Δt, the total magnetic energy through A is $W_B = S_z A \Delta t$. For given W_B,

$$V_z = (4\pi)W_B/(B_h^2 A\Delta t). \quad (50)$$

Thus, the injected poloidal energy can be directly measured as Doppler shift because V_z is fully coupled to B^2. Using $W_B = 10^{32}$ ergs (a large flare), $A = 10^{10}$ km^2, $B_h = 100$ G ($\beta \gg 1$), and $\Delta t = 10^3$ s, Eq. (50) yields $V_z = 12.5$ km s^{-1}. No such horizontal magnetic field or coherent plasma motion at this speed in contiguous patches of this size is observed, and Forbes argued that poloidal flux injection mechanisms could be ruled out. This conclusion is predicated on the assumption that the specified configuration is the necessary consequence of poloidal flux injection.

A similar calculation for a cylindrical flux rope was performed using a longer time period $\Delta t \sim 10^4$ s but a smaller area $A \sim 10^8$ km^2.[405–407] This work also assumed $B_z = 0$, yielding $V_z \propto (B_p^2 A\Delta t)^{-1}$, where B_p is purely horizontal. This is, not surprisingly, essentially the same as Eq. (50). The paper argued that the poloidal flux injection hypothesis of the EFR theory is "falsified." It is a mathematically complex argument, but this "complexity" is reducible, revealing basically the same calculation as Ref. 403: start with a specified monolithic patch of poloidal field ($B_z = 0$) and calculate the vertical Poynting flux S_z, leading to Eq. (50) with a different constant factor. This work developed the "optimal velocity" method to account for non-vertical plasma motion. Here, "optimal" refers to minimization of Lagrangians of the form $\mathcal{I}_i = \int_0^{r_c} r v_i^2 dr$, subject to some *ad hoc* constraints on v_i, the fluid velocity in the i-th direction; $\mathcal{I}_i$ contain no force or injected magnetic energy.

The Forbes-Schuck argument asserts that regardless of the mechanism, poloidal magnetic flux transported through the surface necessarily appears as large patches of horizontal magnetic field. Yet, this configuration is not known to occur in any flux emergence or injection process. No physical or logical relevance to flux injection is demonstrated.

Forbes (2001)

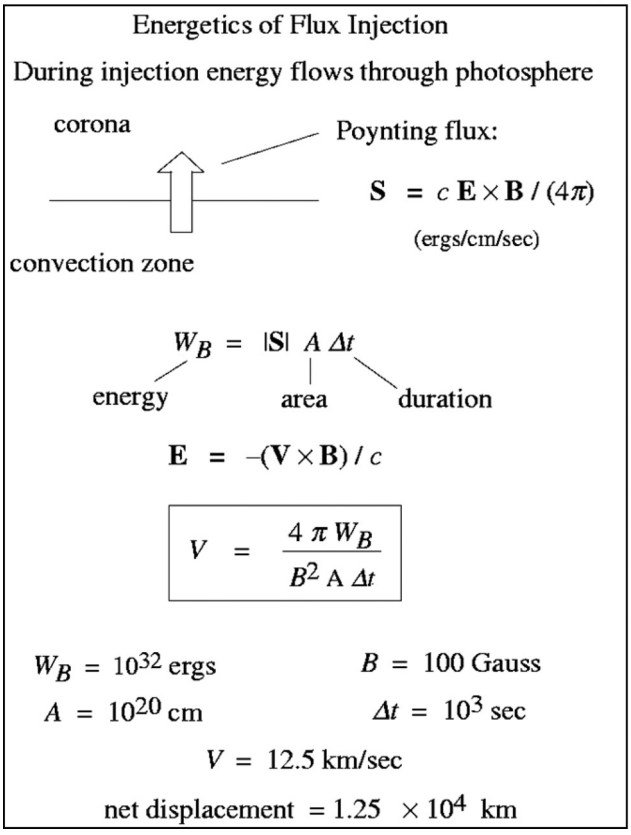

FIG. 40. Analysis of the energetics of flux injection. A viewgraph page from the talk given by T. G. Forbes at the American Geophysical Union Spring Meeting (2001) at the invitation of Chen. Courtesy of T. G. Forbes.

D. Photospheric magnetic fields

The above discussion shows that understanding the plasma dynamics of magnetic energy transport across the photosphere is essential for clarifying the energy budget in eruptions. The long-standing adage of coronal energy storage is based on the legacy built on early observations with low spatiotemporal resolution.[391–393] New observations show that magnetic fields in the solar photosphere occur on small spatiotemporal scales.[151,165,167–169]

It is instructive to examine the observed features of known flux emergence/injection phenomena. The most prominent of such processes is the emergence of new sunspots in the photosphere: an active region ($\ell \sim 10^4$–10^5 km) first appears as a pair of sunspots having strong magnetic fields of opposite polarity. The sunspots gradually separate—as would the footpoints of a rising flux—over a few days. Until recently, magnetograms showed little magnetic activities between the emerging sunspots save an occasional small bipolar element. This led to the common notion that magnetic energy of the order of 10^{33} ergs *requires* days to emerge and is not observable in the photosphere.[391–393] Recent observations by the Swedish Vacuum Solar Telescope with much higher resolution (0.29″ ~210 km), however, show small-scale features that are interpreted as "serpentine" field lines.[283,284] Sunspots themselves, the largest and most strongly magnetized structures in the photosphere, appear to be highly filamented (Fig. 8). The *Hinode* SOT/SP magnetograph (~200 km resolution) observed an emerging sunspot event and captured the appearance of a sea of small bipolar features. This process has been studied using a radiative MHD simulation of an emerging flux rope. Figure 41(a) shows the flux rope magnetic field with the footpoints at the lower simulation boundary indicated by converging field lines. Figure 41(b) is a synthetic magnetogram for this field in the photospheric surface, where the field of the well-organized flux rope appears as small bipoles (white +, black −), interpreted as the footpoints of undular field "lines." This is shown in Fig. 42. These bipoles may be the previously unobservable footpoints of filamentary loops in AFSs,[204] which appear in tens of minutes to a few hours.[43,202,203] This indicates that the timescale of flux emergence is hours, not days.

The serpentine field in the simulation appears to result from the interaction with the convective flows (Fig. 42) at the granular cell size of 1000 km in the surface, but the fact that the bipoles occur on scales of 200 km or below implies that additional processes such as plasma instabilities[412] are at work. More generally, magnetic fields in the photosphere—measured as net flux per pixel—show scale

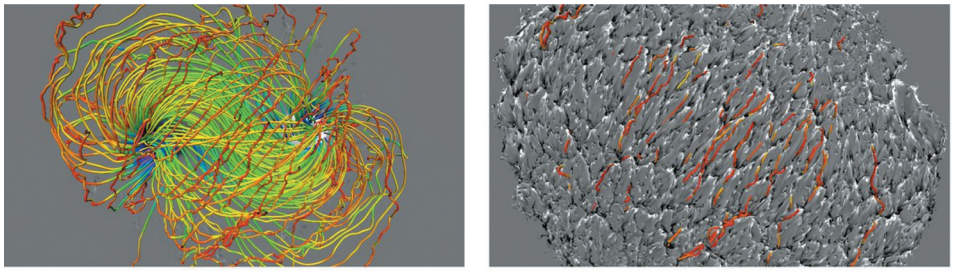

(a) (b)

FIG. 41. Magnetic field of an emerging flux rope in a radiative MHD simulation. (a) The feet of the flux rope, located at the lower simulation boundary ($z = -7.5 \times 10^3$ km) with minor radius $a = 3.6 \times 10^3$ km, are indicated by the converging field lines. (b) Synthetic LOS magnetogram of the flux-rope field in the photosphere ($z = 0$). Well-organized magnetic field of an emerging flux rope appears as a sea of bipoles—white (+) and black (–)—that are the footpoints of undular ("serpentine") field lines. They are much smaller than the dimension of the underlying magnetic structure and result from the interaction between the rising field and granular convection flows in the simulation. In the Sun, various instabilities can also play a role as a flux rope rises from a much deeper source. From Ref. 192.

invariance down to the limit of resolution under both quiet and active conditions.[167–169,283,413] That even strong photospheric magnetic fields occur on small scales is consistent with the small natural scales of plasmas (Table I). Large patches of horizontal magnetic field are not consistent with these observations or the known physical processes in the Sun.

As for the Poynting flux associated with the serpentine field, Fig. 42 shows that V_z in Eq. (50) may apply to the apex of each ∩-shaped loop where S_z is coupled to V_z but that such features are much smaller than the patch dimensions of 10^4–10^5 km assumed in Refs. 403 and 405. On this scale, a significant amount of poloidal energy emerges as B_z^2, which is not measurable as the Doppler motion V_z and cannot be accounted for by Eq. (50).

For the 3-D dynamics involved in poloidal flux injection through the photosphere, it is important to account for the azimuthal electric field E_θ at the flux rope footpoints

$$\frac{\partial E_\theta}{\partial z} = \frac{1}{c}\frac{\partial B_r}{\partial t},$$
$$\frac{1}{r}\frac{\partial}{\partial r}(rE_\theta) = -\frac{1}{c}\frac{\partial B_z}{\partial t}, \tag{51}$$

where the legs of the flux rope in the photosphere are assumed to be vertical and the standard cylindrical coordinates are used with $\partial/\partial\theta = 0$. This field has a component E_p along the wavy B_p lines illustrated in Fig. 23. By Ohm's law, an electric current $J_p = \sigma E_p$ is produced, where σ is the plasma conductivity. This implies that the serpentine "rods" shown in Fig. 42 are small-scale current filaments (thin flux ropes), which have their own poloidal fields in the photosphere, replicating this structure on the scale of filamentary serpentine lines. The small plasma scale lengths suggest that this process can cascade down to much smaller sizes, consistent with the scale invariance suggested by observations.[167,169] As for the increasing J_p in the vertical sections of serpentine structures, this corresponds to a Poynting flux in the minor radial (horizontal) direction converging toward the current on all scales. This means $S_h \neq 0$, which is *a priori* neglected in Eq. (50).

Another important point is that the undular B_p field lines can reconnect and shed the heavy plasma tied to the field lines,[192,406] illustrated in 3-D by Fig. 42. In this regard, the so-called Parker instability[407] plays an essential role, where the plasma on a magnetic field line is stratified with higher density at the bottom of a U-shaped field line. The reconnected B_p field would form the poloidal field around the flux

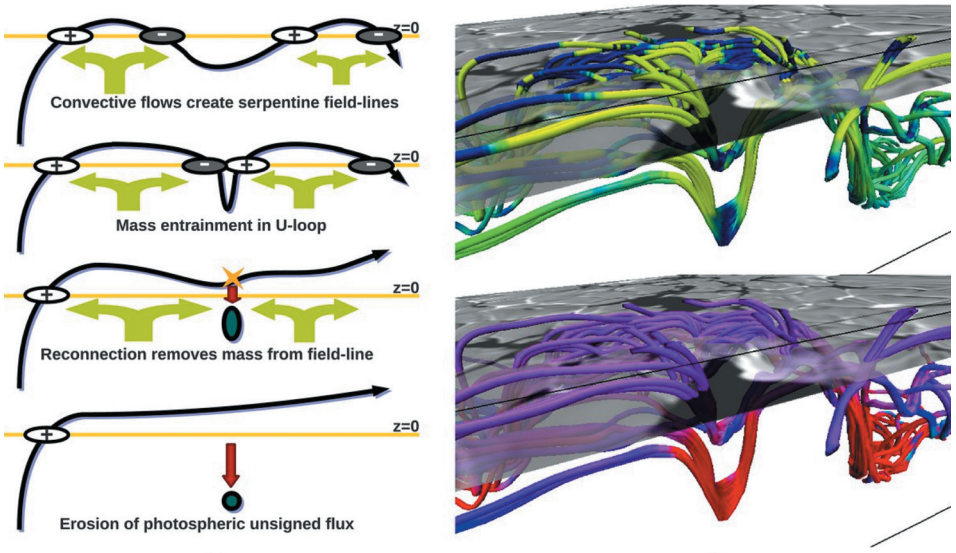

(a) (b)

FIG. 42. Shedding of subphotospheric mass from rising undular field lines due to local reconnection. Reproduced with permission from Cheung *et al.*, Astrophys. J. **720**, 233 (2010). Copyright 2010 IOP Science.[192] (a) Cartoon of how mass is removed from emerging magnetic field lines. The serpentine field is attributed to the convective granular upflows. (b) 3-D depiction of the simulated emerging magnetic elements. Upper panel: density perturbations along field lines (darker is denser). Lower panel: z component of the fluid flow momentum (red is downflow).

rope in the corona (Fig. 23). These dynamical processes are excluded in monolithic patches of horizontal fields. Note that the Parker instability has been seen in numerical simulations.[408,409]

The above discussion identifies three major predictions for the photospheric signatures of poloidal flux injection: (1) the injected poloidal field emerges through the photosphere in the form of filamentary undular structures on small scales, (2) such serpentine field can reconnect in the photosphere and below, continually "shedding" the dense material as a magnetic structure rises, and (3) the induced current J_p due to E_θ, Eq. (51), is essential in the magnetic flux budget and its measurement. These are 3-D and dynamical effects. Low-dimensional simulations, where the dense subphotospheric plasma cannot be shed or drained, show that it is difficult, if not impossible, even for 2-D subphotospheric magnetic structures to rise to the corona.[410,411] The above predictions are potentially testable by detailed simulations of physical flux injection mechanisms.

V. SUMMARY AND REMARKS

The paper has presented a discussion of the state-of-the-art understanding of the eruptive processes from observational, theoretical, and modeling points of view. The focus has been on the physics of CMEs—their magnetic configuration, acceleration mechanism and forces, and their physical relationships with the major manifestations of eruption: EPs, flare emissions, and interplanetary MCs. The observed dynamics are consistent with the EFR theory, currently, the most extensively tested by remote solar as well as *in situ* SW data. The theory also produces the temporal profiles of associated flare SXR emissions, tested by an ensemble of CME-flare events. This suggests a new theoretical framework to unify the CME-EP-flare-MC phenomenon. A "tutorial" on the EFR theory has been given (Secs. III F and III G). The EFR concept is contrasted with the traditional CSHKP paradigm, and model discriminators are identified. New answers to long-standing questions regarding solar eruptions and their connection to geoplasma space are emerging:

1. *CMEs are erupting magnetic flux ropes from the earliest stages observed*. A key identifier of flux-rope CMEs is the dynamics, i.e., the agreement between the observed CME-EP dynamics and the calculated dynamics of toroidal flux ropes having fixed footpoints ($S_f = const$). SOHO and STEREO observations from the Sun to 1 AU, combined with ACE data, have provided an unprecedented basis for testing model predictions. The ideal-MHD EFR theory has accurately reproduced observed CME/EP trajectories. The observed aspect ratio $\Lambda(t)$, Eq. (7), where available, is replicated by such solutions (Sec. III H 2), implying that the equations of motion captures the 3-D CME dynamics in the two coupled orthogonal directions. There is increasing observational evidence that CMEs have the flux rope topology prior to the onset.[97–99]
2. *CME flux ropes are driven by the Lorentz hoop force* ($I_t B_p$). A manifestation of this force is the predicted S_f scaling law, which has been observed in CME-EP data (Fig. 32). It is a geometrical effect that quenches the hoop force according to $Q_R \propto (S_f/R)^2$, Eq. (37). It is specific to toroidal flux ropes with stationary footpoints (Figs. 30 and 31). The length scale $S_f = const$ is essential to correctly calculate CME acceleration: models using the hoop force but without constrained footpoints do not exhibit this property.
3. *Initial flux-rope magnetic field is determined by the toroidal equilibrium*. The initial field B_{pa0} is given by Eq. (29), resulting from toroidal force balance, $d^Z/dt^2 = 0$ and $d^2a/dt^2 = 0$ at $t = 0$. This determines the timescale of the main acceleration phase, the Alfvénic time $\tau_R \propto R_0/B_{pa0}$.
4. *Pre-eruptive flux ropes are driven out of equilibrium by the Lorentz hoop force due to the increasing poloidal flux*, $\Phi_p(t)$. The source of Φ_p is not specified and has not been established: it may be of subphotospheric or coronal origin. Numerical MHD models also produce $d\Phi_p/dt \neq 0$ due to reconnection.[278] This should appear as a non-ideal MHD correction to Eq. (21), a possible model discriminator. To date, no need for such a correction has been indicated by data, but more detailed observation of the very earliest phase of acceleration is required. Unresolved issues for both scenarios have been discussed in Sec. IV.
5. *Poloidal flux injection generates an emf* $\mathcal{E}(t) = -(1/c)\, d\Phi_p(t)/dt$, *which can accelerate particles to flare energies*. The temporal profiles of $d\Phi_p(t)/dt$ predicted by EFR for observed CMEs coincides with the associated flare SXR emission profile $\mathcal{I}_{SXR}(t)$. See Fig. 38(d). For CMEs, $\mathcal{E} \sim 10^{10}$ V over 10^5 km. This supports the hypothesis that the emf $\mathcal{E}(t)$ accelerates particles producing flare emissions. The emf $\mathcal{E}$ scales with $M_T^{1/2}$ and S_f (Sec. III H 4). The ideal MHD EFR theory predicts $\mathcal{E}(t)$, but particle acceleration must be separately modeled.
6. *MCs correspond to the evolved current channels of CME flux ropes*. The STEREO spacecraft have, for the first time, continuously tracked CMEs and measured the ejecta magnetic and plasma data at 1 AU. Theoretically, the current channel of the CME flux rope evolves into an MC as the heliospheric counterpart. For a few events, the EFR solution replicates both the CME dynamics and the evolved counterpart observed at 1 AU.[33] There is evidence that MCs maintain their magnetic and thermal connection to the Sun.[35,36]
7. *The observed CME dynamics and CME-to-MC evolution can be correctly replicated by the EFR theory only if prominence mass is included in the initial equilibrium flux rope*. The cold prominence plasma is integrally coupled to the long-time CME dynamics via the gravity term $m_i \bar{n}_p \neq 0$ in Eq. (22) and determines the initial flux-rope magnetic field, which determines the Lorentz hoop force. The observed structural relationship between CMEs and associated EPs [e.g., Figs. 10(a), 24, and 27] is consistent with the flux-rope CME concept (Fig. 22). Combined with the temporal relationship $\mathcal{E}(t) \propto \mathcal{I}_{SXR}(t)$ (approximately), the EFR theory can potentially provide a unified framework to understand the integrated CME-EP-flare-MC process.

The agreement between the predicted quantities—$\mathcal{E}(t)$ and $\mathbf{B}_{th}(1\,\mathrm{AU})$—and the observed counterparts—$\mathcal{I}_{SXR}(t)$ (temporal profile) and $\mathbf{B}_{data}(1\,\mathrm{AU})$—is significant because the input to the calculation, the CME position-time data

$Z_{data}(t_i)$, contains no explicit information on magnetic field, SXR emissions, or particle acceleration. The ideal-MHD EFR equations are evidently able to extract the timescale of flare energy release and predict the evolution of CME magnetic field from $Z_{data}(t_i)$ alone (Secs. III H 2 and III H 3). This implies that the equations correctly capture the relationship between the position-time data $Z(t)$ and the magnetic field evolution; they are the "HD" and "M" of MHD, respectively.

The recent advances have not answered all questions, but a number of important issues can now be better defined (Sec. IV). A major question is the physical interpretation of an increase in the flux-rope poloidal flux, $d\Phi_p/dt > 0$, present in both the EFR and CSHKP models. The EFR theory allows (but does not require) poloidal magnetic energy injection from the convection zone, the ultimate source of all solar magnetic energy. The physical process, however, has not been modeled, and potential photospheric signatures of subphotospheric poloidal flux injection have yet to be established. The CSHKP paradigm, in contrast, places the energy of eruption to be in the corona, requiring reconnection in the corona that converts coronal flux into the poloidal flux of an evolving flux rope (Sec. IV A). The required physical mechanism in the corona has yet to be demonstrated.

It is clear that the poloidal flux injection function $d\Phi_p(t)/dt > 0$ predicted by the EFR is applicable to the CSHKP construct. While the traditional CSHKP formulation excludes the subphotospheric sources by imposing the photospheric boundary condition, there is no physical reason to do so. Indeed, new attempts to relax the constraints imposed by this traditional boundary condition and include subphotospheric magnetic structures and sources are emerging.[296,297,411] The challenge is that most of the photospheric plasma dynamics is driven by subphotospheric dynamics (e.g., Refs. 192, 193, and 408), is strongly coupled to radiation, occurs on small scales,[151,165,167,169] and requires fully 3-D simulations.

Potential model discriminators including the observed aspect ratio and certain photospheric features have been suggested, which need to be better understood with further modeling and higher-resolution observations. It is noted that the discipline of helioseismology, both local and global, has made important strides in quantifying the relationships between the unobservable magnetic field in the convection zone and observed photospheric data.[160] In the view of the present author, helioseismology will play a pivotal role in answering some of the most fundamental questions regarding solar magnetism, of which eruptions are but one manifestation. The physics of the expansion of partial flux ropes in a background plasma is generalizable to flux ropes in the solar convection zone, stellar atmospheres,[414–417] and laboratory plasma experiments.[365,418–420] Well-constructed and scalable experiments can potentially simulate specific assumptions and processes embodied in theories and numerical models of solar eruptions.

ACKNOWLEDGMENTS

I wish to express my gratitude to Dr. Valbona Kunkel of George Mason University, my former Ph.D. student, and Dr. Russell Howard of the Space Science Division (SSD), Naval Research Laboratory (NRL), for numerous discussions over many years. The depth and extent of Dr. Howard's knowledge of the CME phenomenon, especially his insight dating back to the very first observation of CMEs, have been beneficial. I also wish to record my deep gratitude to the late Dr. Guenter E. Brueckner of the SSD/NRL who supported my initial effort to establish a program in solar plasma physics in the Plasma Physics Division/NRL. It is fitting that the observations by the LASCO instruments, of which Dr. Brueckner was Principal Investigator, extended the coronagraph field of view to $32R_\odot$, which played a key role in establishing the then-controversial flux-rope CME paradigm. I also wish to thank two anonymous referees who provided numerous comments from the traditional point of view during several iterations, leading to more extensive discussions of differences between the new theory and the prevailing models in Sec. IV. The work was supported by the Naval Research Laboratory Base Research Program.

APPENDIX: POLOIDAL FLUX INJECTION FUNCTION

The quantity $d\Phi_p(t)/dt$ is a mathematical function that enters the EFR theory as the driving function: when it is increased from zero, the flux rope is set into motion. It represents a packet of poloidal flux injected into the existing flux rope. The EFR model uses a simple generic pulse in terms of a number of parameters as follows:

$$\frac{d\Phi_p(t)}{dt} = \begin{cases} q_0 & 0 \le t \le t_1, \\ q_0 + q_1\left\{\operatorname{sech}^2\left[(t_2 - t)/\tau_1\right] - \operatorname{sech}^2\left[(t_2 - t_1)/\tau_1\right]\right\}, & t_1 < t < t_2, \\ q_0 + q_1\left\{1 - \operatorname{sech}^2\left[(t_2 - t_1)/\tau_1\right]\right\} \equiv \left(d\Phi_p/dt\right)_{max}, & t_2 \le t \le t_3, \\ \left(d\Phi_p/dt\right)_{max}\operatorname{sech}^2\left[(t - t_3)/\tau_2\right], & t_3 < t, \end{cases} \tag{A1}$$

where q_0 and q_1 are non-negative constants, and τ_1 (τ_2) is the ramp-up (ramp-down) timescale. the main pulse starts at $t = t_1$ and reaches maximum at $t = t_2$. The flux injection rate is constant at $(d\Phi_p/dt)_{max}$ in the time interval $[t_2, t_3]$. Thereafter, $d\Phi_p(t)/dt$ decreases and asymptotes to zero. In reality, a packet of Φ_p need not be a single-peak pulse, but a

more general profile may be represented as a superposition of multiple single-peaks.

In the CSHKP framework, the functional form of $d\Phi_p(t)/dt$ would be determined by the coronal reconnection physics on the macroscopic scales. In simulations, the time constants τ_1 and τ_2 and the magnitude of the pulse $(d\Phi_p/dt)_{max}$ are determined by grid-based numerical dissipation.

For modeling observed CME-flare events using the EFR theory, all the parameters in the above expressions are constrained by CME trajectory data $Z_{data}(t_i)$ (Sec. III H 2). No mechanisms are specified. Figure 43(a) shows two examples of $d\Phi_p(t)/dt$. For profile "1," $t_2 = t_3$ is required. This is the minimum-$\mathcal{D}$ solution with $\mathcal{D} = 0.46$ (Fig. 38). Profile 2 is obtained by imposing the constraint $t_3 - t_2 = 30$ min and minimizing $\mathcal{D}$. For this solution, $\mathcal{D} = 1.01$, and the LE speed (not shown) is similar to that of curve 3 in Fig. 38(b). The thin vertical line is where the acceleration is maximum [Fig. 38(c)]. It is typical that observed CME data result in $t_3 - t_2 \simeq 0$. It is also typical that $q_0 \simeq 0$. Some CMEs do exhibit gradual rise prior to the main acceleration, sometimes refer to as the "initiation phase."[219] In such events, the EFR equations predict a small nonzero value $q_0 \ll q_1$. Some examples are given in Ref. 209.

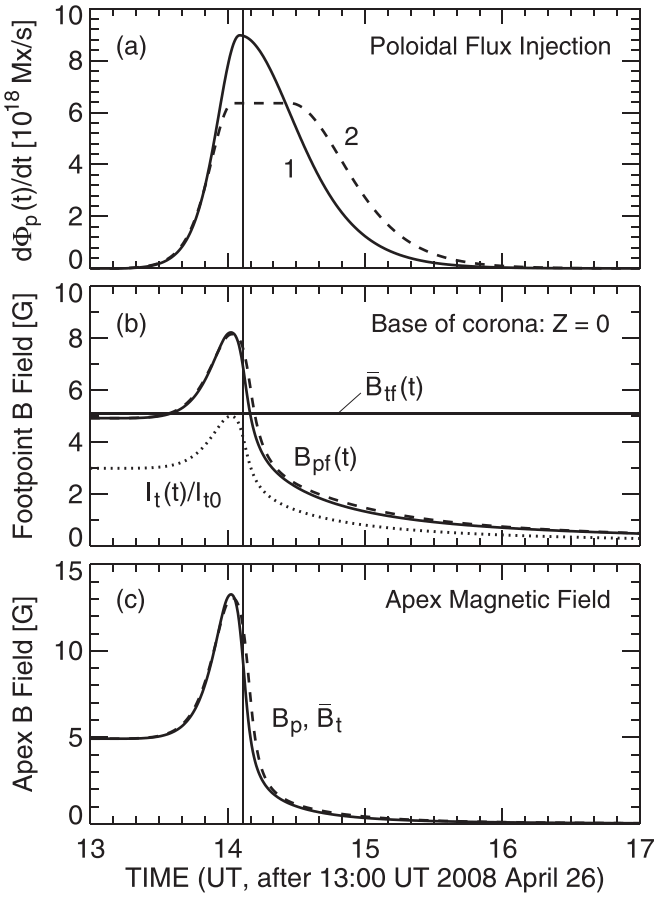

FIG. 43. Flux injection function given by Eq. (A1) and its relationship to the magnetic field. For the CME of 2008 April 24 (Fig. 38). (a) Two profiles of $d\Phi_t(t)/dt$. Solid curves: the minimum-$\mathcal{D}$ solution (solution 1), for which $\mathcal{D} = 0.46$. The EFR equations require $t_3 - t_2 = 0$ for this CME. For solution "2" (dashed curve), $d\Phi_t(t)/dt$ is required to have $t_3 - t_2 = 30$ min. $\mathcal{D}$ is minimized with this constraint. $\mathcal{D} = 1.01$ for this solution. (b) Magnetic field components at the base of the corona (footpoints), B_{pf} and $\bar{B}_{tf}$. Note that $\bar{B}_{tf} = const$. For solutions 1 (solid) and 2(dashed). The toroidal component $\bar{B}_{tf}$ remains constant while the poloidal component B_{pf} increases for about 10–20 min. $I_t(t)/I_{t0}$ is shown (dotted, arbitrary units). (c) Field components at the apex, where $B_{pa}(t) \approx \bar{B}_t(t)$.

Figure 43(b) shows the poloidal component $B_{pf} \equiv B_p(a_f)$ of the "footpoint" and the average toroidal component $\bar{B}_{tf}$ of the footpoint at the base of the corona for the two solutions. The total toroidal current $I_t(t)$ has the identical profile as $B_{pf}(t)$ and is not separately shown. It is important to note that $\bar{B}_{tf} = const$. The toroidal current $I_t(t)$ is shown, normalized to the initial value I_{t0} and scaled to fit the plot. Panel (c) shows the magnetic field components of the flux rope apex, $B_{pa} = B_p(r = a_a)$ (solid and dash-dot) and $\bar{B}_{ta}$ (dashed) for the two profiles. For this particular initial flux rope, $B_{pa}(t) \simeq \bar{B}_{ta}(t)$ for all t and are not distinguishable. ($\bar{B}_{ta}(t)$–dashed–for solution 1 is visible near $t = 13:00$ UT.)

The peaks in Figs. 43(b) and 43(c) are caused by the same process that causes the aspect ratio Λ to increase (Sec. III E 2): as $\Phi_p(t)$ increases, $I_t(t) = \Phi_p/cL(t)$ increases (panel c) as do $B_p = cI_t/ca$. At the footpoint, $a_f = const$ and therefore $B_{pf}(t) \propto I_t(t)$ and $\bar{B}_t(t) = const$. At the apex, the increased pinch force causes $a_a(t)$ to decrease slightly so that the relative increase in $B_{pa}(t) \propto I_t(t)/a_a(t)$ is greater than that in B_{pf}, as can be seen by comparing panels (b) and (c). The most important difference, however, is in $\bar{B}_t$. Because flux conservation requires $\Phi_t(t) = const$, $\bar{B}_{ta}(t) = \Phi_t/\pi a_a^2(t)$, which increases during the main acceleration phase because $a_a(t)$ decreases by the increased pinch force.

From $\Phi_p = cL(t)I_t(t)$ and $\Phi_t = \pi a^2 \bar{B}_t$, one sees that $\Gamma_a(t) \simeq const$ implies $\Phi_p(t)a_a(t)/R(t)\ln(R/a_f) \simeq const$, where constant factors have been omitted. Thus, $R(t)\ln(R/a_f)/a_a(t) \sim \Phi_p(t)$. During the main acceleration phase, and $R/a \equiv R(t)/a_a(t) \propto \Phi_p(t)/\ln(R/a_f) \neq const$.

An interesting manifestation of the last property can be seen in the following quantity,

$$\Gamma(t) = B_p(t)/\bar{B}_t(t), \tag{A2}$$

which is the characteristic pitch of the flux-rope field lines. The local magnetic field pitch angle $\eta(r,t) \equiv \tan^{-1}[\Gamma(r,t)]$ inside a flux rope is variable, ranging from $\eta = 0$ at $r = 0$ to $\eta_a = \tan^{-1}(\Gamma)$ at $r = a$. Figure 44 plots the characteristic magnetic pitch at the apex $\Gamma_a(t)$ and at the footpoint $\Gamma_f(t)$, showing that $\Gamma_f(t)$ is peaked but $\Gamma_a(t)$ is nearly constant. This means that the pitch or the "twist" of the field lines in

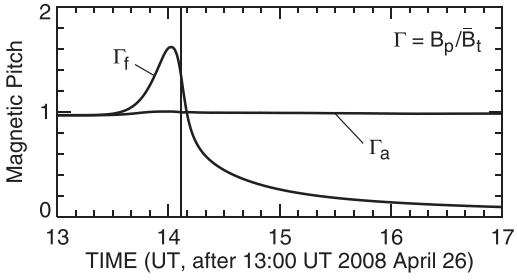

FIG. 44. Magnetic field pitch at the footpoint $\Gamma_f(t)$ and apex $\Gamma_a(t)$ for solution 1 in Fig. 43. The vertical line indicates the time of acceleration maximum. $\Gamma_a(t)$ is nearly constant. The peak in Γ_f correlated with the rising phase of $d\Phi_p(t)/dt$ (Fig. 43) and constancy of Γ_a are characteristic of flux-rope dynamics due to poloidal flux injection in the EFR theory.

the "legs" down to the footpoints of an erupting flux rope increases during the main acceleration phase, while the magnetic field pitch at and around the apex is nearly constant. The peak in $\Gamma_f(t)$ is due to the peak in B_{pf}, which arises from the peak in pinch force.

The above property is general (see Sec. II.4.4 of Ref. 86 and Sec. 6 of Ref. 220) and may be observable during the early stages of prominence eruption. Assuming that the characteristic braided features in EPs (Figs. 4, 5, and 28) represent plasmas outlining magnetic field, it has been inferred from the apparent twist that the toroidal current in the lower legs increased for 30–40 min during the early phase of an observed EP.[326] In a statistical study of EPs exhibiting apparent helical features, images of those observed at the onset of eruption and in the acceleration phase tend to show greatest twist while images of post-acceleration prominences exhibit reduced twist.[327] Where individual EPs could be followed, the twist of a prominence near the apex appeared to change only slightly. These observed properties—including the timescale—and inferences are consistent with the general behavior shown in Figs. 43 and 38 and may be evidence of the predicted magnetic field response to flux injection. Aside from the few detailed studies of EPs observed in Hα mentioned above, these properties have not received much attention.

[1]R. C. Carrington, Mon. Not. R. Astron. Soc. **20**, 13 (1859).
[2]R. Hodgson, Mon. Not. R. Astron. Soc. **20**, 16 (1860).
[3]G. E. Hale, Astron. Astrophys. **11**, 17 (1892); **11**,917 (1892).
[4]H. Deslandres, Astron. Astrophys. **11**, 502 (1892); **11**, 314 (1892).
[5]A. Boischot, C. R. Acad. Sci. Paris **244**, 1326 (1957).
[6]A. D. Fokker, Space Sci. Rev. **2**, 70 (1963).
[7]M. R. Kundu, Sol. Phys. **111**, 53 (1987).
[8]L. Viatour, www.Lucnix.be (1999).
[9]E. Pettit, Astrophys. J. **76**, 9 (1932).
[10]H. W. Dodson, Mon. Not. R. Astron. Soc. **110**, 199 (1950).
[11]H. W. Dodson and R. W. Donselman, Astrophys. J. **113**, 519 (1951).
[12]R. Tousey, in *Proceedigs of the Open Meetings of Working Groups of the 15th Plenary Meeting of the Committee on Space Research (COSPAR Space Research XIII)*, edited by M. J. Rycroft and S. K. Runcom (Pergamon, Oxford, 1973), p. 713.
[13]B. Lyot, C. R. Acad. Sci. Paris **191**, 834 (1930).
[14]B. Lyot, Mon. Not. R. Astron. Soc. **99**, 580 (1939).
[15]A description of the Soviet spacecraft Luna 1 launched in January 1959 and its discoveries can be found in NASA's National Space Science Data Center.
[16]P. J. Coleman, Jr., L. Davis, and C. P. Sonett, Phys. Rev. Lett. **5**, 43 (1960).
[17]M. Neugebauer and C. W. Snyder, Sci. **138**, 1095 (1962).
[18]W. D. Gonzalez, J. A. Joselyn, Y. Kamide, H. W. Kroehl, G. Rostoker, B. T. Tsurutani, and V. M. Vasyliunas, J. Geophys. Res. **99**, 5771, doi:10.1029/93JA02867 (1994).
[19]E. W. Maunder, Knowledge **17**, 173 (1894).
[20]A. M. Clerke, Knowledge **17**, 206 (1894).
[21]F. W. G. Spörer, Vierteljahrsschr. Astron. Ges. (Leipzig) **22**, 323–329 (1887).
[22]E. W. Maunder, Mon. Not. R. Astron. **50**, 251 (1890).
[23]J. A. Eddy, Science **192**, 1189 (1976).
[24]G. Rostoker and C.-G. Fäthammar, J. Geophys. Res. **72**, 5853, doi:10.1029/JZ072i023p05853 (1967).
[25]J. Hirshberg and D. S. Colburn, Planet. Space Sci. **17**, 1183 (1969).
[26]C. T. Russell, R. L. McPherron, and R. K. Burton, J. Geophys. Res. **79**, 1105, doi:10.1029/JA079i007p01105 (1974).
[27]L. F. Burlaga, E. Sittler, F. Mariani, and R. Schwenn, J. Geophys. Res. **86**, 6673, doi:10.1029/JA086iA08p06673 (1981).
[28]L. W. Klein and L. F. Burlaga, J. Gophys. Res. **87**, 613 (1982).
[29]L. F. Burlaga, L. Klein, N. R. Sheeley, Jr., D. J. Michels, R. A. Howard, M. J. Koomen, R. Schwenn, and H. Rosenbauer, Geophys. Res. Lett. **9**, 1317, doi:10.1029/GL009i012p01317(1982).
[30]R. M. Wilson and E. Hildner, Sol. Phys. **91**, 169 (1984).
[31]K. Marubashi, in *Coronal Mass Ejections*, Geophysical Monograph Series, Vol. 99, edited by N. Crooker, J. A. Joselyn, and J. Feynman (American Geophysics Union, Washington, DC, 1997), p. 147.
[32]M. L. Kaiser, *STEREO: Science and Mission Overview* (Johns Hopkins APL Technical Digest, 2009), Vol. 28, p. 2.
[33]V. Kunkel and J. Chen, Astrophys. J. Lett. **715**, L80 (2010).
[34]R. A. Howard *et al.*, Space Sci. Rev. **136**, 67 (2008).
[35]D. E. Larson *et al.*, Geophys. Res. Lett. **24**, 1911, doi:10.1029/97GL01878 (1997).
[36]J. Chen and D. A. Garren, Geophys. Res. Lett. **20**, 2319, doi:10.1029/93GL02426 (1993).
[37]S. T. Wu, W. P. Guo, D. J. Michels, and L. F. Burlaga, J. Geophys. Res. **104**, 14789, doi:10.1029/1999JA900099 (1999).
[38]*The Many Faces of the Sun*, edited by K. Strong, J. Saba, B. Haisch, and J. Schmelz (Springer, New York, 1999).
[39]J. A. Klimchuk, in *Space Weather*, Geophysical Monograph Vol. 125, edited by P. Song, H. Singer, and G. Siscoe (AGU, Washington, (2001), p. 143.
[40]W. D. Pesnell, B. J. Thompson, and P. C. Chamberlin, Sol. Phys. **275**, 3 (2012).
[41]P. F. Chen, Living Rev. Sol. Phys. **8**, 1 (2011).
[42]M. Aschwanden, *Physics of the Solar Corona* (Springer-Verlag, 2004).
[43]H. Zirin, *Astrophysics of the Sun* (Cambridge University Press, Cambridge, UK, 1988).
[44]E. Tandberg-Hanssen and A. G. Emslie, *The Physics of Solar Flares*, Cambridge Astrophysics Series No. 14 (Cambridge University Press, Cambridge, UK, 2009).
[45]A. O. Benz, Living Rev. Sol. Phys. **5**, 1 (2008).
[46]E. W. Cliver and H. S. Hudson, J. Atmos. Sol.-Terr. Phys. **64**, 231 (2002).
[47]H. S. Hudson, Space Sci. Rev. **158**, 5 (2011).
[48]S. Tsuneta *et al.*, Sol. Phys. **136**, 37 (1991).
[49]Y. Ogawara, T. Takano, T. Kato, T. Kosugi, S. Tsuneta, T. Watanabe, I. Kondo, and Y. Uchida, Sol. Phys. **136**, 1 (1991).
[50]In older literature, the term "disparition brusque" (DB) is encountered. In low time-resolution observations, filaments on the disk "suddenly" can disappear between successive images. They can also become invisible in filtergrams due to Doppler shift. They were presumed to expand away from the Sun as in prominence eruption. Eruptive prominence (EP) and disparition brusque (DB) refer to the same phenomenon, viewed from different observing angles relative to the erupting structures. Occasionally, dense and cold plasma of small extent is detected in the SW, which is interpreted as the remnants of erupted prominences.
[51]E. Tandberg-Hanssen, *The Nature of Solar Prominences* (Kluwer Academic, New York, 1995).
[52]T. Hirayama, Sol. Phys. **100**, 415 (1985).
[53]T. Hirayama, Sol. Phys. **24**, 310 (1972).
[54]D. A. Landman, Astrphys. J. **290**, 369 (1985).
[55]D. M. Rust, Astrophys. J. **150**, 313 (1967).
[56]J. L. Leroy, V. Bommier, and S. Sahal-Brechot, Sol. Phys. **83**, 135 (1983).
[57]E. Tandberg-Hanssen and U. Anzer, Sol. Phys. **15**, 158 (1970).
[58]M. J. Koomen, R. T. Seal, and R. Tousey, Bull. Am. Astron. Soc. **1**, 283 (1969).
[59]The OSO-7 coronagraph data were downlinked from the satellite to the ground in the form of pixel-by-pixel intensity data. The first CME to be observed occurred on 14 December 1971[12] and appeared as patches of saturated pixels. The first person to see this occurrence was David Roberts, who was an electronics engineer at the Naval Research Laboratory. The initial thought was that the instrument had malfunctioned. Much to the surprise of the researchers who gathered to examine this anomaly, G. E. Brueckner and R. A. Howard, the next set of data showed that the high intensity values moved outward to new pixels, proving that the "anomaly" was not due to the failure of the pixels.
[60]R. M. MacQueen, J. A. Eddy, J. T. Gosling, E. Hildner, R. H. Munro, G. A. Newkirk, Jr., A. I. Poland, and C. L. Ross, Astrophys. J. **187**, L85 (1974).
[61]N. R. Sheeley, Jr., D. J. Michels, R. A. Howard, and M. J. Koomen, Astrophys. J. Lett. **237**, L99 (1980).
[62]R. M. MacQueen, A. Csoeke-Poeckh, E. Hildner, L. House, R. Reynolds, A. Stanger, H. Tepoel, and W. Wagner, Sol. Phys. **65**, 91 (1980).

[63]R. R. Fisher, R. H. Lee, R. M. MacQueen, and A. I. Poland, Appl. Opt. **20**, 1094 (1981).
[64]J. T. Gosling, E. Hildner, R. M. MacQueen, R. H. Munro, A. I. Poland, and C. L. Ross, J. Geophys. Res. **79**, 4581, doi:10.1029/JA079i031p04581 (1974).
[65]E. Hildner, J. T. Gosling, R. M. MacQueen, R. H. Munro, A. I. Poland, and C. L. Ross, Sol. Phys. **48**, 127 (1976).
[66]R. R. Fisher and A. I. Poland, Astrophys. J. **246**, 1004 (1981).
[67]R. A. Howard, N. R. Sheeley, Jr., M. J. Koomen, and D. J. Michels, J. Geophys. Res. **90**(A9), 8173, doi:10.1029/JA090iA09p08173 (1985).
[68]R. M. E. Illing and A. J. Hundhausen, J. Geophys. Res. **90**, 275, doi:10.1029/JA090iA01p00275 (1985).
[69]A. J. Hundhausen, in *The Many Faces of the Sun*, edited by K. Strong, J. Saba, B. Haisch, and J. Schmelz, (Springer-Verlag, New York, 1999), p. 143.
[70]O. C. St. Cyr, J. T. Burkepile, A. J. Hundhausen, and A. R. Lecinski, J. Geophys. Res. **104**, 12493, doi:10.1029/1999JA900045 (1999).
[71]R. M. E. Illing and A. J. Hundhausen, J. Geophys. Res. **91**, 10951, doi:10.1029/JA091iA10p10951 (1986).
[72]E. E. Billings, *A Guide to the Solar Corona* (Academic, New York, 1966), Chap. 6.
[73]V. Rusin and M. Rybansky, Bull. Astron. Inst. Czech. **33**, 219 (1982).
[74]R. J. Munro, J. T. Gosling, E. Hildner, R. M. MacQueen, A. I. Poland, and C. L. Ross, Sol. Phys. **61**, 201 (1979).
[75]T. C. Mouschovias and A. I. Poland, Astrophys. J. **220**, 675 (1978).
[76]U. Anzer, Sol. Phys. **57**, 111 (1978).
[77]W. van Tend, Sol. Phys. **61**, 89 (1979).
[78]R. A. Howard, D. J. Michels, N. R. Sheeley, Jr., and M. J. Koomen, Astrophys. J. **263**, L101 (1982).
[79]A. J. Hundhausen, EOS **65**, 1069 (1984).
[80]D. F. Webb, J. Geophys. Res. **93**, 1749, doi:10.1029/JA093iA03p01749 (1988).
[81]R. R. Fisher and R. H. Munro, Astrophys. J. **280**, 428 (1984).
[82]R. A. MacQueen, Sol. Phys. **145**, 169 (1993).
[83]G. E. Brueckner *et al*., Sol. Phys. **162**, 357 (1995).
[84]V. Domingo *et al*., Sol. Phys. **162**, 1 (1995). SOHO is a joint mission of the National Aeronautics and Space Administration (NASA) and the European Space Agency (ESA).
[85]J. Chen, Astrophys. J. **338**, 453 (1989).
[86]J. Chen, J. Geophys. Res. **101**, 27499, doi:10.1029/96JA02644 (1996).
[87]J. Chen, R. A. Howard, G. E. Brueckner, R. Santoro, J. Krall, S. E. Paswaters, O. C. St. Cyr, R. Schwenn, P. Lamy, and G. M. Simnett, Astrophys. J. Lett. **490**, L191 (1997).
[88]A. F. R. Thernisien, R. A. Howard, and A. Vourlidas, Astrophys. J. **652**, 763 (2006).
[89]J. Krall, Astrophys. J. **657**, 559 (2007).
[90]M. G. Linton and M. B. Moldwin, J. Geophys. Res. **114**, A00B09 doi:10.1029/2008JA013660 (2009).
[91]P. Démoulin, A. Vourlidas, M. Pick, and A. Bouteille, Astrophys. J. **754**, 156 (2012); Erratum **750**, 147 (2012).
[92]J. Zhang, P. Hess, and W. Poomvises, Sol. Phys. **284**, 89 (2013).
[93]A. Vourlidas, B. J. Lynch, R. A. Howard, and Y. Li, Sol. Phys. **284**, 179 (2013).
[94]B. E. Wood, M. Karovska, J. Chen, G. E. Brueckner, J. W. Cook, and R. A. Howard, Astrophys. J. **512**, 484 (1999).
[95]J. Chen, R. A. Santoro, J. Krall, R. A. Howard, R. Duffin, J. D. Moses, G. E. Brueckner, J. A. Darnell, and J. T. Burkepile, Astrophys. J. **533**, 481 (2000).
[96]J. Krall, J. Chen, R. T. Duffin, R. A. Howard, and B. J. Thompson, Astrophys. J. **562**, 1045 (2001).
[97]S. E. Gibson, D. Foster, J. Burkepile, G. de Toma, and A. Stanger, Astrophys. J. **641**, 590 (2006).
[98]S. Patsourakos, A. Vourlidas, and G. Stenborg, Astrophys. J. **764**, 125 (2013).
[99]G. Chintzoglou, S. Patsourakos, and A. Vourlidas, Astrophys. J. **809**, 34 (2015).
[100]E. Robbrecht, S. Patsourakos, and A. Vourlidas, Astrophys. J. **701**, 283 (2009).
[101]H. Ji, H. Wang, E. J. Schmahl, Y.-J. Moon, and Y. Jiang, Astrophys. J. **595**, L135 (2003).
[102]D. J. Christian, D. B. Jess, P. Antolin, and M. Mathioudakis, Astrophys. J. **804**, 147 (2015).
[103]X. Cheng, Q. Hao, M. D. Ding, K. Liu, P. F. Chen, C. Fang, and Y. D. Liu, Astrophys. J. **809**, 46 (2015).
[104]S. E. Gibson and Y. Fan, Astrophys. J. **637**, L65 (2006).
[105]This exceptionally large flare is sometimes referred to as the "Carrington" flare or event. In light of the simultaneous observations by the two astronomers in London and their back to back reports in the *Monthly Notices of the Royal Astronomical Society*,[1,2] it seems more appropriate to refer to it as the "Carrington-Hodgson" event, if a name is to be given.
[106]B. T. Tsurutani, W. D. Gonzalez, G. S. Lakhina, and S. Alex, J. Geophys. Res. **108**(A7), 1268, doi:10.1029/2002JA009504 (2003).
[107]S.-I. Akasofu and Y. Kamide, J. Geophys. Res. **110**, A09226, doi:10.1029/2005JA011005 (2005); B. T. Tsurutani, W. D. Gonzalez, G. S. Lakhina, and S. Alex, J. Geophys. Res. **110**, A09227, doi:10.1029/2005JA011121 (2005).
[108]E. W. Cliver and L. Svalgaard, Sol. Phys. **224**, 407 (2004).
[109]E. W. Maunder, Astrophys. J. **21**, 101 (1905).
[110]S. Chapman and V. C. A. Ferraro, Nature **126**, 129 (1930).
[111]L. Biermann, Z. Astrophys. **25**, 161 (1948).
[112]L. Biermann, Z. Astrophys. **29**, 274 (1951).
[113]S. Chapman, Smithson. Contrib. Astrophys. **2**, 2 (1957).
[114]E. N. Parker, Astrophys. J. **128**, 664 (1958).
[115]H. Alfén, Tellus **9**, 92 (1957).
[116]In the solar physics literature, the spiral solar wind magnetic field from the Sun is attributed to Parker,[114] but Alfén[115] had earlier used a plasma medium with embedded spiral field lines in a theory of comet tails, which is essentially the one in current use.
[117]*The Physics of Inner Heliosphere*, edited by R. Schwenn and E. Marsch (Springer-Verlag, New York, 1991), Vol. 1.
[118]*The Physics of Inner Heliosphere*, edited by R. Schwenn and E. Marsch (Springer-Verlag, New York, 1991), Vol. 2.
[119]D. J. McComas *et al*., Geophys. Res. Lett. **25**, 1, doi:10.1029/97GL03444 (1998).
[120]J. Chen, P. J. Cargill, and P. J. Palmadesso, J. Geophys. Res. **102**, 14701, doi:10.1029/97JA00936 (1997).
[121]C. Arge, S. Wahl, J. Chen, S. Slinker, and V. Pizzo, in *Solar-Terrestrial Magnetic Activity and Space Environment*, COSPAR Colloquia Series, Vol. 14, edited by H. N. Wang and R. L. Xu (Elsevier, New York, 2002), p. 393.
[122]J. Chen, S. P. Slinker, and I. Triandaf, Space Weather **10**, S04005, doi:10.1029/2011SW000740 (2012).
[123]M. Sugiura, in *Annals of the International Geophysical Year* (Pergamon, Oxford, UK, 1964), Vol. 35, pp. 945–948.
[124]J. W. Dungey, Phys. Rev. Lett. **6**, 47 (1961).
[125]W. M. Neupert and V. Pizzo, J. Geophys. Res. **79**, 3701, doi:10.1029/JA079i025p03701 (1974).
[126]N. R. Sheeley, Jr., J. W. Harvey, and W. C. Feldman, Sol. Phys. **49**, 271 (1976).
[127]C. P. Sonett, D. S. Colburn, L. Davis, E. J. Smith, and P. J. Coleman, Jr., Phys. Rev. Lett. **13**, 153 (1964).
[128]S. W. Kahler, Ann. Rev. Astron. Astrophys. **30**, 113 (1992).
[129]J. T. Gosling, J. Geophys. Res. **98**, 18937, doi:10.1029/93JA01896 (1993).
[130]D. V. Reames, Space Sci. Rev. **90**, 413 (1999).
[131]S.-I. Akasofu, *Physics of Magnetospheric Substorms* (D. Reidel Publishing, Dordrecht, The Netherlands, 1977).
[132]S.-I. Akasofu, Space Sci. Rev. **28**, 121 (1981).
[133]L. F. Burlaga, J. Geophys. Res. **93**, 7217, doi:10.1029/JA093iA07p07217 (1988).
[134]R. P. Lepping, J. A. Jones, and L. F. Burlaga, J. Geophys. Rev. **95**, 11957 (1990).
[135]V. Bothmer and R. Schwenn, Space Sci. Rev. **70**, 215 (1994).
[136]P. Démoulin and S. Dasso, Astron. Astrophys. **498**, 551 (2009).
[137]S. Lundquist, Ark. Fys. **2**, 361 (1950).
[138]J. Chen, Astrophys. J. **761**, 179 (2012).
[139]T. Nieves-Chinchilla, M. G. Linton, M. A. Hidalgo, A. Vourlidas, N. P. Savani, A. Szabo, C. Farrugia, and W. Yu, Astrophys. J. **823**, 27 (2016).
[140]L. J. Lanzerotti, Space Sci. Rev. **34**, 347 (1983).
[141]J. Allen, H. Sauer, L. Frank, and P. Reiff, EOS, Trans. Am. Geophys. Union **70**, 1479 (1989). Also see publications of the National Space Weather Program, Office of the Federal Coordinator for Meteorology.
[142]D. H. Boteler, Nat. Hazards **23**, 101 (2001).
[143]S. Basu *et al*., J. Geophys. Res. **113**, A00A06, doi:10.1029/2008JA013076 (2008).
[144]J. T. Gosling, D. N. Baker, S. J. Bame, W. C. Feldman, R. D. Zwickl, and E. J. Smith, J. Geophys. Res. **92**, 8519, doi:10.1029/JA092iA08p08519 (1987).
[145]R. M. Skoug, W. C. Feldman, J. T. Gosling, and D. J. McComas, J. Geophys. Res. **105**, 23069, doi:10.1029/2000JA000017 (2000).

[146]A. Wittmann, Astron. Astrophys. **66**, 93 (1978).
[147]Most historical accounts credit Thomas Harriot for the first telescopic observation of sunspots (See http://galileo.rice.edu/sci/observations/sunspots.html for *The Galileo Project*). Other observers included David and Johannes Fabricius, Galileo Galilei, and Christoph Scheiner. In addition to observing four moons of Jupiter (1610), Galileo noted that sunspots became foreshortened as they moved toward the limb. He inferred that sunspots were features on the hemispherical solar surface rotating with the Sun.
[148]G. E. Hale, Astrophys. J. **28**, 315 (1908).
[149]S. K. Solanki, Space Sci. Rev. **63**, 1 (1993).
[150]J. E. Vernazza, E. H. Avrett, and R. Loeser, Astrophys. J. **45**, 635 (1981).
[151]G. B. Scharmer, B. V. Gudiksen, M. G. Löfdahl, and L. H. M. Rouppe van der Voort, Nature **420**, 151 (2002).
[152]J. Christensen-Dalsgaard *et al*., Science **272**, 1286 (1996).
[153]G. B. Scharmer *et al*., Astrophys. J. Lett. **689**, L69 (2008).
[154]The photon mean free path in the photosphere is about 100 km.[156] Thus, these measurements are near the diffraction limit, requiring large apertures to maximize the photon count.
[155]A. G. Kosovichev *et al*., Sol. Phys., Sol. Phys. **170**, 43 (1997).
[156]J. W. Harvey *et al*., Science **272**, 1284 (1996).
[157]T. L. Duvall, Jr., J. W. Harvey, and M. A. Pomerantz, Nature **321**, 500 (1986).
[158]J. Christensen-Dalsgaard, D. O. Gough, and M. J. Thompson, Astrophys. J. **378**, 413 (1991).
[159]A. G. Kosovichev and A. V. Fedorova, Astron. Zh. **68**, 1015 (1991).
[160]D. O. Gough, J. W. Leibacher, P. H. Scherrer, and J. Toomre, Science **272**, 1281 (1996).
[161]E. A. Milne, Mon. Not. R. Astron. Soc. **81**, 361 (1921).
[162]P. H. Scherrer, R. S. Bogart, R. I. Bush, J. T. Hoeksema, A. G. Kosovichev, and J. Schou, Sol. Phys. **162**, 129 (1995).
[163]K. S. Balasubramaniam and A. A. Pevtsov, Proc. SPIE **8148**, 814809 (2011).
[164]J. O. Stenflo, Astron. Astrophys. **555**, A132 (2013).
[165]H. J. Hagenaar, C. J. Schrijver, A. M. Title, and R. A. Shine, Astrophys. J. **511**, 932 (1999).
[166]T. Kosugi, K. Matsuzaki *et al*., Sol. Phys. **243**, 3 (2007).
[167]J. Pietarila Graham, S. Danilovic, and J. Schüssler, Astrophys. J. **693**, 1728 (2009).
[168]J. O. Stenflo, Astron. Astrophys. **541**, A17 (2012).
[169]C. E. Parnell, C. E. DeForest, H. J. Hagenaar, B. A. Johnston, D. A. Lamb, and B. T. Welsch, Astrophys. J. **698**, 75 (2009).
[170]S. Tsuneta *et al*., "The solar optical telescope for the hinode mission: An overview," Sol. Phys. **249**, 167 (2008).
[171]G. E. Hale and F. Ellerman, Publ. Yerkes Obs. **3**(I), 3 (1903).
[172]H. Deslandres, Ann. Obs. Paris-Meudon **4**(I), 1 (1910).
[173]J.-P. Delaboudiniere *et al*., Sol. Phys. **162**, 291 (1995).
[174]B. N. Handy *et al*., Sol. Phys. **187**, 229 (1999).
[175]K. J. H. Phillips, C. Chifor, and E. Landi, Astrophys. J. **626**, 1110 (2005).
[176]M. J. Aschwanden, L. Fletcher, C. J. Schrijver, and D. Alexander, Astrophys. J. **520**, 880 (1999).
[177]V. M. Nakariakov, L. Ofman, E. E. DeLuca, B. Roberts, and J. M. Davila, Science **285**, 862 (1999).
[178]C. S. Schrijver *et al*., Sol. Phys. **187**, 261 (1999).
[179]J. Chen and P. W. Schuck, Sol. Phys. **246**, 145 (2007).
[180]I. Arregui, J. L. Ballester, and M. Goossens, Astrophys. J. **676**, L77 (2008).
[181]V. M. Nakariakov, M. J. Aschwanden, and T. van Doorsselaere, Astron. Astrophys. **502**, 661 (2009).
[182]C. De Loore, Astrophys. Space Sci. **6**, 60 (1970).
[183]R. L. Moore and P. C. W. Fung, Sol. Phys. **23**, 78 (1972).
[184]R. W. P. McWhirter and R. Wilson, Philos. Trans. R. Soc. London A **281**, 331 (1976).
[185]R. Tousey *et al*., Sol. Phys. **33**, 265 (1973).
[186]G. S. Vaiana, J. M. Davis, R. Giacconi, A. S. Krieger, J. K. Silk, A. F. Timothy, and M. Zombeck, Astrophys. J. **185**, L47 (1973).
[187]P. V. Foukal, Astrophys. J. **210**, 575 (1976).
[188]J. A. Klimchuk, Sol. Phys. **193**, 53 (2000).
[189]R. J. Bray, L. E. Cram, C. J. Durrant, and R. E. Loughhead, *Plasma Loops in the Solar Corona* (Cambridge University Press, New York, 1991).
[190]M. C. M. Cheung, M. Schüssler, and F. Moreno-Inseretis, Astron. Astrophys. **467**, 703 (2007).
[191]W. P. Abbett, Astrophys. J. **665**, 1469 (2007).
[192]M. C. M. Cheung, M. Rempel, A. M. Title, and M. Schüssler, Astrophys. J. **720**, 233 (2010).
[193]R. F. Stein and A. Nordlund, Astrophys. J. Lett. **753**, L13 (2012).
[194]H. W. Babcock, Astrophys. J. **133**, 572 (1961).
[195]E. N. Parker, *Cosmical Magnetic Fields* (Oxford University Press, Oxford, UK, 1979).
[196]F. Moreno-Insertis and T. Emonet, Astrophys. J. Lett. **472**, L53 (1996).
[197]D. W. Longcope and I. Klapper, Astrophys. J. **488**, 443 (1997).
[198]Y. Fan, E. G. Zweibel, and S. R. Lantz, Astrophys. J. **493**, 480 (1998).
[199]W. B. Manchester, T. I. Gombosi, I. Roussev, D. L. de Zeeuw, I. V. Sokolov, K. G. Powell, G. Tóth, and M. Opher, J. Geophys. Res. **109**, A01102, doi:10.1029/2002JA009672 (2004).
[200]W. B. Manchester, T. I. Gombosi, I. Roussev, A. Ridley, D. L. de Zeeuw, I. V. Sokolov, K. G. Powell, and G. Tóth, J. Geophys. Res. **109**, A02107, doi:10.1029/2003JA010150 (2004).
[201]W. P. Abbett and G. H. Fisher, Astrophys. J. **582**, 475 (2003).
[202]A. Bruzek, Sol. Phys. **2**, 451 (1967).
[203]D.-Y. Chou and H. Zirin, Astrophys. J. **333**, 420 (1988).
[204]S. R. Weart and H. Zirin, Publ. Astron. Soc. Pac. **81**, 270 (1969).
[205]H. Wang, J. Qiu, J. Jing, and H. Zhang, Astrophys. J. **593**, 564 (2003).
[206]B. Vršnak, K.-L. Klein, A. Warmuth, W. Otruba, and M. Skender, Sol. Phys. **214**, 325 (2003).
[207]J. Qiu, H. M. Wnag, C. Z. Cheng, and D. E. Gary, Astrophys. J. **604**, 900 (2004).
[208]P. W. Schuck, J. Chen, I. B. Schwartz, and V. Yurchyshyn, Astrophys. J. Lett. **610**, L133 (2004).
[209]J. Chen and V. Kunkel, Astrophys. J. **717**, 1105 (2010).
[210]R. A. Harrison, Astron. Astrophys. **162**, 283 (1986).
[211]S. T. Wu, Space Sci. Rev. **32**, 115 (1982).
[212]M. Dryer, Space Sci. Rev. **33**, 233 (1982).
[213]J. Sakai and K.-I. Nishikawa, Sol. Phys. **88**, 241 (1983).
[214]R. S. Steinolfson, in *Collisionless Shocks in the Heliosphere*, Geophysics Monograph Vol. 35, edited by B. T. Tsurutani and R. G. Stone (American Geophysical Union, 1985), p. 1.
[215]A. Maxwell, M. Dryer, and P. McIntosh, Sol. Phys. **97**, 401 (1985).
[216]G. M. Simnett and R. A. Harrison, Sol. Phys. **99**, 291 (1985).
[217]D. F. Webb and A. J. Hundhausen, Sol. Phys. **108**, 383 (1987).
[218]R. A. Harrison, Astron. Astrophys. **304**, 585 (1995).
[219]J. Zhang, K. P. Dere, R. A. Howard, M. R. Kundu, and S. M. White, Astrophys. J. **559**, 452 (2001).
[220]J. Chen and J. J. Krall, Geophys. Res. **108**, 1410, doi:10.1029/2003JA009849 (2003).
[221]D. Maričič, B. Vršnak, A. L. Stanger, A. M. Veronig, M. Temmer, and D. Roša, Sol. Phys. **241**, 99 (2007).
[222]M. Temmer, A. M. Veronig, B. Vršnak, J. Rybák, P. Gömöry, S. Stoiser, and D. Maričič, Astrophys. J. **673**, L95 (2008).
[223]S. W. Kahler, R. L. Moore, S. R. Kane, and H. Zirin, Astrophys. J. **328**, 824 (1988).
[224]R. L. Moore, A. C. Sterling, and S. T. Suess, Astrophys. J. **668**, 1221 (2007).
[225]X. P. Zhao, S. P. Plunkett, and W. Liu, J. Geophys. Res. **107**, SSH 13-1, doi:10.1029/2001JA009143 (2002).
[226]H. Xie, L. Ofman, and G. Lawrence, J. Geophys. Res. **109**, A03109, doi:10.1029/2003JA010226 (2004).
[227]X. H. Xue, C. B. Wang, and X. K. Dou, J. Geophys. Res. **110**, A08103, doi:10.1029/2004JA010698 (2005).
[228]T. R. Detman, M. Dryer, T. Yet, S. M. Han, S. T. Wu, and D. J. McComas, J. Geophys. Res. **96**, 9531, doi:10.1029/91JA00443 (1991).
[229]C. A. de Koning, G. Millward, V. J. Pizzo, and D. A. Biesecker, AIP Conf. Proc. **1500**, 20 (2012).
[230]B. C. Low, Astrophys. J. **212**, 234 (1977).
[231]K. Jockers, Sol. Phys. **56**, 37 (1978).
[232]J. Birn and K. Schindler, in *Solar Flare Magnetohydrodynamics*, edited by E. R. Priest (Gordon and Breach, New York, NY, 1981), p. 337.
[233]Z. Mikić, D. C. Barnes, and D. D. Schnack, Astrophys. J. **328**, 830 (1988).
[234]D. Biskamp and H. Welter, Sol. Phys. **120**, 49 (1989).
[235]Z. Mikić, Phys. Fluids B **2**, 1450 (1990).
[236]E. R. Priest and T. G. Forbes, Sol. Phys. **126**, 319 (1990).
[237]J. M. Finn and J. Chen, Astrophys. J. **349**, 345 (1990).
[238]T. G. Forbes and P. A. Isenberg, Astrophys. J. **373**, 294 (1991).
[239]T. G. Forbes and E. R. Priest, Astrophys. J. **446**, 377 (1995).
[240]S. T. Wu, M. T. Song, P. C. Martens, and M. Dryer, Sol. Phys. **134**, 353 (1991).

[241]J. M. Finn, P. N. Guzdar, and J. Chen, Astrophys. J. **393**, 800 (1992).
[242]Z. Mikić and J. A. Linker, Astrophys. J. **430**, 898 (1994).
[243]E. N. Parker, J. Geophys. Res. **101**, 10587, doi:10.1029/95JA02866 (1996).
[244]S. K. Antiochos, C. R. DeVore, and J. A. Klimchuk, Astrophys. J. **510**, 485 (1999).
[245]P. F. Chen and K. Shibata, Astrophys. J. **545**, 524 (2000).
[246]J. A. Linker, R. Lionello, Z. Mikić, and T. Amari, J. Geophys. Res. **106**, 25165, doi:10.1029/2000JA004020 (2001).
[247]D. Uzdensky, Astrophys. J. **574**, 1011 (2002).
[248]C. Z. Cheng, Y. Ren, G. S. Choe, and Y.-J. Moon, Astrophys. J. **596**, 1341 (2003).
[249]T. Amari, J. F. Luciani, Z. Mikić, and J. Linker, Astrophys. J. **529**, L49 (2000).
[250]A. A. van Ballegooijen and P. C. H. Martens, Astrophys. J. **343**, 971 (1989).
[251]B. Inhester, J. Birn, and M. Hesse, Sol. Phys. **138**, 257 (1992).
[252]T. G. Forbes, J. Geophys. Res. **95**, 11919, doi:10.1029/JA095iA08p11919 (1990).
[253]R. G. Giovanelli, Nature **158**, 81 (1946).
[254]R. G. Giovanelli, Mon. Not. R. Astron. Soc. **107**, 338 (1947).
[255]P. A. Sweet, "Electromagnetic phenomena in cosmical physics," in *Proceedings of the International Astronomical Union Symposium No. 6*, edited by B. Lehnert (Cambridge University Press, 1958), p. 123.
[256]T. Gold and F. Hoyle, Mon. Not. R. Astron. Soc. **120**, 89 (1960).
[257]H. Alfén and P. Carlquist, Sol. Phys. **1**, 220 (1967).
[258]S. S. Hasan and D. ter Haar, Astrophys. Space Sci. **56**, 89 (1978).
[259]H. Carmichael, "A process for flares: The physics of solar flares," in Proceedings of the AAS-NASA Symposium, edited by W. N. Hess (NASA, Washington, DC, 1964), Vol. SP-50, pp. 451–456.
[260]P. A. Sturrock, Nature **211**, 695 (1966).
[261]T. Hirayama, Sol. Phys. **34**, 323 (1974).
[262]R. A. Kopp and G. W. Pneuman, Sol. Phys. **50**, 85 (1976).
[263]Z. Švestka and E. W. Cliver, in *Eruptive Solar Flares*, Lecture Notes in Physics, Vol. 399, edited by Z. Švestka, B. V. Jackson, and M. E. Machado (Springer Verlag, 1992), p. 1.
[264]P. C. H. Martens and N. P. M. Kuin, Sol. Phys. **122**, 263 (1989).
[265]P. Démoulin and M. A. Raadu, Sol. Phys. **142**, 291 (1992).
[266]M. Kuperus and M. A. Raadu, Astron. Astrophys. **31**, 189 (1974).
[267]B. C. Low and J. R. Hundhausen, Astrophys. J. **443**, 818 (1995).
[268]R. Kippenhahn and A. Schlüter, Z. Astrophys. **43**, 36 (1957).
[269]W. van Tend and M. Kuperus, Sol. Phys. **59**, 115 (1978).
[270]M. M. Molodenskii and B. P. Filippov, Sov. Astron. **31**, 564 (1987).
[271]P. A. Isenberg, T. G. Forbes, and P. Démoulin, Astrophys. J. **417**, 368 (1993).
[272]K. Shibata and T. Magara, Living Rev. Sol. Phys. **8**, 6 (2011).
[273]J. Lin and T. G. Forbes, J. Geophys. Res. **105**, 2375, doi:10.1029/1999JA900477 (2000).
[274]J. A. Linker, Z. Mikić, R. Lionello, P. Riley, T. Amari, and D. Odstrcil, Phys. Plasmas **10**, 1971 (2003).
[275]R. L. Moore, A. C. Sterling, H. S. Hudson, and J. R. Lemen, Astrophys. J. **552**, 833 (2001).
[276]J. T. Karpen, S. K. Antiochos, and C. R. DeVore, Astrophys. J. **760**, 81 (2012).
[277]D. MacTaggard and A. W. Hood, Astron. Aastrophys. **501**, 761 (2009).
[278]B. J. Lynch, S. K. Antiochos, Y. Li, J. G. Luhman, and C. R. DeVore, Astrophys. J. **697**, 1918 (2009).
[279]J. J. Aly, Astrophys. J. **283**, 349 (1984).
[280]J. J. Aly, Astron. Astrophys. **193**, 19 (1985).
[281]J. Birn, J. F. Drake, M. A. Shay, B. N. Rogers, R. E. Denton, M. Hesse, M. Kuznetsova, Z. W. Ma, A. Bhattacharjee, A. Otto, and P. L. Pritchett, J. Geophys. Res. **106**, 3715, doi:10.1029/1999JA900449 (2001).
[282]W. Daughton *et al*., Phys. Rev. Lett. **103**, 065004 (2009).
[283]L. H. Strous, G. Scharmer, T. D. Tarbell, A. M. Title, and C. Zwaan, Astron. Astrophys. **306**, 947 (1996).
[284]L. H. Strous and C. Zwaan, Astrophys. J. **527**, 435 (1999).
[285]S. P. Plunkett, A. Vourlidas, S. Simberova, J. Karlicky, P. Kotrc, P. Heinzel, Y. A. Kupryakov, W. P. Guo, and S. T. Wu, Sol. Phys. **194**, 371 (2000).
[286]N. Gopalswamy, AIP Conf. Proc. **1539**, 5 (2013).
[287]W. Liu, Q. Chen, and V. Petrosian, Astrophys. J. **767**, 168 (2013).
[288]G. A. Doschek, D. E. McKenzie, and H. P. Warren, Astrophys. J. **788**, 26 (2014).
[289]P. A. Isenberg and T. G. Forbes, Astrophys. J. **670**, 1453 (2007).
[290]J. Chen, Space Sci. Rev. **95**, 165 (2001).
[291]I. I. Roussev, T. G. Forbes, T. I. Gombosi, I. V. Sokolov, D. L. DeZeeuw, and J. Birn, Astrophys. J. Lett. **588**, L45 (2003).
[292]P. D'emoulin and E. R. Priest, Astron. Astrophys. **206**, 336 (1988).
[293]B. Vršnak, Sol. Phys. **129**, 295 (1990).
[294]S. E. Gibson and B. C. Low, Astrophys. J. **493**, 460 (1998).
[295]S. T. Wu, W. P. Guo, and M. Dryer, Sol. Phys. **170**, 265 (1997).
[296]Y. Fan and S. E. Gibson, Astrophys. J. **589**, L105 (2003).
[297]W. Manchester, IV, T. Gombosi, D. DeZeeuw, and Y. Fan, Astrophys. J. **610**, 588 (2004).
[298]B. Kliem and T. Török, Phys. Rev. Lett. **96**, 255002 (2006).
[299]V. D. Shafranov, in *Reviews of Plasma Physics*, edited by M. A. Leontovich (Consultants Bureau, New York, 1966), Vol. 2, p. 103.
[300]B. Filippov and S. Koutchmy, Ann. Geophys. **26**, 3025 (2008).
[301]J. M. Malherbe and E. R. Priest, Astron. Astrophys. **123**, 80 (1983).
[302]T. Amari, P. Démoulin, P. Browning, A. Hood, and E. Priest, Astron. Astrophys. **241**, 604 (1991).
[303]M. S. Wheatland, Astrophys. J. **532**, 616 (2000).
[304]G. J. D. Petrie, Sol. Phys. **287**, 415 (2013).
[305]M. Janvier, G. Aulanier, V. Bommier, B. Schmieder, P. Démoulin, and E. Pariat, Astrophys. J. **788**, 60 (2014).
[306]K. Tanaka, Sol. Phys. **136**, 133 (1991).
[307]B. W. Lites, B. C. Low, V. Martnez Pillet, P. Seagraves, A. Skumanich, Z. A. Frank, R. A. Shine, and S. Tsuneta, Astrophys. J. **446**, 877 (1995).
[308]K. D. Leka, R. C. Canfield, A. N. McClymont, and L. van Driel-Gesztelyi, Astrophys. J. **462**, 547 (1996).
[309]B. W. Lites, Astrophys. J. **622**, 1275 (2005).
[310]M. L. Xue and J. Chen, Sol. Phys. **84**, 119 (1983).
[311]J. Lin, T. G. Forbes, P. A. Isenberg, and P. Démoulin, Astrophys. J. **504**, 1006 (1998).
[312]S. V. Titov and P. Démoulin, Astron. Astrophys. **351**, 707 (1999).
[313]J. Krall and J. Chen, Astrophys. J. **628**, 1046 (2005).
[314]D. J. McComas, J. Phillips, A. J. Hundhausen, and J. T. Burkepile, Geophys. Res. Lett. **18**, 73, doi:10.1029/90GL02480 (1991).
[315]D. F. Webb and E. W. Cliver, J. Geophys. Res. **100**, 5853, doi:10.1029/94JA02731 (1995).
[316]D. F. Webb, J. Burkepile, T. G. Forbes, and P. Riley, J. Geophys. Res. **108**, 1440, doi:10.1029/2003JA009923 (2003).
[317]T. Török and B. Kliem, Astrophys. J. **630**, L97 (2005).
[318]J. Chen, C. Marqué, A. Vourlidas, J. Krall, and P. W. Schuck, Astrophys. J. **649**, 452 (2006).
[319]K. P. Dere, G. E. Brueckner, R. A. Howard, D. J. Michels, and J. P. Delaboudiniere, Astrophys. J. **516**, 465 (1999).
[320]J. Krall, V. B. Yurchyshyn, S. Slinker, R. M. Skoug, and J. Chen, Astrophys. J. **642**, 541 (2006).
[321]B. Vršnak, J. Geophys. Res. **106**, 25249, doi:10.1029/2000JA004007 (2001).
[322]U. Anzer and J. J. Ballester, Astron. Astrophys. **238**, 365 (1990).
[323]L. D. Landau, E. M. Lifshitz, and L. P. Pitaevskii, *Electrodynamics of Continuous Media*, 2nd ed. (Pergamon, New York, 1984), p. 124.
[324]V. S. Mukhovatov and V. D. Shafranov, Nucl. Fusion **11**, 605 (1971).
[325]J. Krall, J. Chen, and R. Santoro, Astrophys. J. **539**, 964 (2000).
[326]O. Engvold, J. Malville, and B. M. Rustad, Sol. Phys. **48**, 137 (1976).
[327]B. Vršnak, V. Ruždjak, and B. Rompolt, Sol. Phys. **136**, 151 (1991).
[328]R. S. Steinolfson and A. J. Hundhausen, J. Geophys. Res. **93**, 14269, doi:10.1029/JA093iA12p14269 (1988).
[329]P. J. Cargill, J. Chen, and D. A. Garren, Astrophys. J. **423**, 854 (1994).
[330]D. A. Garren and J. Chen, Phys. Plasmas **1**, 3425 (1994).
[331]V. Kunkel, Ph.D. thesis, George Mason University, Fairfax, VA (2012).
[332]P. J. Cargill, J. Chen, D. S. Spicer, and S. T. Zalesak, Geophys. Res. Lett. **22**, 647, doi:10.1029/95GL00013 (1995).
[333]P. J. Cargill, J. Chen, D. S. Spicer, and S. T. Zalesak, **101**, 4855 (1996).
[334]S. J. Tappin, Sol. Phys. **233**, 233 (2006).
[335]T. A. Howard, C. D. Fry, J. C. Johnston, and D. F. Webb, Astrophys. J. **667**, 610 (2007).
[336]B. Vršnak, T. Žic, T. V. Falkenberg, C. Möstl, S. Vennerstrom, and D. Vrbanec, Astron. Astrophys. **512**, 43 (2010).
[337]P. J. Cargill, Sol. Phys. **221**, 135 (2004).
[338]P. Subramanian, A. Lara, and A. Borgazzi, Geophys. Res. Lett. **39**, L19107, doi:10.1029/2012GL053625 (2012).
[339]G. K. Batchelor, *An Introduction to Fluid Dynamics* (Cambridge University Press, New York, 1967).
[340]N. Gopalswamy, A. Lara, R. P. Lepping, M. L. Kaiser, D. Berdichevsky, and O. C. St. Cyr, Geophys. Res. Lett. **27**, 145, doi:10.1029/1999GL003639 (2000).

[341]R. P. Feynman, R. B. Leighton, and M. Sands, *The Feynman Lectures on Physics* (Addison-Wesley, Reading, MA, 1964), Vol. II.
[342]G. Van Hoven, C. Chiuderi, and R. Giachetti, Astrophys. J. **213**, 869 (1977).
[343]C. Chiuderi, R. Giachetti, and G. van Hoven, Sol. Phys. **54**, 107 (1977).
[344]T. Sakurai, Publ. Astron. Soc. Jpn. **28**, 177 (1976).
[345]A. W. Hood and E. R. Priest, Sol. Phys. **73**, 289 (1981).
[346]T. Török, B. Kliem, and V. S. Titov, Astron. Astrophys. **413**, L27 (2004).
[347]J. Chen, in *Coronal Mass Ejections*, Geophysics Monography Series Vol. 99, edited by N. Crooker, J. A. Joselyn, and J. Feynman (American Geophysics Union, Washington, DC, 1997), p. 65.
[348]B. R. Suydam, in *Porceedings of the 2nd UN Conference on the Peaceful Use of Atomic Energy* (Columbia University, NY, 1958), Vol. 31, p. 157.
[349]B. B. Kadomtsev, *Reviews of Plasma Physics* (Consultants Bureau, New York, 1966), Vol. 2, p. 178.
[350]H. E. Ramsey and S. F. Smith, Astrophys. J. **71**, 197 (1966).
[351]C. L. Hyder, Z. Astrophys. **63**, 78 (1966).
[352]O. Olmedo and J. Zhang, Astrophys. J. **718**, 433 (2010).
[353]P. Hammond, Proc. IEE-Part C: Monogr. **107**(12), 306 (1960).
[354]P. Démoulin and G. Aulanier, Astrophys. J. **718**, 1388 (2010).
[355]P. T. Gallagher, G. R. Lawrence, and B. R. Dennis, Astrophys. J. Lett. **588**, L53 (2003).
[356]R. M. MacQueen and R. R. Fisher, Sol. Phys. **89**, 89 (1983).
[357]J. T. Gosling, E. Hildner, R. M. MacQueen, R. H. Munro, A. I. Poland, and C. L. Ross, Sol. Phys. **48**, 389 (1976).
[358]N. Srivastava, R. Schwenn, B. Inhester, S. F. Martin, and Y. Hanaoka, Astrophys. J. **534**, 468 (2000).
[359]N. R. Sheeley, Jr., J. H. Walters, Y.-M. Wang, and R. A. Howard, J. Geophys. Res. **104**, 24,739, doi:10.1029/1999JA900308 (1999).
[360]Y.-J. Moon, G. S. Choe, H. Wang, Y. D. Park, N. Gopalswamy, G. Yang, and S. Yashiro, Astrophys. J. **581**, 694 (2002).
[361]B. C. Low and M. Zhang, Astrophys. J. **564**, L53 (2002).
[362]D. Alexander, T. R. Metcalf, and N. V. Nitta, Geophys. Res. Lett. **29**, 41, doi:10.1029/2001GL013670 (2002).
[363]M. Zhang, L. Golub, E. DeLuca, and J. Burkepile, Astrophys. J. **574**, L97 (2002).
[364]E. P. Carley, R. T. J. McAteer, and P. T. Gallagher, Astrophys. J. **752**, 36 (2012).
[365]C. E. Myers, M. Yamada, H. Ji, J. Yoo, W. Fox, J. Jara-Almonte, A. Savcheva, and E. E. DeLuca, Nature **528**, 526 (2015).
[366]H. Nakajima *et al*., Proc. IEEE **82**, 705 (1994).
[367]B. Vršnak, D. Maričič, A. L. Stanger, A. M. Veronig, M. Temmer, and D. Roša, Sol. Phys. **241**, 85 (2007).
[368]V. Yurchyshyn, S. Yashiro, V. Abramenko, H. Wang, and N. Gopalswamy, Astrophys. J. **619**, 599 (2005). y
[369]B. Vršnak, D. Sudar, and D. Ruždjak, Astron. Astrophys. **435**, 1149 (2005).
[370]A. Q. Chen, P. F. Chen, and C. Fang, Astron. Astrophys. **456**, 1153 (2006).
[371]B. Vršnak, Ann. Geophys. **26**, 3089 (2008).
[372]Y. Liu, Astrophys. J. Lett. **679**, L151 (2008).
[373]J. Chen, Phys. Rev. Lett. **99**, 099501 (2007).
[374]T. Wiegelmann, J. Geophys. Res. **113**, A03S02, doi:10.1029/2007JA012432 (2008).
[375]S. Liu, H. Q. Zhang, and J. T. Su, Sol. Phys. **270**, 89 (2011).
[376]A. B. Galvin *et al*., Space Sci. Rev. **136**, 437 (2008).
[377]M. H. Acuña *et al*., Space Sci. Rev. **136**, 203 (2008).
[378]T. Nieves-Chinchilla, private communication (2012).
[379]W. Neupert, Astrophys. J. Lett. **153**, L59 (1968).
[380]S. Tsuneta, Astrophys. J. **290**, 353 (1985).
[381]G. D. Holman, Astrophys. J. **293**, 584 (1985).
[382]A. G. Emslie and J.-C. Hénoux, Astrophys. J. **446**, 371 (1995).
[383]J. Jing, J. Qiu, J. Lin, M. Qu, Y. Xu, and H. Wang, Astrophys. J. **620**, 1085 (2005).
[384]J. Qiu, Q. Hu, T. A. Howard, and V. B. Yurchyshyn, Astrophys. J. **459**, 758 (2007).
[385]K. K. Reeves, Astrophys. J. **644**, 592 (2006).
[386]The concept of $d\Phi/dt \neq 0$ of subphotospheric origin as the driving function was regarded as "radical."[46] This numerical test of the predicted behavior of $d\Phi/dt \neq 0$ in the breakout model was carried out as part of a NASA-sponsored invesgitation: NASA # NNH06AD56I, Investigators: J. Chen (PI), J. Krall, S. K. Antiochos, and V. Yurchyshyn, 2005.
[387]P. Riley, R. Lionello, Z. Mikić, and J. Linker, Astrophys. J. **672**, 1221 (2008).
[388]J. G. Lyon, J. A. Fedder, and C. M. Mobarry, J. Atmos. Sol.-Terr. Phys. **66**, 1333 (2004).
[389]Y. Liu, J. D. Richardson, and J. W. Belcher, Planet. Space Sci. **53**, 3 (2005).
[390]A. M. Gulisano, P. Démoulin, S. Dasso, and L. Rodriguez, Astron. Astrophys. **543**, A107 (2012).
[391]D. M. Rust, Sol. Phys. **47**, 21 (1976).
[392]D. M. Rust, J. Geophys. Res. **106**, 25075, doi:10.1029/2000JA004016 (2001).
[393]A. Patterson, Astrophys. J. **280**, 884 (1984).
[394]H. Wang, M. W. Ewell, Jr., H. Zirin, and G. Ai, Astrophys. J. **424**, 436 (1994).
[395]R. Cameron and I. Sammis, Astrophys. J. **525**, L61 (1999).
[396]A. G. Kosovichev and V. V. Zharkova, Sol. Phys. **190**, 459 (1999).
[397]T. J. Spirock, V. B. Yurchyshyn, and H. Wang, Astrophys. J. **572**, 1072 (2002).
[398]H. Wang, T. J. Spirock, J. Qiu, H. Ji, V. Yurchyshyn, Y.-J. Moon, C. Denker, and P. R. Goode, Astrophys. J. **576**, 497 (2002).
[399]J. J. Sudol and J. W. Harvey, Astrophys. J. **635**, 647 (2005).
[400]A. Nindos and H. Zhang, Astrophys. J. **573**, L133 (2002).
[401]L. M. Green, M. C. López Fuentes, C. H. Mandrini, P. Démoulin, L. Van Driel-Gesztelyi, and J. L. Culhane, Sol. Phys. **208**, 43 (2002)
[402]K. Kusano, T. Maeshiro, T. Yokoyama, and T. Sakurai, Astrophys. J. **577**, 501 (2002)
[403]T. G. Forbes, EOS Transaction Of AGU (abstract), 82(20), Spring Meeting Supplment, SH41C-03 (2001). A talk at a special session convened by T. Zurbuchen, J. Chen, and S. Antiochos at the American Geophysical Union Spring Meeting, 2001. The talk was given at the invitation of J. Chen.
[404]T. G. Forbes, in *Heliophysics II. Plasma Physics of the Local Cosmos*, edited by C. J. Schrijver and G. L Siscoe (Cambridge University Press, 2010), pp. 159–191.
[405]P. W. Schuck, Astrophys. J. **714**, 68 (2010).
[406]H. Isobe, D. Tripathi, and V. Archotis, Astrophys. J. **657**, L53 (2007).
[407]E. N. Parker, Astrophys. J. **145**, 811 (1966).
[408]K. Shibata, T. Tajima, R. S. Steinolfson, and R. Matsumoto, Astrophys. J. **345**, 584 (1989).
[409]S. Toriumi and T. Yokoyama, Astron. Astrophys. **539**, A22 (2012).
[410]J. Krall, J. Chen, R. Santoro, D. S. Spicer, S. T. Zalesak, and P. J. Cargill, Astrophys. J. **500**, 992 (1998).
[411]J. E. Leake, M. G. Linton, and S. K. Antiochos, Astrophys. J. **722**, 550 (2010).
[412]R. J. Goldston and P. H. Rutherford, *Introduction to Plasma Physics* (IOP Publishing, Bristol, UK, 1995).
[413]L. M. Thornton and C. E. Parnell, Sol. Phys. **269**, 13 (2011).
[414]B. M. Haisch, Sol. Phys. **121**, 3 (1989).
[415]Y. Tsuboi, K. Koyama, H. Murakami, M. Hayashi, S. Skinner, and S. Ueno, Astrophys. J. **503**, 894 (1998).
[416]E. D. Feigelson and T. Montmerle, Annu. Rev. Astron. Astrophys. **37**, 363 (1999).
[417]M. Güdel, Ann. Rev. Astron. Astrophys. **40**, 217 (2002).
[418]S. K. P. Tripathi and W. Gekelman, Phys. Rev. Lett. **105**, 075005 (2010).
[419]W. Gekelman, E. Lawrence, and B. Van Compernolle, Astrophys. J. **753**, 131 15 doi: (2012).
[420]S. K. P. Tripathi and W. Gekelman, Sol. Phys. **286**, 479 (2013).